



# When Do Stalled Stars Resume Spinning Down? Advancing Gyrochronology with Ruprecht 147

Jason Lee Curtis<sup>1,2</sup> , Marcel A. Agüeros<sup>1</sup> , Sean P. Matt<sup>3</sup> , Kevin R. Covey<sup>4</sup> , Stephanie T. Douglas<sup>5</sup> , Ruth Angus<sup>1,2,6</sup> , Steven H. Saar<sup>5</sup> , Ann Marie Cody<sup>7</sup> , Andrew Vanderburg<sup>5,8</sup> , Nicholas M. Law<sup>9</sup> , Adam L. Kraus<sup>8</sup> , David W. Latham<sup>5</sup> , Christoph Baranec<sup>10</sup> , Reed Riddle<sup>11</sup> , Carl Ziegler<sup>12</sup> , Mikkel N. Lund<sup>13</sup> , Guillermo Torres<sup>5</sup> , Søren Meibom<sup>5</sup>, Victor Silva Aguirre<sup>13</sup> , and Jason T. Wright<sup>14</sup>

<sup>1</sup> Department of Astronomy, Columbia University, 550 West 120th Street, New York, NY 10027, USA; [jasoncurtis.astro@gmail.com](mailto:jasoncurtis.astro@gmail.com)

<sup>2</sup> Department of Astrophysics, American Museum of Natural History, Central Park West, New York, NY, USA

<sup>3</sup> University of Exeter, Department of Physics & Astronomy, Stocker Road, Exeter, EX4 4QL, UK

<sup>4</sup> Department of Physics & Astronomy, Western Washington University, Bellingham, WA 98225-9164, USA

<sup>5</sup> Center for Astrophysics, Harvard & Smithsonian, 60 Garden Street, Cambridge, MA 02138, USA

<sup>6</sup> Center for Computational Astrophysics, Flatiron Institute, 162 5th Avenue, Manhattan, NY, USA

<sup>7</sup> Bay Area Environmental Research Institute, 625 2nd Street, Ste. 209, Petaluma, CA 94952, USA

<sup>8</sup> Department of Astronomy, The University of Texas at Austin, Austin, TX 78712, USA

<sup>9</sup> Department of Physics and Astronomy, University of North Carolina, Chapel Hill, NC 27599, USA

<sup>10</sup> Institute for Astronomy, University of Hawai'i at Mānoa, 640 N. A'ohōkū Pl., Hilo, HI 96720-2700, USA

<sup>11</sup> Division of Physics, Mathematics, and Astronomy, California Institute of Technology, Pasadena, CA 91125, USA

<sup>12</sup> Dunlap Institute for Astronomy and Astrophysics, University of Toronto, 50 St. George Street, Toronto, ON M5S 3H4, Canada

<sup>13</sup> Stellar Astrophysics Centre, Department of Physics and Astronomy, Aarhus University, Ny Munkegade 120, DK-8000 Aarhus C, Denmark

<sup>14</sup> Penn State Extraterrestrial Intelligence Center/Center for Exoplanets and Habitable Worlds/ Department of Astronomy & Astrophysics, 525 Davey Laboratory, The Pennsylvania State University, University Park, PA 16802, USA

Received 2020 April 10; revised 2020 September 27; accepted 2020 September 28; published 2020 November 27

## Abstract

Recent measurements of rotation periods ( $P_{\text{rot}}$ ) in the benchmark open clusters Praesepe (670 Myr), NGC 6811 (1 Gyr), and NGC 752 (1.4 Gyr) demonstrate that, after converging onto a tight sequence of slowly rotating stars in mass–period space, stars temporarily stop spinning down. These data also show that the duration of this epoch of stalled spin-down increases toward lower masses. To determine when stalled stars resume spinning down, we use data from the K2 mission and the Palomar Transient Factory to measure  $P_{\text{rot}}$  for 58 dwarf members of the 2.7 Gyr old cluster Ruprecht 147, 39 of which satisfy our criteria designed to remove short-period or near-equal-mass binaries. Combined with the Kepler  $P_{\text{rot}}$  data for the approximately coeval cluster NGC 6819 (30 stars with  $M_* > 0.85 M_{\odot}$ ), our new measurements more than double the number of  $\approx 2.5$  Gyr benchmark rotators and extend this sample down to  $\approx 0.55 M_{\odot}$ . The slowly rotating sequence for this joint sample appears relatively flat ( $22 \pm 2$  days) compared to sequences for younger clusters. This sequence also intersects the Kepler intermediate-period gap, demonstrating that this gap was not created by a lull in star formation. We calculate the time at which stars resume spinning down and find that  $0.55 M_{\odot}$  stars remain stalled for at least 1.3 Gyr. To accurately age-date low-mass stars in the field, gyrochronology formulae must be modified to account for this stalling timescale. Empirically tuning a core–envelope coupling model with open cluster data can account for most of the apparent stalling effect. However, alternative explanations, e.g., a temporary reduction in the magnetic braking torque, cannot yet be ruled out.

*Unified Astronomy Thesaurus concepts:* [Open star clusters \(1160\)](#); [Stellar evolution \(1599\)](#); [Stellar ages \(1581\)](#); [Stellar rotation \(1629\)](#)

*Supporting material:* data behind figure, figure sets, machine-readable tables

## 1. Introduction

Observations of Sun-like stars revealed that they spin down over time via magnetic braking. This led to the development of gyrochronology, a promising age-dating technique that uses rotation periods ( $P_{\text{rot}}$ ) as a clock (Barnes 2003).<sup>15</sup> Recent measurements of  $P_{\text{rot}}$  in the benchmark open clusters Praesepe (670 Myr; Douglas et al. 2017), the Hyades (730 Myr; Douglas et al. 2019), NGC 6811 (1.0 Gyr; Curtis et al. 2019a), and

NGC 752 (1.4 Gyr; Agüeros et al. 2018), however, have shown that the formula describing the process of stellar spin-down cannot be as simple as it once appeared. Instead of  $P_{\text{rot}}$  evolving continuously as a power law with a braking index that is constant in time and common to all stars (i.e.,  $P_{\text{rot}} \propto t^n$ , with Skumanich 1972 originally proposing  $n = 0.5$ ), it is now clear that, after converging onto a slowly rotating sequence that illustrates the tight relationship between mass and  $P_{\text{rot}}$  in clusters older than  $\approx 100$  Myr, stars temporarily stop spinning down. Furthermore, based on where the period sequences for these benchmark clusters overlap, Agüeros et al. (2018) concluded that the duration of this epoch of stalled spin-down increases toward lower stellar masses.

Most empirical gyrochronology relations (e.g., Barnes 2007, 2010) and angular momentum evolution models (e.g., van Saders & Pinsonneault 2013; Gallet & Bouvier 2015; Lanzafame & Spada 2015; Matt et al. 2015), which predate these new

<sup>15</sup> We define Sun-like broadly, to include all stars with radiative cores and convective envelopes, i.e.,  $0.4 \lesssim M_* \lesssim 1.3 M_{\odot}$ , or spectral types early M to late F. These stars have solar-like dynamos and undergo magnetic braking.

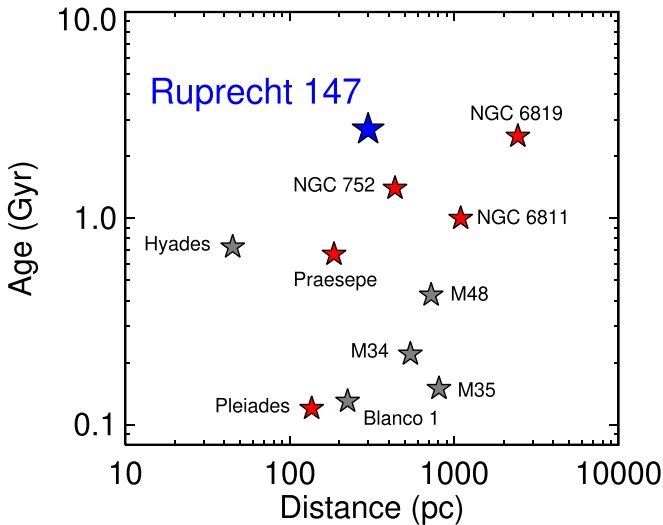


**Figure 1.** Age vs. distance for a selection of benchmark open clusters with  $P_{\text{rot}}$  data. Red stars indicate clusters used in this study; gray stars represent other notable clusters with  $P_{\text{rot}}$  data mentioned in this paper. Ruprecht 147 and NGC 6819 have similar ages, but Ruprecht 147 is much closer to Earth and its stars are  $\approx 77\times$  brighter. This allows us to measure  $P_{\text{rot}}$  for Ruprecht 147 stars with much lower masses than was possible with the Kepler survey of NGC 6819.

observational findings, do not account for the phenomenon of stalling, so ages inferred for low-mass stars with these models will likely be incorrect. It is therefore imperative that we extend the benchmark sample of cluster rotators to lower masses and older ages. This will allow us to constrain the timescale for stalled spin-down and to eventually repair empirical gyrochronology models, so that accurate ages can be inferred for low-mass stars in the field. These new data are also needed to tune free parameters in the more physically motivated class of gyrochronology models (for a recent example using our new  $P_{\text{rot}}$  data for NGC 6811 from Curtis et al. 2019a, see Spada & Lanzafame 2020).

We present measurements of  $P_{\text{rot}}$  for the 2.7 Gyr old open cluster Ruprecht 147, the oldest nearby open cluster (see Figure 1). In Section 2, we discuss the properties of and membership criteria for this cluster and then identify binaries among, and estimate stellar parameters for, the targets of this study. In Section 3, we analyze photometric time series data from NASA’s K2 mission (Howell et al. 2014) and the Palomar Transient Factory (PTF; Law et al. 2009; Rau et al. 2009) and measure  $P_{\text{rot}}$  for 58 dwarf members with masses as low as  $M_{\star} \approx 0.55 M_{\odot}$ . In Section 4, we identify 35 of these as benchmark rotators, including 23 likely single stars, discuss the impact of binarity on the color–period distribution, and present a rotation catalog for Ruprecht 147.

Our sample of rotators in Ruprecht 147 contains few stars with masses  $\gtrsim 1 M_{\odot}$ . To remedy this, we combine our sample with  $P_{\text{rot}}$  measurements for the approximately coeval (2.5 Gyr) cluster NGC 6819, which was surveyed during the primary Kepler mission (Meibom et al. 2015). Because stars in NGC 6819 were monitored 10–16 $\times$  longer than those in Ruprecht 147, and because the Kepler light curves contain negligible systematics compared to our K2 Campaign 7 data, Meibom et al. (2015) were able to recover weaker amplitude signals in the NGC 6819 data than we could detect in the Ruprecht 147 light curves. This enabled Meibom et al. (2015) to measure  $P_{\text{rot}}$  for early G dwarfs in NGC 6819, although the cluster’s larger distance modulus restricted their overall  $P_{\text{rot}}$

sample to  $M_{\star} > 0.85 M_{\odot}$ . In this study, we contribute rotation periods for 20 benchmark rotators with masses smaller than this lower limit for NGC 6819.

Pairing the rotation data for NGC 6819 and Ruprecht 147 allows us to describe stellar rotation at 2.5–2.7 Gyr as a function of mass from late F down to M1 spectral types. Section 5 describes this procedure, which involves calculating the average interstellar reddening toward NGC 6819 relative to Ruprecht 147 and estimating their relative ages with gyrochronology using the portions of each sample that overlap significantly in mass (i.e., mid- to late G dwarfs).

The slowly rotating sequence for this joint sample appears relatively flat compared to sequences for younger clusters. In Section 6, we use this sample to determine when stars resume spinning down after enduring the temporary stalling epoch. We find that the lowest-mass stars in our sample resumed spinning down only 700 Myr ago. This is consistent with the new mass-dependent core–envelope coupling timescale derived by Spada & Lanzafame (2020). We also note that the Ruprecht 147  $P_{\text{rot}}$  sequence intersects the Kepler intermediate-period gap (McQuillan et al. 2014), i.e., the color dependence of the gap is different from the color dependence of rotation periods at any one age. This demonstrates that the gap was not created by a temporary lull in the star formation rate 600 Myr ago.

We conclude in Section 7.

## 2. Properties, Membership, Multiplicity, and Stellar Parameters for Ruprecht 147

### 2.1. Fundamental Cluster Properties

We adopt an age of  $2.7 \pm 0.2$  Gyr for Ruprecht 147, based on the analysis of the masses and radii for three eclipsing binary systems (EBs; Torres et al. 2018, 2019, 2020). This value is consistent with ages obtained from fitting isochrones to color–magnitude diagrams (CMDs; Curtis et al. 2013; Curtis 2016).

Based on spectra for six single solar twins observed with the MIKE spectrograph (Bernstein et al. 2003) on the 6.5 m Magellan Clay Telescope at Las Campanas Observatory and with the High Resolution Echelle Spectrometer (HIRES; Vogt et al. 1994) on the 10 m Keck telescope, which we analyzed with Spectroscopy Made Easy (SME; Valenti & Fischer 2005; Brewer et al. 2015), we adopt a metallicity for the cluster of  $[\text{Fe}/\text{H}] = +0.10 \pm 0.03$  dex (see Table 5.4 in Curtis 2016). This is consistent with all other analyses in the literature (Pakhomov et al. 2009; Curtis et al. 2013; Bragaglia et al. 2018; Casamiquela et al. 2020).

We calculated the average interstellar reddening by comparing the Gaia DR2 colors,  $(G_{\text{BP}} - G_{\text{RP}})$ ,<sup>16</sup> with spectroscopic temperatures ( $T_{\text{eff}}$ ) derived from high-resolution spectroscopy using SME for nearby, unreddened field stars (Valenti & Fischer 2005) and the same six solar twin members of Ruprecht 147 used to measure the cluster metallicity. We found a reddening value of  $E(B - V) = 0.099 \pm 0.010$ , or equivalently an extinction value of  $A_V = 0.31 \pm 0.03$  assuming a standard  $R_V = A_V/E(B - V) = 3.1$  relationship. This new value is consistent with CMD isochrone fitting ( $A_V = 0.30$  in Figure 2 in this work;  $A_V = 0.25 \pm 0.05$  from Curtis et al. 2013) and EB

<sup>16</sup> We applied extinction coefficients calculated by the PARSEC isochrone service (Bressan et al. 2012) using the Evans et al. (2018) passbands: <http://stev.oapd.inaf.it/cgi-bin/cmd>.  $A_G \approx 0.86 A_V$ ,  $E(G_{\text{BP}} - G_{\text{RP}}) \approx 0.415 A_V$ .

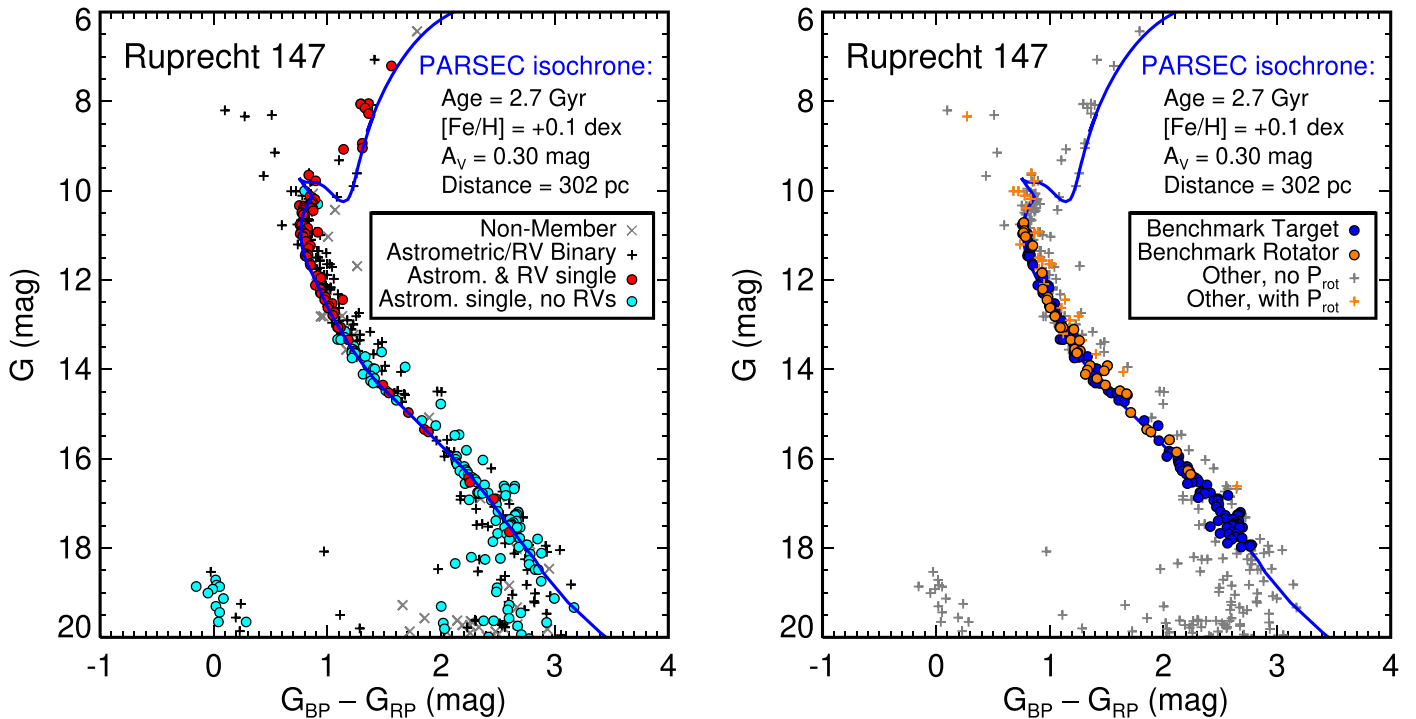


**Figure 2.** Gaia DR2 CMDs for Ruprecht 147. Left: stars with astrometry and RVs consistent with single-star membership are highlighted in red (77 stars). Cyan points indicate astrometrically single stars lacking RVs (145 stars). Stars with parallaxes and/or RVs in violation of our membership criteria are marked with crosses (43 stars). All other stars marked with plus signs are assumed to be either astrometric and/or RV binaries (175 stars). The PARSEC isochrone solution we adopt is overlaid: 2.7 Gyr,  $[Fe/H] = +0.10$  dex,  $A_V = 0.30$ ,  $(m - M)_0 = 7.40$ . Right: this CMD highlights the gyrochronology benchmark targets, which are photometrically single dwarfs ( $10.5 < G < 18$ ) that are not EBs, SB2s, or short-period SB1s (161 blue points). This includes 39 benchmark dwarfs with measured rotation periods (orange points). Also shown are nonbenchmark stars (gray plus signs, 211 stars) and nonbenchmark rotators (orange plus signs, 29 stars).

analyses ( $A_V = 0.35 \pm 0.09$ ; Torres et al. 2018). For this work, we adopt  $A_V = 0.30$ .

We adopt a distance modulus of  $(m - M)_0 = 7.40$  ( $d \approx 302$  pc).<sup>17</sup> This is consistent with the CMD isochrone fitting ( $(m - M)_0 = 7.35 \pm 0.1$ ; Curtis et al. 2013) and EB results ( $(m - M)_0 = 7.26 \pm 0.13$ ; Torres et al. 2018). The cluster parallax from the second Gaia data release (DR2; Gaia Collaboration et al. 2018b) is  $\varpi = 3.2516 \pm 0.0038$  (Gaia Collaboration et al. 2018a); if the DR2 parallaxes are indeed systematically biased toward smaller values (e.g., Lindegren et al. 2018; Sahlholdt & Silva Aguirre 2018; Stassun & Torres 2018; Zinn et al. 2019), the parallax would increase to between 3.28 and 3.33 mas, corresponding to  $(m - M)_0 = 7.42$  or 7.39 mag, respectively. This bias does not alter the age or interstellar reddening values, which were determined independently of distance.

## 2.2. Cluster Membership

Our pre-Gaia target list included  $>1000$  candidates based on proper motions from PPMXL (Roesser et al. 2010) and catalogs produced by the United States Naval Observatory (e.g., NOMAD, UCAC2; Zacharias et al. 2004a, 2004b) and on photometry from CFHT/MegaCam ( $g'$ ,  $r'$ ,  $i'$ ; Curtis et al. 2013; Curtis 2016), UKIRT/WFCAM ( $J$ ,  $K$ ; Curtis 2016), and the Two Micron All Sky Survey (2MASS  $J$ ,  $H$ ,  $K_S$ ; Skrutskie et al. 2006). From this preliminary candidate list, Curtis (2016)

<sup>17</sup>  $(m - M)_0$  refers to the unreddened distance modulus representing only the physical distance. When a photometric band is listed in the subscript, this indicates the total difference between the apparent and absolute magnitude, i.e.,  $(m - M)_V = A_V + 5 \log_{10}(d/10)$ , where  $d$  is in pc.

identified 150 stars with radial velocities (RVs) consistent with membership.<sup>18</sup>

With Gaia DR2, we now also have high-precision astrometry and photometry for stars reaching down to  $G \approx 20$  mag. We expanded our candidate list by merging Gaia-based membership lists from the literature, including 234 stars from Gaia Collaboration et al. (2018a), 191 stars from Cantat-Gaudin et al. (2018), and 259 stars from Olivares et al. (2019).

However, even with Gaia data, constructing a complete cluster catalog is not straightforward, as binaries can severely bias the Gaia astrometry. Indeed, in rare cases, unresolved binaries can cause the astrometric and photometric solutions to fail entirely, preventing a star's inclusion in Gaia DR2. For example, the Curtis et al. (2013) cluster member CWW 87<sup>19</sup> does not appear in Gaia DR2. A high-resolution adaptive optics

<sup>18</sup> We have measured RVs for cluster candidates using the Hamilton echelle spectrometer on the 120-inch Shane telescope at Lick Observatory (Vogt 1987), the East-Arm Echelle (Peri 1995) on the Hale 200-inch telescope at Palomar Observatory, the Hectochelle multiobject spectrograph (Szentgyorgyi et al. 1998; Fűrész et al. 2008) on the 6.5 m telescope at MMT Observatory (Fabricant et al. 2004), the MIKE and Magellan Echelle (MagE; Marshall et al. 2008) spectrographs on the 6.5 m Clay Telescope at Las Campanas Observatory, and the Tillinghast Reflector Echelle Spectrograph (TRES; Szentgyorgyi & Fűrész 2007) on the 1.5 m Tillinghast telescope at Fred Lawrence Whipple Observatory (see Chapters 2.2 and 3.3.2; Curtis 2016). We supplemented these data with archival RVs from the High Accuracy Radial velocity Planet Searcher (HARPS; Mayor et al. 2003) on the 3.6 m telescope at La Silla Observatory (PI Minniti; Run IDs 091.C-0471(A) and 095.C-0947(A), accessible from the public archive by Trifonov et al. 2020), and from the Gaia Radial Velocity Spectrometer (Soubiran et al. 2013).

<sup>19</sup> Also known as EPIC 219659980, 2MASS J19160785-1610360, and NOMAD 0738-0795586. PPMXL proper motions and our RVs support its membership of the cluster.

(AO) instrument, Robo-AO (Baranec et al. 2014), image for this star shows a companion at  $0''.42$  with a Sloan Digital Sky Survey (SDSS)  $i$ -band contrast of  $\Delta i = 0.57 \pm 0.05$  (see Figure 3.10 in Curtis 2016),<sup>20</sup> which we suspect is responsible for this star’s exclusion. Such cases are why assembling a complete membership catalog for Ruprecht 147 is beyond the scope of this paper.

Our final list of cluster members contains 440 stars.<sup>21</sup> This list is provided as a machine-readable table in the online journal, and its contents are described in Table 1. The CMD for this list is displayed in Figure 2. Because only Sun-like stars experience magnetic braking, we also limit our list of stars of interest to those with  $G > 10.5$ , corresponding to stars with  $M_* \lesssim 1.4 M_\odot$ . Of these, 258 are main-sequence dwarfs with  $G < 18$  mag; the remainder are white dwarfs (WDs), red giants, blue stragglers, or dwarfs too faint for us to measure their  $P_{\text{rot}}$ . Below we assess the binarity/multiplicity of each of these stars.

### 2.3. Stellar Multiplicity

#### 2.3.1. Spectroscopic Binaries

We identified seven EBs and 23 double-lined spectroscopic binaries (SB2s; see Chapters 3.1.4.4 and 4 in Curtis 2016). Because these systems have short orbital periods, the rotational evolution of these stars can be affected by tidal interactions, limiting their use in constraining gyrochronology (Meibom & Mathieu 2005; Douglas et al. 2019). Furthermore, if absorption lines are detectable for multiple stars in an optical spectrum (thus identifying it as an SB2), then the light curve will also certainly be sensitive to the binary components as well. For both reasons, we reject SB2s and EBs from our “benchmark sample”—those stars that appear to be single, or effectively single, like long-period, high-contrast binaries.

We identify single-lined spectroscopic binaries (SB1) by observing variability in RV measurements. Following the methodology developed by the WIYN Open Cluster Study (Geller et al. 2008), we calculate the  $e/i$  statistic (called “rv\_ei” in Table 1), where  $e$  represents the variance in the RV data set and  $i$  is the expected measurement precision, and flag 13 stars with  $e/i > 4$  as SB1s (not counting SB2s or EBs). There are an additional six stars with Gaia RV errors greater than  $4 \text{ km s}^{-1}$ , which we assume are due to RV variations, and we therefore classified these as SB1s as well.

Candidate long-period binaries can be identified by calculating the absolute RV deviation from the cluster median and flagging those greater than some threshold value based on the expected intrinsic cluster dispersion ( $\approx 0.5 \text{ km s}^{-1}$ ) and the measurement precision. We initially adopted a larger  $5 \text{ km s}^{-1}$  value and found six RV outliers: each only has RVs from Gaia, and given the relatively low RV errors ( $0.2\text{--}3.4 \text{ km s}^{-1}$ ) from multiple measurements (2–10 each) and relatively large RV deviations ( $7\text{--}107 \text{ km s}^{-1}$ ), these are likely nonmembers and are discussed further in Section 2.3.5.

<sup>20</sup> We acquired high spatial resolution imaging for 130 cluster members and candidates with Robo-AO in 2013 while it was on the Palomar 60-inch telescope (Chapters 2.6 and 3.3.1 of Curtis 2016).

<sup>21</sup> Two of these stars lack five-parameter astrometric solutions from Gaia, so we adopt the PPMXL proper motions for them. Nine stars lack Gaia color, ( $G_{\text{BP}} - G_{\text{RP}}$ ), but they were not observed with K2 and rotation periods were not detected with PTF, so this does not affect our study.

Table 1 lists spectroscopic binary classifications in the “spec\_binary” column, which are assigned in this order: “N/A” if no RVs are available; “RV-NM” if the median RV is systematically offset from R147 by “dRV”  $> 10 \text{ km s}^{-1}$ ; “SB1-Long” if the RVs either exhibit long-term trends, have measured orbital periods  $> 100$  days, or  $5 < \text{“dRV”} < 10$ ; while satisfying astrometric and photometric membership criteria; “SB1-Short” if “rv\_ei”  $> 4$  or “e\_RV\_Gaia”  $> 4 \text{ km s}^{-1}$ ; “SB2” according to the spectrum and cross-correlation function shapes; else “No” if RV data indicate that the star is likely single. See Appendix D.9 for two exceptions.

#### 2.3.2. Astrometric Binaries

The Gaia DR2 proper motions are precise enough that certain binaries can be identified by a star’s moderate deviation from the cluster’s average value. If the cluster’s internal velocity dispersion is  $\sigma_V = 0.5 \text{ km s}^{-1}$ , at 300 pc this would be equal to  $0.35 \text{ mas yr}^{-1}$ . The Gaia proper-motion error does increase toward fainter magnitudes, but this is insignificant over the brightness range of the rotator sample we construct in the next section (e.g., the error for the faintest rotator in our sample is only  $\sigma_\mu = 0.16 \text{ mas yr}^{-1}$ ), and so we ignore this. Since we do not know the internal velocity dispersion yet, we conservatively flag stars that deviate from the cluster by  $\Delta\mu > 2 \text{ mas yr}^{-1}$  as astrometric binary candidates, based on the distribution of  $\Delta\mu$  for our target list.

Excess astrometric noise can indicate whether a source deviates significantly from the single-star model used to derive the astrometric parameters for the Gaia DR2 catalog. Candidate wide binaries can therefore be identified by selecting sources with poor astrometric solutions. The renormalized unit weight error (RUWE)<sup>22</sup> accounts for the strong dependencies of the astrometric noise on color and magnitude.<sup>23</sup> Single stars with good astrometric solutions should have  $\text{RUWE} \approx 1$ . We classify 32 dwarfs with  $\text{RUWE} > 1.4$  as candidate binaries. Many of these also appear as photometric binaries in the CMD, but this is not required, as even high mass ratio companions can impart measurable astrometric perturbations.

#### 2.3.3. Visual Binaries Resolved with Adaptive Optics

We have observed 130 cluster stars with Robo-AO (Baranec et al. 2014), of which 50 are dwarfs less massive than the  $1.4 M_\odot$  cutoff for this study. These data were analyzed following Ziegler et al. (2018). Companions/neighbors were detected for the five targets in Table 2 (see also Chapters 2.6 and 3.3.1 of Curtis 2016).

The four stars with neighbors within  $1''$  all have  $\text{RUWE} > 2$ , confirming that this parameter is useful for identifying unresolved wide binaries in Gaia DR2. Both components for the nearly equal mass wide binary EPIC 219678096 were resolved in Gaia DR2 and have separate entries in that and our catalog.

<sup>22</sup> RUWE values were downloaded from <http://gaia.ari.uni-heidelberg.de/singlesource.html>.

<sup>23</sup> For a description of RUWE, see [http://www.rssd.esa.int/doc\\_fetch.php?id=3757412](http://www.rssd.esa.int/doc_fetch.php?id=3757412).

**Table 1**  
Description of Data in the Ruprecht 147 Catalog

Column	Format	Units	Example	Description
<i>Identifiers:</i>				
DR2Name	string	...	4183944182414043136	Gaia DR2 Source ID
Twomass	string	...	J19172940-1611577	2MASS Source ID
EPIC	string	...	219651610	K2 EPIC ID
CWW	string	...	108	ID from Curtis et al. (2013)
NOMAD	string	...	0738-0797617	NOMAD ID (Zacharias et al. 2004a)
<i>Astrometry:</i>				
R.A.	double	degrees	289.37254	Right ascension in decimal degrees
Decl.	double	degrees	-16.199489	decl. in decimal degrees
pmra	float	mas yr <sup>-1</sup>	-0.946	Right ascension proper motion
pmde	float	mas yr <sup>-1</sup>	-26.775	decl. proper motion
epm	float	mas yr <sup>-1</sup>	0.071	Proper-motion error
astrom_source	string	...	Gaia DR2	Source of astrometry (Gaia DR2 or PPMXL)
plx	float	mas	3.3023	Parallax
eplx	float	mas	0.0304	Parallax error
epsi	float	...	0.000	Astrometric excess noise ( $\epsilon_i$ )
sepsi	float	...	0.000	Significance of astrometric excess noise ( $D$ )
ruwe	float	...	1.093	Renormalized unit weight error
<i>Photometry:</i>				
Gmag	float	mag	14.3257	Gaia DR2 $G$ magnitude
bp_rp	float	mag	1.47600	Gaia DR2 color: ( $G_{BP} - G_{RP}$ )
e_br	float	mag	0.004	Gaia DR2 photometric error: $\sqrt{(\sigma_{BP}^2 + \sigma_{RP}^2)}$
Jmag	float	mag	12.474	2MASS $J$ magnitude
Kmag	float	mag	11.767	2MASS $K_S$ magnitude
e_jk	float	mag	0.031	2MASS photometric error: $\sqrt{(\sigma_J^2 + \sigma_K^2)}$
<i>Radial velocities:</i>				
RV_Gaia	float	km s <sup>-1</sup>	...	Gaia DR2 radial velocity
e_RV_Gaia	float	km s <sup>-1</sup>	...	Gaia DR2 radial velocity error
RV_R147Project	float	km s <sup>-1</sup>	42.15	Median radial velocity from non-Gaia data
nRV	integer	...	5	Number of non-Gaia RV measurements
rv_ei	float	...	1.7	RV variability to error ratio ( $e/i$ ; Geller et al. 2008)
dRV	float	km s <sup>-1</sup>	0.6	RV deviation from cluster
RVdelT	float	days	1886	RV epoch baseline
<i>Membership and binarity:</i>				
Member	string	...	Yes	1st character: "Y" (Yes), "P" (Probable), "N" (Nonmember)
Photo_Binary	string	...	No	if $ dcmd  > 0.4$ mag then "Yes," else "No"
Wide_Binary	string	...	No	"Yes" if $(pmd > 2 \text{ mas yr}^{-1})$ or $(AO = \text{Yes})$ or $(RUWE > 1.4)$ , else "No"
Spec_Binary	string	...	No	SB2, SB1-Short, SB1-Long, No, N/A (see comment for criteria)
rad	float	degrees	0.7	Radial R.A./decl. coordinate distance
drad	float	pc	5.0	3D distance from cluster center
pmd	float	mas yr <sup>-1</sup>	0.1	Proper-motion deviation from cluster
dplx	float	mas	0.05	Parallax deviation from cluster
dcmd	float	mag	0.04	Photometric excess in $G$
AO	string	...	No	Robo-AO detection? (Yes, No, N/A)
<i>Stellar properties:</i>				
Teff	integer	K	4525	Effective temperature
Mass	float	$M_{\odot}$	0.74	Mass
SpT	string	...	K4	Spectral type
<i>Rotation data:</i>				
K2_PTF_Data	string	...	S_Y	Observed by K2? (S=superstamp, A=aperture, N=No) PTF? (Y/N)
Prot	float	days	20.4	Rotation period. Negative values indicate $P_{rot}$ is not trusted.
Prot_Source	string	...	Both	Light curve used to measure $P_{rot}$ : PTF, K2, or both
sigma_LC	float	ppt	4.8	Photometric noise for light curve
Rvar_LC	float	ppt	20.3	Photometric amplitude for light curve
Near_mag	float	mag	18.3	$G$ magnitude of brightest neighbor within $12''$
Near_rad	float	arcsec	7.0	Distance to brightest neighbor within $12''$
Benchmark	string	...	Yes	No/Yes/Yes-Rapid_Outlier/Yes-Prot_Secondary?
Notes	string	...	...	Notes on K2 light curve or the target

**Note.** The table is available for download in the online journal. To reproduce our benchmark rotator sample, query "Prot"  $> 0$  and "Benchmark" = "Yes."  
(This table is available in its entirety in machine-readable form.)

**Table 2**  
Cluster Gyrochronology Targets with Companions Detected in Our Robo-AO Observations

EPIC ID	NOMAD ID	RUWE	Ang. Sep.	Contrast
219633753	0737–0795762	4.4	0"7	$\Delta m = 2.7$ mag
219678096	0738–0796304	0.9	1"6	$\Delta i = 0.0$ mag
219664556	0738–0795948	24.6	0"2	$\Delta i = 0.6$ mag
219777155	0741–0796328	2.4	0"5	$\Delta i = 2.4$ mag
219366731	0730–0979511	79.5	0"6	$\Delta m = 1.6$ mag

**Note.** The NOMAD IDs (Zacharias et al. 2004a) are useful for looking up the Robo-AO images presented in Figures 3.9 and 3.10 in Curtis (2016). The third column provides the Gaia DR2 RUWE, which should be valued near 1 for single stars; we flag stars with  $RUWE > 1.4$  as candidate wide binaries. The last column gives the difference between the magnitude of the detected neighbor and that of the target, where  $i$  is the SDSS filter and  $m$  denotes the Robo-AO 600 nm long pass filter. For reference, 0"5 at 300 pc projects to 150 au.

### 2.3.4. Photometric Binaries

Binaries can also appear brighter than the single-star main sequence. We use a 2.7 Gyr PARSEC isochrone with  $[Fe/H] = +0.1$  dex,  $A_V = 0.30$ , and  $(m - M)_0 = 7.4$  to measure the  $G$ -band excess in the  $(G_{BP} - G_{RP})$  versus  $G$  CMD (“dcmd” in Table 1). We also inspect  $(G_{BP} - G_{RP})$  versus  $M_G$  and  $(G - 2MASS K_S)$  versus  $G$  CMDs. If a star is within 0.4 mag of the single-star sequence in at least one of these diagrams, it is classified as photometrically single. We flag 70 stars as photometric binaries from our list of 258 dwarf targets. Identifying photometric binaries/multiples is important because, like SB2s, the spot modulation signals from both/all stars are blended in the light curves, and those signals will interfere with each other and can confuse the periodicity analysis. In such situations, even if multiple periods can be distinguished, we cannot confidently assign each to the appropriate binary component.

### 2.3.5. Nonmembers

Ruprecht 147 likely has tidal tails and a diffuse halo containing many additional members that are currently dispersing into the Galaxy (Yeh et al. 2019). Kounkel & Covey (2019) identified candidates eight degrees away from the cluster center. Focusing on their 178 brighter stars with precise and reliable astrometry, 70% are within 20 pc of the cluster center, 90% are contained to 85 pc, and the most distant is at 490 pc. Out of the 85 stars with Gaia RVs with errors under  $4 \text{ km s}^{-1}$  (to filter out short-period SB1s), 70 share Galactic  $UVW$  velocities to within  $<5 \text{ km s}^{-1}$  of our Ruprecht 147 membership, reaching out to 54 pc. Most do not yet have RVs, which will be even more critical to corroborate the membership of such evaporated low-mass stars than in the vicinity of the core, where proper motions alone are often sufficient. It is therefore premature to incorporate them into our analysis, and we focus our present study on those that we can place the highest confidence in membership. In the future, especially after subsequent Gaia data releases provide even higher-precision astrometry, and RVs for fainter stars, we will revisit the topic of the evaporating membership and examine their magnetic activity and rotational behavior relative to the distribution found for our bona fide single-star members.

For this reason, stars with reliable parallaxes ( $RUWE < 1.4$ ) indicating that they are  $>100$  pc away from the core are classified as nonmembers. Some stars have high-quality five-parameter astrometric solutions (coordinates, proper motions, parallaxes) and have RVs from Gaia and/or our database. For those that are also not already classified as SB2s or short-period SB1s, we calculate Galactic  $UVW$  velocities and reclassify stars with large discrepancies as nonmembers ( $\Delta UVW > 10 \text{ km s}^{-1}$ ). Those with differential values ranging between 5 and  $10 \text{ km s}^{-1}$  are classified as possible members and candidate binaries, irrespective of their distance.

For example, Gaia DR2 408924111304212992 ( $(G_{BP} - G_{RP}) = 1.25$  and  $G = 11.66$ ) appears to be a photometric binary or even triple in the CMD. However, with  $\varpi = 2.5$  mas, it is 100 pc away from the core. Although the proper motion and RVs suggest membership, transforming these into Galactic  $UVW$  reveals that its 3D space motion is  $13 \text{ km s}^{-1}$  discrepant from R147. We therefore reclassify it as a nonmember.

In Table 1, the first character of the “member” column will read “Y” (yes, these are considered members; 395 stars), “P” (these are probably members; 2 stars), or “N” (no, these are not likely members; 43 stars).

## 2.4. Stellar Properties

We estimated  $T_{\text{eff}}$  and spectral type for members of Ruprecht 147 following the procedure described by Curtis et al. (2019a). Specifically, we calculated  $T_{\text{eff}}$  from the dereddened Gaia DR2 color  $(G_{BP} - G_{RP})_0$  using a color–temperature relation we constructed using nearby benchmark stars from Brewer et al. (2016a), Boyajian et al. (2012), and Mann et al. (2015); see Appendix A.1 for details. We then interpolated the stellar properties table in Kraus & Hillenbrand (2007) to estimate spectral types from our photometric  $T_{\text{eff}}$  values.

In Curtis et al. (2019a), we also estimated stellar masses by interpolating this same table. However, this procedure yields biased results for the high-mass end of the Ruprecht 147 sample, where  $M_* > 1.2 M_\odot$  stars have evolved substantially away from the zero-age main sequence toward cooler temperatures. For such stars, color inaccurately biases estimated masses toward lower values. For this study, we instead use a PARSEC isochrone appropriate for Ruprecht 147 (2.7 Gyr,  $[Fe/H] = +0.10$  dex,  $A_V = 0.30$ ,  $(m - M)_0 = 7.4$ ) to estimate masses from Gaia photometry.

Figure 2 presents the Gaia DR2 CMD for the Ruprecht 147 members (440 stars) and highlights stars with astrometry and RVs consistent with single-star membership (222 stars). Approximately half of our membership list are candidate binaries, which is consistent with the stellar multiplicity seen in the solar neighborhood (Raghavan et al. 2010; Duchêne & Kraus 2013). The figure also includes a version of the CMD that highlights our gyrochronology benchmark targets (161 stars), which are photometrically single dwarfs ( $10.5 < G < 18$ ), excluding EBs, SB2s, and short-period SB1s. In Section 4, we report rotation periods for 40 of these benchmark stars, which are also highlighted in this CMD.

## 3. Measuring Rotation in Ruprecht 147

### 3.1. Measuring $P_{\text{rot}}$ with K2 Light Curves

Our team petitioned to adjust the pointing for K2’s Campaign 7 so that it covered Ruprecht 147, which we then

proposed to monitor (GO proposal 7035).<sup>24</sup> Our GO program was allocated 1086 individual apertures for candidate members. A series of contiguous apertures, a “superstamp,” was created to tile the inner cluster core in response to a different proposal and covered 96 additional candidates from our preliminary membership list (Cody et al. 2018).

Our target list was designed in 2015 to maximize completeness in anticipation of the high-precision Gaia astrometry and photometry that would become available 3 yr later. For this reason, a large number of objects on the GO 7035 target list are now known to be nonmembers.

Of our 258 potential gyrochronology targets, 105 have K2 data: 70 stars were allocated individual apertures, and 35 are in the superstamp. Fifty-one other members of Ruprecht 147 also have K2 data, including evolved stars, blue stragglers, and members with  $G > 18$  mag.

All targets that were allocated individual apertures have light curves produced by the K2 team with the Pre-search Data Conditioning Simple Aperture Photometry pipeline (PDCSAP; Smith et al. 2012; Stumpe et al. 2012).<sup>25,26</sup> These targets also have light curves that were produced by community-created pipelines, including EVEREST (EPIC Variability Extraction and Removal for Exoplanet Science Targets; Luger et al. 2016, 2018) and K2SFF (Vanderburg & Johnson 2014).

We produced light curves for the superstamp targets using a moving aperture procedure with a 2-pixel-radius circular aperture (see also Rebull et al. 2018). These superstamp light curves show a common systematic: stars tend to brighten over the course of the Campaign. We median-combined the normalized light curves for our superstamp targets and then divided out this common systematic from each light curve. A typical example is provided in Appendix B to illustrate this procedure. The set of light curves is available for download.

With these high-precision light curves, we discovered the sub-Neptune K2-231 b transiting a solar twin (EPIC 219800881; Curtis et al. 2018), the warm brown dwarf CWW 89 Ab transiting another solar twin (EPIC 219388192; Curtis et al. 2016; Beatty et al. 2018),<sup>27</sup> and six EBs (Curtis 2016), three of which have been precisely characterized (EPIC 219394517, EPIC 219568666, and EPIC 219552514; Torres et al. 2018, 2019, 2020).

We visually inspected all of the pipeline-generated light curves available for every target.<sup>28</sup> We did not detect spot modulation variability in light curves for targets fainter than  $G = 16.5$  mag. These light curves suffered from low signal-to-noise ratio, so it is possible that the spot modulation amplitudes are too weak in comparison to the photometric noise (see Appendix D.6). It is also possible that the  $P_{\text{rot}}$  for these stars are too long compared to the duration of Campaign 7.

For the 151 non-WD stars with K2 data, we computed autocorrelation functions (ACFs; e.g., McQuillan et al. 2014) and Lomb–Scargle (LS) periodograms (Scargle 1982; Press & Rybicki 1989). For stars that clearly show rotational modulation, we also measured  $P_{\text{rot}}$  by fitting the timing of successive local maxima sets and minima sets (see, e.g., the discussion of

EPIC 219333882 in Appendix D.4. This final, visual method is important for correcting cases where the automated analyses detected half-period harmonics. It also allows us to identify data quality problems or, e.g., light curves affected by significant spot evolution midway through the Campaign. In most cases, the three methods yielded  $P_{\text{rot}}$  consistent to within 10% (after doubling the  $P_{\text{rot}}$  for those cases where the LS periodogram favored the half-period harmonic).

This approach is similar to the one we employed for NGC 6811 using Kepler data (Curtis et al. 2019a). The key difference is that for Ruprecht 147 we prefer the ACF  $P_{\text{rot}}$  to the LS  $P_{\text{rot}}$ . The ACF more accurately recovers  $P_{\text{rot}}$  in the spot modulation patterns, which more often double dip at the longer  $P_{\text{rot}}$  found in Ruprecht 147 stars compared to stars in younger clusters that more often exhibit sinusoidal modulation patterns (Basri & Nguyen 2018).

We measured preliminary periods for 68 stars, including 59 of the 105 main-sequence dwarfs ( $G > 10.5$ , ignoring red giants, blue stragglers, and stars at the main-sequence turnoff). Light curves for 11 other stars showed variability consistent with spot modulation, but we were unable to unambiguously assign a  $P_{\text{rot}}$  because the signal was confused by data quality problems, by interference with a neighbor blended in the K2 pixels, and/or by spot evolution. We do not report periods for the six EBs, as these are being analyzed separately (Curtis 2016; Torres et al. 2018, 2019, 2020).

Figure 3 shows the results of our light-curve analysis for one mid-K dwarf, EPIC 219651610; similar figures for all non-WD candidate members with K2 data are provided in the online journal (151 stars). Table 1 presents data for the entire 440-star membership catalog, including results for all K2 targets. We estimate a typical  $P_{\text{rot}}$  uncertainty of 10% for all targets with reported values; see Appendix D.8 for details.

See Gruner & Barnes (2020) for an independent analysis of the K2 data for Ruprecht 147 stars allocated individual apertures.

### 3.2. Measuring $P_{\text{rot}}$ with Light Curves from the Palomar Transient Factory

We monitored Ruprecht 147 from 2012 April 29 to 2012 October 7 as part of the PTF Open Cluster Survey (Agüeros et al. 2011, 2018; Covey et al. 2016; Kraus et al. 2017). This survey used the robotic 48-inch Oschin (P48) telescope at Palomar Observatory, CA. The P48 was equipped with the modified CFH12K mosaic camera: 11 CCDs, 92 megapixels, 1" sampling, and a 7.26 deg<sup>2</sup> field of view (Rahmer et al. 2008). Under typical conditions (1" seeing), it produced 2" FWHM images with a  $5\sigma$  limiting  $R_{\text{PTF}} \approx 21$  mag in 60 s (Law et al. 2010).

Two slightly overlapping PTF fields, each  $3.5 \times 2.3$ , covered the center of Ruprecht 147. The bulk of the cluster members later published in Curtis et al. (2013) fall in these two fields, centered at  $\alpha = 19:07:43.4$ ,  $\delta = -16:52:30.0$  and  $\alpha = 19:21:58.8$ ,  $\delta = -16:52:30.0$ . For most of the campaign, these fields were observed roughly three times a night, weather permitting. However, there were gaps in our coverage each month when PTF conducted its  $g$ -band and/or  $H\alpha$  surveys. The result is a set of  $R_{\text{PTF}}$  light curves with  $\approx 180$  points unevenly spaced over the roughly 5-month baseline for our observations. We typically only kept data taken in the first  $\approx 100$  days owing to long data gaps that followed. In the

<sup>24</sup> <https://keplerscience.arc.nasa.gov/data/k2-programs/GO7035.txt>

<sup>25</sup> <http://keplerscience.arc.nasa.gov/pipeline.html>

<sup>26</sup> Our preliminary results were based on K2 Data Release 9, whereas this manuscript uses Data Release 36: <https://keplerscience.arc.nasa.gov/k2-data-release-notes.html#k2-campaign-7>.

<sup>27</sup> This system was independently discovered by Nowak et al. (2017).

<sup>28</sup> Only cadences with `SAP_QUALITY=0` are used.

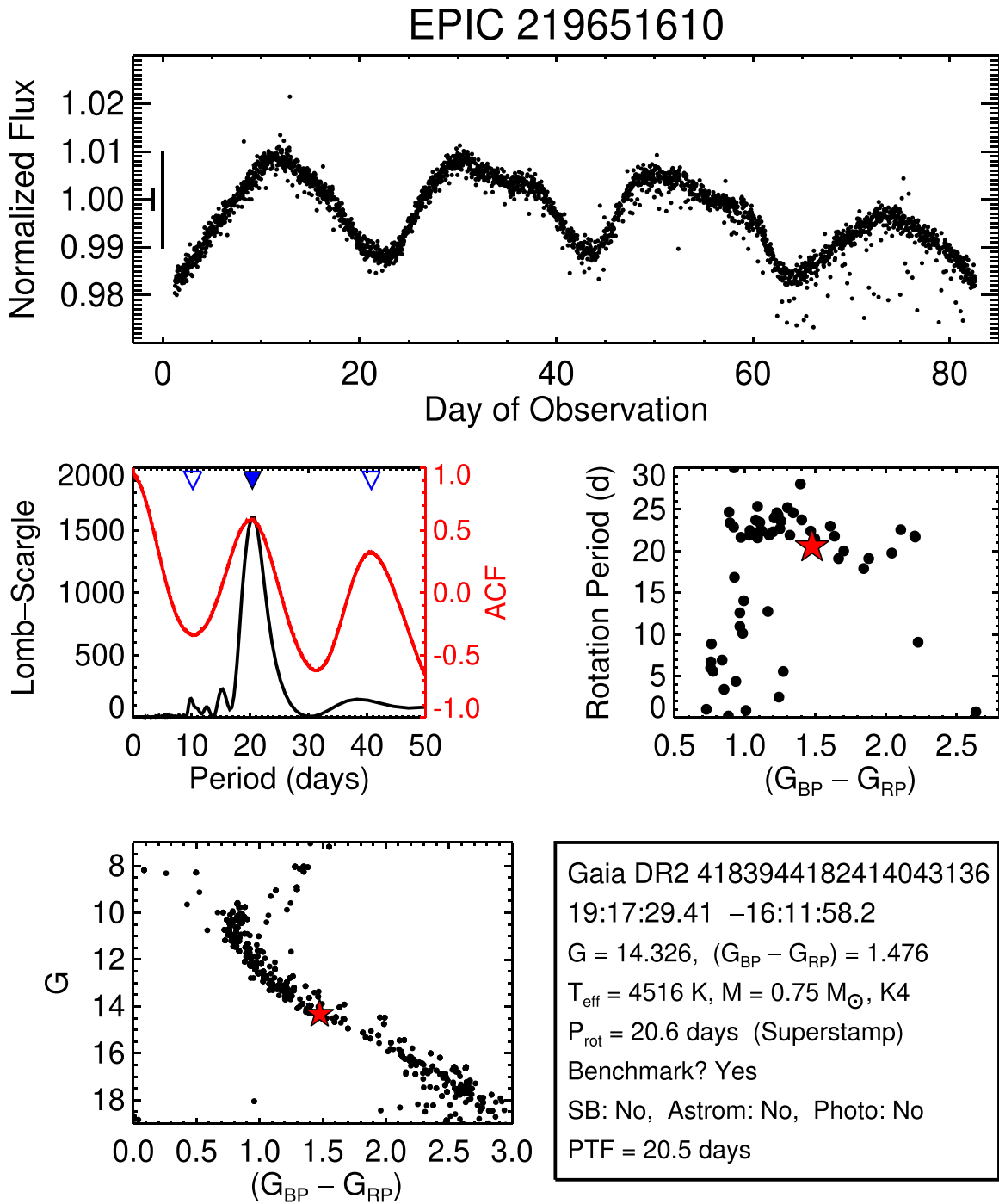


**Figure 3.** Analysis of K2 data for EPIC 219651610 (Gaia DR2 4183944182414043136, CWW 108, NOMAD 0738-0797617), a mid-K dwarf ( $T_{\text{eff}} = 4516$  K,  $M_{\star} = 0.75 M_{\odot}$ ) member of Ruprecht 147. Top: K2 light curve from the superstamp. Two vertical lines at left mark the photometric precision (“sigma\_LC”) and amplitude (“Rvar\_LC”), respectively. Middle left: periodicity is measured with the LS periodogram (left axis, black line) and ACF (right axis, red line). At top, the solid blue triangle marks the adopted period, and the open triangles mark the half and double values. Middle right:  $P_{\text{rot}}$  vs. ( $G_{BP} - G_{RP}$ ) for Ruprecht 147 (black points), along with the target star (red star). Bottom left: Gaia DR2 CMD for Ruprecht 147 and the target star (red star) is used to check for binary photometric excess. We also queried Gaia DR2 for objects within  $12''$  of the target ( $\approx 3$  pixels) and plot the apparent (cyan) and absolute (blue) magnitudes of any neighbors (none found near this target). This is useful for assessing whether blends could be responsible for the apparent rotation signal seen in the light curve. Bottom right: this information panel includes useful data for the target. Similar plots for all candidate members with K2 data are available in the online journal (151 total). (The complete figure set (151 images) is available.)

case shown in Figure 4, this left us with 142 data points collected on 48 nights spread across 102 days.

We sought to improve the photometric precision for our targets’ light curves by performing local differential photometry in the immediate vicinity of each target. We downloaded

the calibrated PTF images ( $8' \times 8'$  regions centered on each target) from the NASA/IPAC Infrared Science Archive (IRSA).<sup>29</sup> We identified all sources within  $\pm 1.5$  mag of the

<sup>29</sup> <https://irsa.ipac.caltech.edu/applications/ptf/>



target and calculated simple aperture photometry for these stars on all images. We then subtracted off the median magnitude for each star and median-combined the results for all stars to produce a light curve describing the systematic photometric zero-point. Finally, we subtracted this signal from the light curves for the target and all reference stars and then computed LS periodograms for the full sample with periods ranging between 0.1 and 80 days.<sup>30</sup> Some of the reference stars are themselves variables; phase-folded light curves for four examples are shown in Figure 15 in Appendix C to illustrate the photometric precision and range of measurable  $P_{\text{rot}}$  attainable with our procedure.

We applied this procedure to all stars on our list with  $13 \text{ mag} < G < 18 \text{ mag}$  (K to early M spectral types) with  $\Delta G < 0.5 \text{ mag}$  and, where available, RVs consistent with being single-star members (RVs are available for 22 stars). Our list included 128 targets, 56 of which had usable data from PTF (62 stars were not observed in our two fields, and 10 others suffered other data quality problems, including proximity to bright neighbors or diffraction spikes). Seven of our targets showed significant rotational modulation for which we report rotation periods, and nine others showed weak modulation.

Figure 4 shows the results for EPIC 219651610, the mid-K dwarf observed with K2 and presented in Figure 3 (similar figures for the other PTF rotators are available in the online journal). Remarkably, we measured  $P_{\text{rot}} = 20.6$  days from K2 and 20.5 days from PTF, despite the differences in photometric precision, cadence, and times of observation. To estimate the  $P_{\text{rot}}$  uncertainty, we calculate each half-width at half-maximum power of the primary peak in the periodogram to estimate upper and lower error bars, and we find a typical value of 10% for these stars ( $\approx 2$  days); see Appendix D.8 for additional discussion.

#### 4. The Ruprecht 147 Rotation Catalog

The Ruprecht 147 catalog, described in Table 1, includes identifiers from Gaia DR2, the K2 Ecliptic Plane Input Catalog (EPIC; Huber et al. 2016), 2MASS, NOMAD, and the CWW numbers from Curtis et al. (2013). It also includes astrometry from Gaia DR2 and proper motions from PPMXL for three stars lacking Gaia data, photometry from Gaia DR2 and 2MASS, RVs from Gaia DR2 and our own database (see footnote 18), stellar properties, and the results of our rotation period analyses. We also provide information on membership and binarity and list the  $G$  magnitude and radial angular distance to the brightest neighbor within  $12''$  to assess possible contamination for K2 targets.

##### 4.1. Crafting a Benchmark Sample of Rotators

We measured preliminary periods for 72 stars, including 64 main-sequence dwarfs. Seven of these  $P_{\text{rot}}$  were measured using PTF, including four stars not observed by K2. However, this raw sample suffers from a variety of problems.

First, this list includes seven SB2s and seven short-period SB1s. These stars are susceptible to tidal interactions, which

can alter the course of stellar angular momentum evolution and keep stars rotating rapidly or even spin them back up depending on the circumstances. For this reason, we remove such stars from our benchmark sample (14 stars; criteria were described in Section 2.3.1).

Second, we reject stars with excess luminosities from our sample because rotational modulation from binary components can confuse the light-curve analysis. In certain cases where the primaries are very inactive (e.g., late F to early G dwarfs), we are concerned that the rotational modulation apparent in some light curves might be solely attributable to more active lower-mass companions (e.g., EPIC 219404735 and EPIC 219442294; see also the discussion of EPIC 219661601 in Appendix D.3; designated “Benchmark” = “Yes-Prot\_Secondary?” in Table 1). Photometric binaries are also problematic because the rotation period signals from both components can be visible in the light curve. We speculate that the spot modulation signals from both components of nearly equal mass binaries are interfering and confusing the periodicity analysis. Furthermore, even when the light curves present a clean, periodic pattern, it is impossible to reliably associate the period with the appropriate binary component. Therefore, it is imperative that we remove all such binary candidates from our sample, regardless of their light-curve morphologies or rotation periods (13 stars total, including six of the SB2s and two of the short-period SB1s; criteria were described in Section 2.3.4).

Third, three stars show rotation periods that seem to be anomalously rapid for their mass and age. However, our Ca II H and K spectra (high resolution from MMT/Hectochelle and/or Magellan/MIKE, with high signal-to-noise ratios) demonstrate that these stars have inactive chromospheres, thus invalidating the apparently rapid rotation seen in the K2 light curves. For details, see Figure 17 in Appendix D.2.

After removing such stars from our sample, we are left with 39 dwarf rotators. Of these, 26 satisfy our criteria for single-star membership; the remainder are wide binary candidates based on their astrometry (e.g.,  $\Delta\mu > 2 \text{ mas yr}^{-1}$  and/or  $\text{RUWE} > 1.4$ ). The rejected stars are discussed in more detail in Appendix D, and their distribution in color–period space is shown in Figure 16.

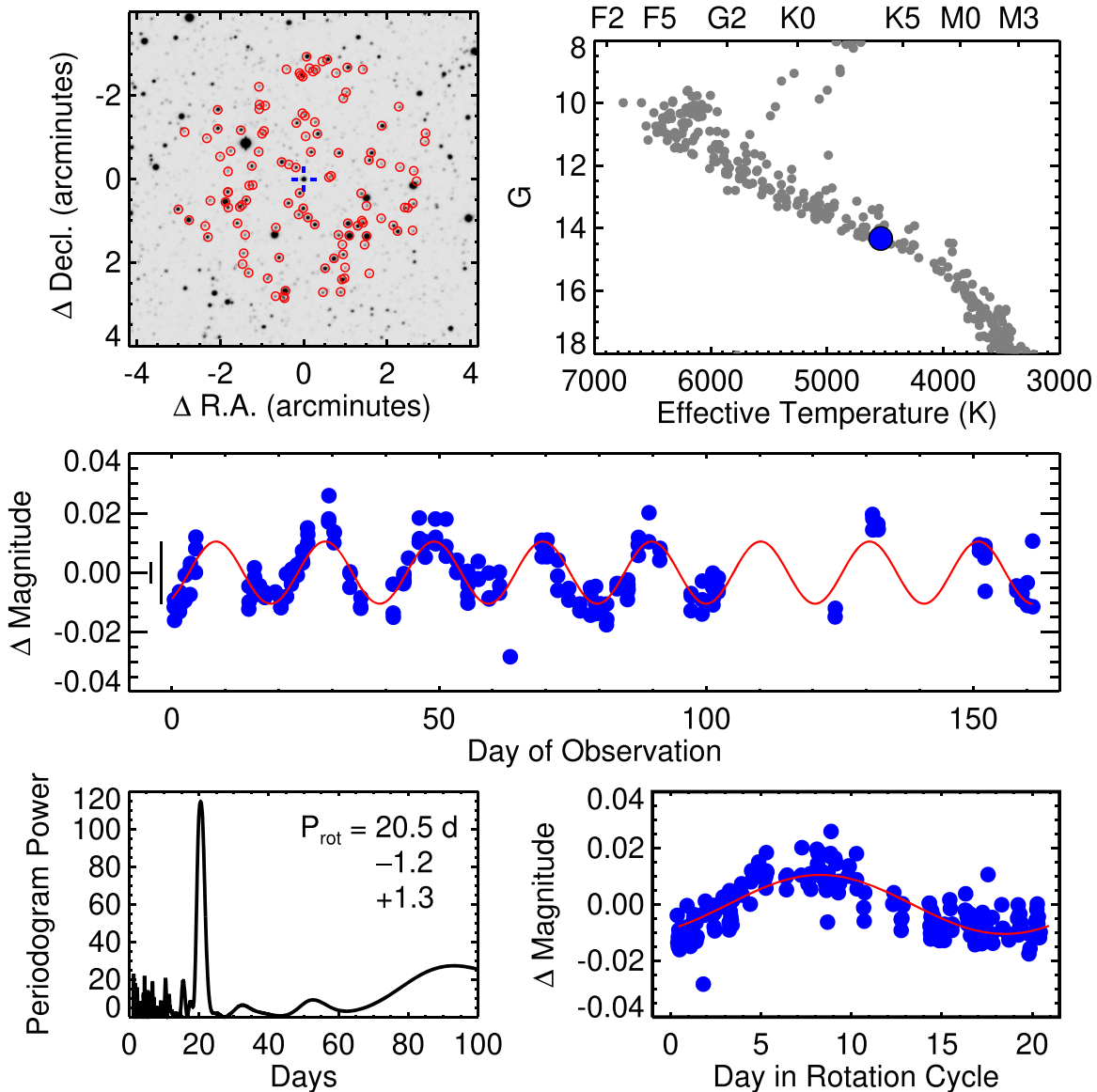
##### 4.2. The Ruprecht 147 $P_{\text{rot}}$ Distribution

Figure 5 presents the color–period distribution for the benchmark rotators. In this figure, we differentiate likely single stars from effectively single stars using different symbols and colors (red circles vs. blue squares). For this purpose, we define “effectively single” as stars satisfying photometric and RV criteria, but which have astrometry suggesting that they are wide binaries. We expect that the primary stars in such binaries evolve as if they were single stars in isolation, and their light curves are unaffected by their companions.

Our benchmark rotator sample spans  $0.62 < (G_{\text{BP}} - G_{\text{RP}})_0 < 2.09$ , corresponding to  $6350 \text{ K} > T_{\text{eff}} > 3700 \text{ K}$  and  $1.40 M_{\odot} > M_{\star} > 0.55 M_{\odot}$ . There are four warm, short-period rotators, which are not expected to have spun down significantly, as they have relatively thin convective envelopes and therefore weaker magnetic dynamos ( $0.5 \lesssim (G_{\text{BP}} - G_{\text{RP}})_0 \lesssim 0.6$ ). Figure 5 also shows that most stars with  $(G_{\text{BP}} - G_{\text{RP}})_0 > 0.8$  ( $T_{\text{eff}} < 5800 \text{ K}$ ,  $M_{\star} \lesssim 1 M_{\odot}$ ) congregate around  $P_{\text{rot}} \approx 22.5 \pm 1.6$  days, which appears to be the cluster’s slowly rotating sequence. That sequence is relatively flat compared to rotation period sequences for younger clusters, which tend to increase from relatively rapid G dwarfs to

<sup>30</sup> Although we preferred ACF for the K2 light curves, that technique requires evenly sampled time series. In double-dip light curves where the LS returned the half-period harmonic, the true period was always represented at a somewhat weaker power. For the PTF analysis, we identified stars as rotators that had unambiguous, single-peaked LS periodograms so as to avoid the half-period harmonic issue, i.e., we trust our  $P_{\text{rot}}$  measurements for stars with a single significant peak in the LS periodogram.

## EPIC 219651610



**Figure 4.** Analysis of the PTF data for EPIC 219651610, the star presented in Figure 3. Top left: PTF image of an  $8' \times 8'$  region centered on the target, marked with blue cross-hairs. Reference stars used to calibrate the light curves are highlighted with red circles ( $\Delta G \lesssim 1.5$  mag). Top right: temperature vs. Gaia DR2 apparent  $G$  magnitude for Ruprecht 147, with the target star highlighted in blue. The Gaia astrometry, the RVs collected by our team, and the proximity to the single-star main sequence collectively indicate that this star is likely a single member. Middle: PTF light curve, extracted with simple aperture photometry, and corrected using a systematics light curve generated with the reference stars shown in the image above. The photometric modulation due to rotating spots is apparent in this light curve. A sine curve fit to these data is overlaid in red to help illustrate the periodicity. Two vertical lines at left mark the photometric precision (“sigma\_LC”) and amplitude (“Rvar\_LC”), respectively. Bottom left: LS periodogram for the target shows a 20.5-day rotation period. The half-width at half-power values for the main peak provide estimates of the period uncertainty ( $\lesssim 10\%$  typically). Bottom right: phase-folded light curve. Similar plots for EPIC 219189038, EPIC 219234791, EPIC 219297228, EPIC 219333882, EPIC 218984438, and EPIC 219665690 are available in the online journal.

(The complete figure set (7 images) is available.)

slower M dwarfs (e.g., the figure shows that the single-star rotator sequence for Praesepe ranges from  $\approx 9$  to 19 days over the same span in color; Douglas et al. 2019).

#### 4.2.1. Candidate Blue Lurkers

Two rapid outliers appear to be single stars, according to all available astrometric, photometric, AO, and RV data. Furthermore, both stars, EPIC 219503117 (CWW 85,  $\log R'_{\text{HK}} = -4.44$  dex)

and EPIC 219692101 (CWW 97,  $\log R'_{\text{HK}} = -4.58$  dex), have anomalously high chromospheric emission, consistent with their rapid periods. These stars are solar twins, so we can compare them directly to the Sun, to solar twins in the field (Lorenzo-Oliveira et al. 2018), and to analogous stars in other clusters (e.g., the fully converged slow rotator sequence for Praesepe). According to all of these benchmarks, the behavior of these old, single, and rapidly rotating solar twins is anomalous.

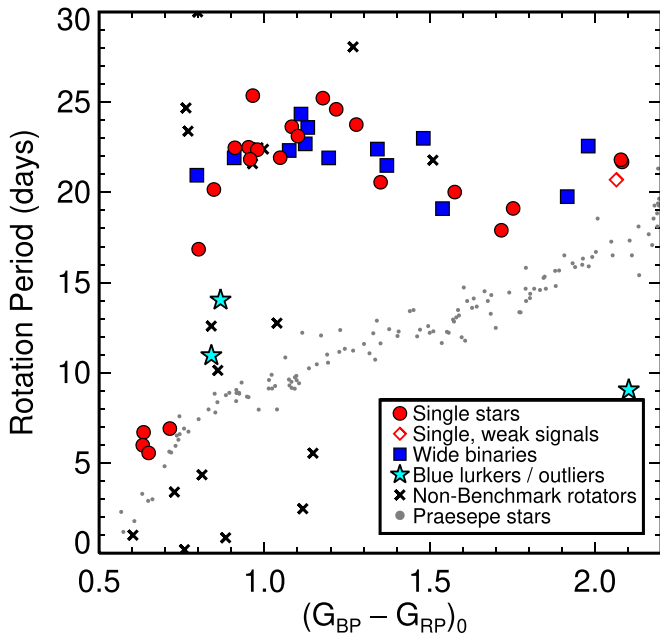


**Figure 5.** Color–period distribution for benchmark stars in Ruprecht 147. The slowly rotating sequence for Ruprecht 147 appears remarkably flat relative to Praesepe’s (small gray points, 670 Myr; Douglas et al. 2019) and other young clusters. Stars marked with crosses are removed from this sample because they have large photometric excesses or are short-period binaries (19 stars). Red circles mark single stars (according to photometry, astrometry, AO imaging where available, and RVs where available; 24 stars), while blue boxes mark “effectively single” wide binaries (single according to photometry and RVs where available, but have proper-motion deviations  $\Delta\mu > 2 \text{ mas yr}^{-1}$  and/or  $\text{RUWE} > 1.4$ , indicating that they are likely wide binaries; 12 stars). One star with a weak signal is shown with an open symbol to indicate that its period is not counted as validated and is caused by increased noise in its light curves relative to analogous cluster members. Three single stars (marked with cyan five-point-star symbols) appear as rapid outliers relative to the main Ruprecht 147 trend. Two are solar twins, which we tentatively classify as candidate blue lurkers—blue stragglers embedded in the main sequence (Leiner et al. 2019). One is an M1 dwarf, which is rotating at twice the rate as Praesepe’s slow sequence, suggesting to us that it might be a short-period binary, a blue lurker, or otherwise anomalous. See Figure 16 in Appendix D for details on the nonbenchmark rotators and stars within invalidated periods.

This is different behavior than found for EPIC 219388192 (CWW 89 A), which Curtis et al. (2016) discovered harbors a warm, transiting brown dwarf and a distant M dwarf companion (see also Nowak et al. 2017; Beatty et al. 2018). In that case, a  $4 \text{ km s}^{-1}$  discrepancy in its systemic RV and a near-IR excess suggested the presence of a stellar companion, which was directly imaged with Keck/NIRC2. More critically, the K2 light curve revealed transits indicating a Jupiter-sized object, which the RV time series confirmed was a brown dwarf orbiting every 5.3 days. Curtis et al. (2016) speculated that the tidal interaction with the brown dwarf is responsible for that star’s rapid rotation and overactive chromosphere. In contrast, the high-precision RV time series for CWW 85 and CWW 97 from TRES and HARPS all but rule out the presence of tidally interacting companions.

Leiner et al. (2019) found similar stars with anomalously rapid rotation in their survey of M67 (as well as rapidly rotating SB1s with long orbital periods where tides should be ineffective). They concluded that such stars are blue stragglers (i.e., stars that received a large influx of mass via accretion from or merger with a stellar companion). However, in contrast to the classic, higher-mass blue stragglers that are found at

warmer  $T_{\text{eff}}$  beyond the main-sequence turnoff, these are embedded in the main sequence and are referred to as “blue lurkers” by Leiner et al. (2019). Perhaps the two rapidly rotating and single solar twins we have identified in Ruprecht 147 are blue lurkers that were formed via mergers, leaving behind isolated blue stragglers with no other companions or remnants. Alternatively, perhaps they are indeed binaries with low-mass companions and orbits oriented nearly in the plane of the sky.

Figure 5 shows a third rapid outlier—the M1 dwarf EPIC 219690421 ( $T_{\text{eff}} \approx 3740 \text{ K}$ ,  $M_* \approx 0.54 M_{\odot}$ ,  $(G_{\text{BP}} - G_{\text{RP}})_0 = 2.10$ ), which is the faintest and reddest star in our rotation sample. The K2 light curve shows a 9.1-day periodicity, and we detected an 8.8-day signal in the PTF light curve, albeit with a periodogram power below our quality threshold. Analogous stars in Praesepe are rotating at 17.3 days. Furthermore, the Praesepe sequence is tightly converged at this temperature, with only two outliers out of 23 stars within 100 K in the single-star sequence presented by Douglas et al. (2019). This means that EPIC 219690421 appears to rotate nearly twice as fast as analogous 670 Myr old stars. Based on the comparison with Praesepe, we do not consider this star to be a suitable benchmark for single-star rotation, as it does not seem like it could be representative of 2.7 Gyr old M1 dwarfs. Unfortunately, we do not have any RV data to assess its binarity, nor an optical spectrum that we could use to diagnose enhanced chromospheric activity via  $\text{H}\alpha$  emission. It will be important to determine its membership and binarity with RV monitoring (and for the other stars currently lacking RVs for that matter) before we can hope to explain the cause for its rapid rotation (is it a tidally interacting binary, a blue lurker, or have  $0.55 M_{\odot}$  stars not fully converged yet?). As this star has the lowest mass in our sample, ignoring it effectively refocuses this study on stars more massive than  $0.55 M_{\odot}$ .

These three stars are designated as “Benchmark” = “Yes-Rapid\_Outlier” in Table 1.

#### 4.3. The Role of Binaries in Shaping the Color–Period Distribution

Rapid outliers in color–period distributions are often short-period binaries (see Figure 16 in Appendix D), but not all binaries appear as outliers. Of the 39 rotators in our benchmark rotator sample, we classify 12 as wide binary candidates based on the Gaia DR2 excess astrometric noise (i.e.,  $\text{RUWE} > 1.4$ ) or large deviation in the proper motion ( $\Delta\mu > 2 \text{ mas yr}^{-1}$ ). All of these candidate long-period binaries are found on the slow sequence in Figure 5. In addition, considering those stars we removed from our benchmark sample, two of the candidate short-period binaries and two photometric binaries are also found on the slow sequence.

The components of long-period binaries should not be affected by gravitational tides (except maybe in rare cases where highly eccentric orbits result in close encounters), nor will the primary’s photometric color necessarily be biased strongly by the secondary (assuming that the primary hosts the rotation period signal). And any impact wide binaries might have on initial rotation rates, perhaps by prematurely dispersing circumstellar disks, will be largely erased through 2.7 Gyr of convergent spin-down. For these reasons, we keep these 12 wide binary systems in our benchmark sample.

We will continue to follow up on these binary, candidate binary, and likely single stars to better determine the properties of each system to study how binarity affects spin-down.

#### 4.4. *There is No Undetected Population of Very Slowly Rotating K Dwarf Cluster Members*

We reported periods for only 21 out of 64 benchmark stars with  $0.50 M_{\odot} \lesssim M_{\star} \lesssim 0.85 M_{\odot}$  ( $3700 \text{ K} \lesssim T_{\text{eff}} < 5000 \text{ K}$ ,  $2.17 \gtrsim (G_{\text{BP}} - G_{\text{RP}})_0 \gtrsim 1.11$ ), or  $\approx 33\%$  of the targets. This includes 17 periods measured from K2 and four from PTF. The periods for all range between 18 and 25 days, except for the rapid 9-day M1 dwarf noted earlier. Given the relatively short duration of Campaign 7, the presence of persistent systematics in the light curves, and expectations from standard gyrochronology models for much longer  $P_{\text{rot}}$  (30–40 days), it is natural to wonder whether we are missing a substantial number of longer-period cool rotators. Unfortunately, only 19 of these benchmark targets were observed by K2. We successfully measured  $P_{\text{rot}}$  for 17 of these, so the recovery rate is actually quite high at 89%,<sup>31</sup> and it is on par with the rates for the K2 surveys of the Hyades and Praesepe clusters (85%–88%; Douglas et al. 2017, 2019), despite those clusters being only 25% of the age of Ruprecht 147 ( $\approx 700 \text{ Myr}$  vs. 2.7 Gyr).

Regarding the two nondetections, in Figure 18 in Appendix D.6 we examine the photometric noise and spot amplitudes for all targets, and we find that the light curve for EPIC 219616992 is  $6.7\times$  noisier than analogous targets, which is suppressing our sensitivity to the rotation signal. Still, we see evidence for a 20.7-day period in a smoothed version, which the LS analysis also picks up (this  $P_{\text{rot}}$  is listed as a negative value in Table 1 to distinguish it from stars with validated periods). As for EPIC 219141523, the PDCSAP and EVEREST light curves show long-period variations that could be caused by rotating spots, but there is no obvious periodicity. The PTF light curve is noisier than those for stars with measured periods, and we see no convincing period; the LS periodogram does show a weak peak at 30 days.

Unfortunately, Ruprecht 147 has not provided us with hundreds of rotators like the rich Pleiades and Praesepe clusters. The K2 surveys of the Pleiades and Praesepe have spoiled us, in a way, so that we expect large returns from these high-quality data. However, Ruprecht 147 is a very sparse cluster with a top-heavy mass function. It might be more fair to call it a cluster remnant, as it has clearly suffered from extreme dynamical evolution and mass loss (Curtis 2016; Yeh et al. 2019). Still, we are encouraged by the high rate of success for those 19 benchmark targets observed by K2.

The two nondetection cases together with the rapid M1 dwarf are the three lowest-mass stars in this particular sample. Refocusing on those with  $M_{\star} > 0.55 M_{\odot}$ , we measured validated  $P_{\text{rot}}$  for every benchmark target observed by K2 and found that all share a common  $P_{\text{rot}}$  to within a few days.

<sup>31</sup> See Appendices D.4 and D.6 for remarks on EPIC 219346771 and EPIC 219675090. The  $P_{\text{rot}}$  for these stars are not immediately obvious from looking at the light curve; however, we measured their  $P_{\text{rot}}$  by timing the arrivals of their minima, and we consider our values to be accurate. Even if one rejects their  $P_{\text{rot}}$  as inconclusive, the recovery rate for this sample would still be 79%.

## 5. Stellar Rotation at 2.7 Gyr with Ruprecht 147 and NGC 6819

Ruprecht 147 is approximately coeval with the 2.5 Gyr old open cluster NGC 6819, which was surveyed during the primary Kepler mission (a literature review of its fundamental properties is provided in Appendix E). Meibom et al. (2015) presented  $P_{\text{rot}}$  for 30 NGC 6819 dwarfs with masses greater than  $M_{\star} \gtrsim 0.85 M_{\odot}$ . Unfortunately, because of the great distance to NGC 6819 ( $\approx 2.5 \text{ kpc}$ ), lower-mass members remained inaccessible to Kepler. As a result, our  $P_{\text{rot}}$  sample for Ruprecht 147 extends to lower masses than does the Meibom et al. (2015) catalog, primarily because Ruprecht 147 stars are  $\approx 77\times$  brighter than analogous stars in NGC 6819 (see Figure 20 in Appendix E). However, the K2 light curves suffer increased systematics due to the increased pointing instability of the spacecraft. This made it relatively more challenging to measure  $P_{\text{rot}}$  for the inactive late F and early G stars in Ruprecht 147 compared to NGC 6819.

The result is that the NGC 6819 sample is primarily composed of F and G dwarfs, whereas the Ruprecht 147 sample is primarily mid-G to early M dwarfs. Fortunately, because the two clusters are approximately coeval, we can combine their data to form a  $\approx 2.7 \text{ Gyr}$  sample that covers a larger range in mass than is possible with just one of the two.

### 5.1. *Gyrochronology Confirms that NGC 6819 and Ruprecht 147 Are Approximately Coeval*

Before examining the rotation samples for Ruprecht 147 and NGC 6819, we must determine whether their mean interstellar reddening values are determined consistently. To do this, we make use of each cluster’s red clump population, which should have nearly identical intrinsic luminosities. Differences in apparent photometric magnitudes can therefore be attributed to differences in distance and interstellar extinction and reddening. Appendix E describes our procedure: using Ruprecht 147 as a reference, we find  $(m - M)_0 = 11.97$  and  $A_V = 0.44$  for NGC 6819.

In the left panel of Figure 6, we plot the Gaia DR2 CMDs for NGC 6819 and Ruprecht 147 with dereddened color and absolute magnitudes. The red clumps align by design. The main sequences and subgiant branches also approximately align, supporting the conclusion from our literature review that the clusters are approximately coeval. The presence of differential reddening across NGC 6819 (Platais et al. 2013; Anthony-Twarog et al. 2014) and the persistent uncertainty in its metallicity preclude a more precise derivation of their relative ages from their CMD morphologies. Eventually, the asteroseismic analysis of Ruprecht 147’s evolved stars should enable an independent measurement of their relative ages; however, this will still require measuring a more precise metallicity of NGC 6819 relative to Ruprecht 147.

The right panel of Figure 6 plots the color–period distributions for NGC 6819 and Ruprecht 147. The  $P_{\text{rot}}$  samples for each cluster overlap most significantly between  $5000 \text{ K} < T_{\text{eff}} < 5500 \text{ K}$ : over this range, for NGC 6819  $P_{\text{rot}} = 21.3 \pm 1.0$  days (nine stars; median and standard deviation) and for Ruprecht 147  $P_{\text{rot}} = 22.4 \pm 1.2$  days (nine stars).

Analogous stars in this  $T_{\text{eff}}$  range in the 1 Gyr old NGC 6811 lag behind the projection of the 670 Myr old Praesepe rotation sequence to 1 Gyr using the Skumanich law (see Figure 5 in

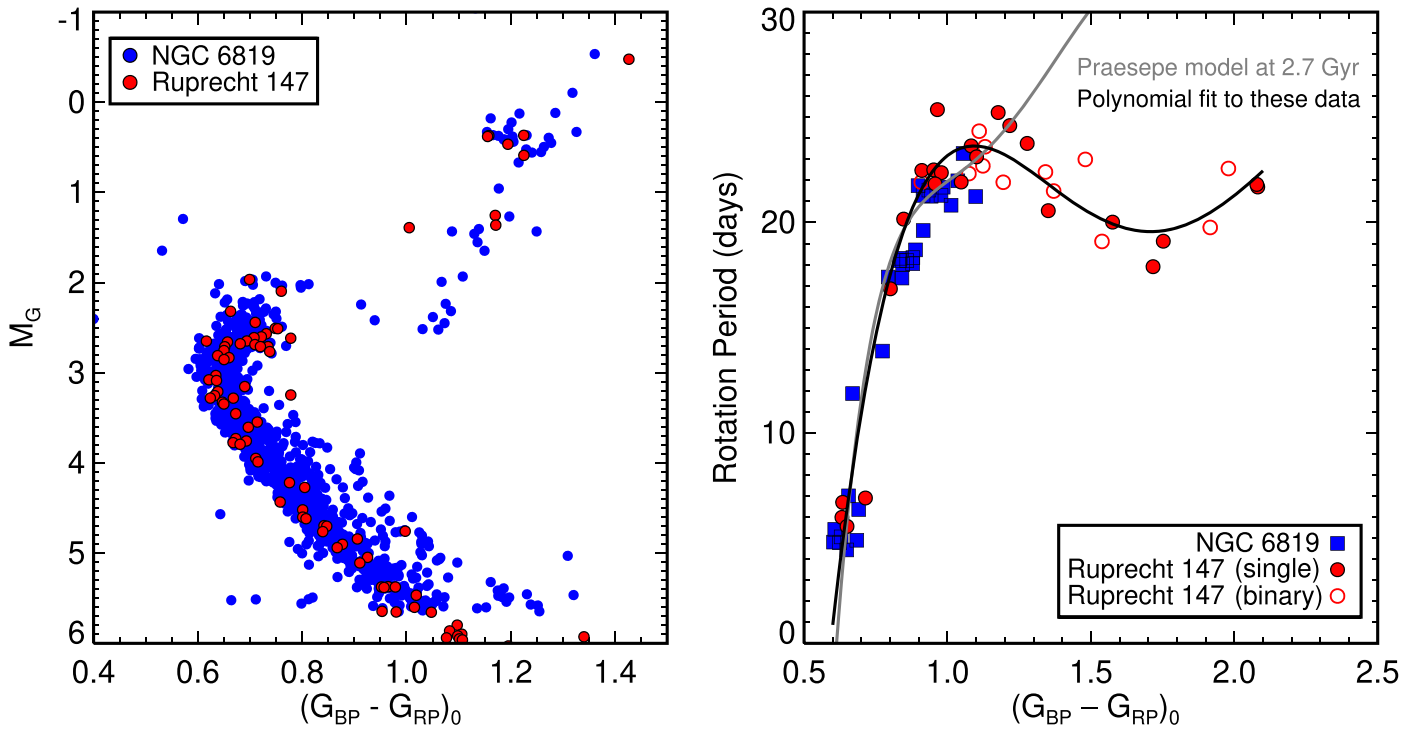


**Figure 6.** Left: dereddened Gaia DR2 color vs. absolute magnitude for the 2.5 Gyr old NGC 6819 (blue points; members from Cantat-Gaudin et al. 2018, with spectroscopic binaries and RV nonmembers from Milliman et al. 2014 removed) and the 2.7 Gyr old Ruprecht 147 (red points). For Ruprecht 147, we applied  $(m - M)_0 = 7.4$  and  $A_V = 0.30$ ; for NGC 6819, we calculated the values needed to align each cluster’s red clump stars (Table 6), which should have approximately equal absolute magnitudes in all photometric bands. We find  $\delta A_V = 0.14$  and  $\delta(m - M)_0 = 4.57$ , corresponding to  $A_V = 0.44$  and  $(m - M)_0 = 11.97$  for NGC 6819. The main sequences and subgiant branches also approximately align, indicating that the clusters are approximately coeval. Right: color–period diagram for NGC 6819 (blue squares; Meibom et al. 2015) and benchmark members of Ruprecht 147 (red circles), divided into singles (filled) and long-period binaries (open). The Ruprecht 147 sample extends much redder than the NGC 6819 sample and appears remarkably flat compared to expectations from standard gyrochronology models, represented by the gray line showing a polynomial fit to Praesepe that is projected forward to 2.7 Gyr with  $n = 0.62$  (tuned with the Sun; Douglas et al. 2019). Also shown is a polynomial fit to these  $P_{\text{rot}}$  data (black line); while the 2.7 Gyr slow sequence is flat compared to past expectations, this model emphasizes that the sequences in fact appear somewhat curved, where the G dwarfs are spinning more slowly than the K dwarfs. The largest overlap between the NGC 6819 and Ruprecht 147 rotation sequences occurs for  $0.91 < (G_{BP} - G_{RP})_0 < 1.09$  ( $5000 < T_{\text{eff}} < 5500$  K): the Ruprecht 147 stars in this range are on average slower by  $\approx 1$  day, corresponding to it being only 8% older. This is consistent with the the somewhat redder and fainter top of the main-sequence turnoff in the left panel of this figure, as well as the literature ages for each cluster.

Curtis et al. 2019a). However, by 2.5 Gyr these stars have clearly resumed spinning down, and we hypothesize that they do so following a Skumanich-like law, meaning continuously and with a common braking index. Therefore, the similarity in the average  $P_{\text{rot}}$  for the  $5000 \text{ K} < T_{\text{eff}} < 5500 \text{ K}$  stars in NGC 6819 and Ruprecht 147 reinforces the conclusion from CMD analyses that the clusters are approximately coeval.

Applying the  $n = 0.62$  braking index (tuned by comparing solar-color stars in Praesepe with the Sun; Douglas et al. 2019) using the Ruprecht 147 sequence as a reference, we calculate gyrochronology ages for the nine NGC 6819 stars in this  $T_{\text{eff}}$  range and find  $2.5 \pm 0.2$  Gyr, which is only 7% younger than Ruprecht 147. This calculation is relatively insensitive to the actual braking index because the  $P_{\text{rot}}$  values are so similar between the clusters. For example, varying  $n$  by  $\pm 0.3$  would modify the gyrochronological age of NGC 6819 by  $< 10\%$ .

### 5.2. The Joint 2.7 Gyr Rotator Sample

In total, we have 35 benchmark rotators for Ruprecht 147 (23 of which are likely single stars, not counting the two blue lurkers and rapid M dwarf) and another 30 rotators from NGC 6819, for a total of 66 stars. There is a notable lack of rotators with  $6000 \text{ K} < T_{\text{eff}} < 6200 \text{ K}$ , and there is a similar dearth in the Kepler field (see the top right panel of Figure 7). This suggests that  $P_{\text{rot}}$  is very challenging to measure for such

old stars in this  $T_{\text{eff}}$  range, as they have crossed into a very inactive regime.

While the NGC 6819 rotator sample was limited to  $M_* > 0.85 M_\odot$ , the addition of the Ruprecht 147 rotators extends the joint 2.5–2.7 Gyr sample down to  $M_* \approx 0.55 M_\odot$  and includes 20 stars with masses below the NGC 6819 sample limit.

The joint sequence can be approximately described by a polynomial model, as shown in the right panel of Figure 6. The dispersion about the fit is 1.18 days, with a median percent deviation of 5% and a maximum deviation of 12%. The formula is provided in Table 4, and details are provided in Appendix A.3.

## 6. Discussion

### 6.1. Stars Do Not Spin Down Continuously: The Case for a Temporary Epoch of Stalled Braking

Early empirical gyrochronology models posited that stars spin down continuously with a common braking index that is constant in time:  $P_{\text{rot}} \propto t^n$ , with  $n = 0.5$  according to Skumanich (1972). In this framework, the mass dependence is then described by a separate function independent of age and derived from young open cluster color–period sequences (e.g., Barnes 2003, 2007; Angus et al. 2019). While the coefficients

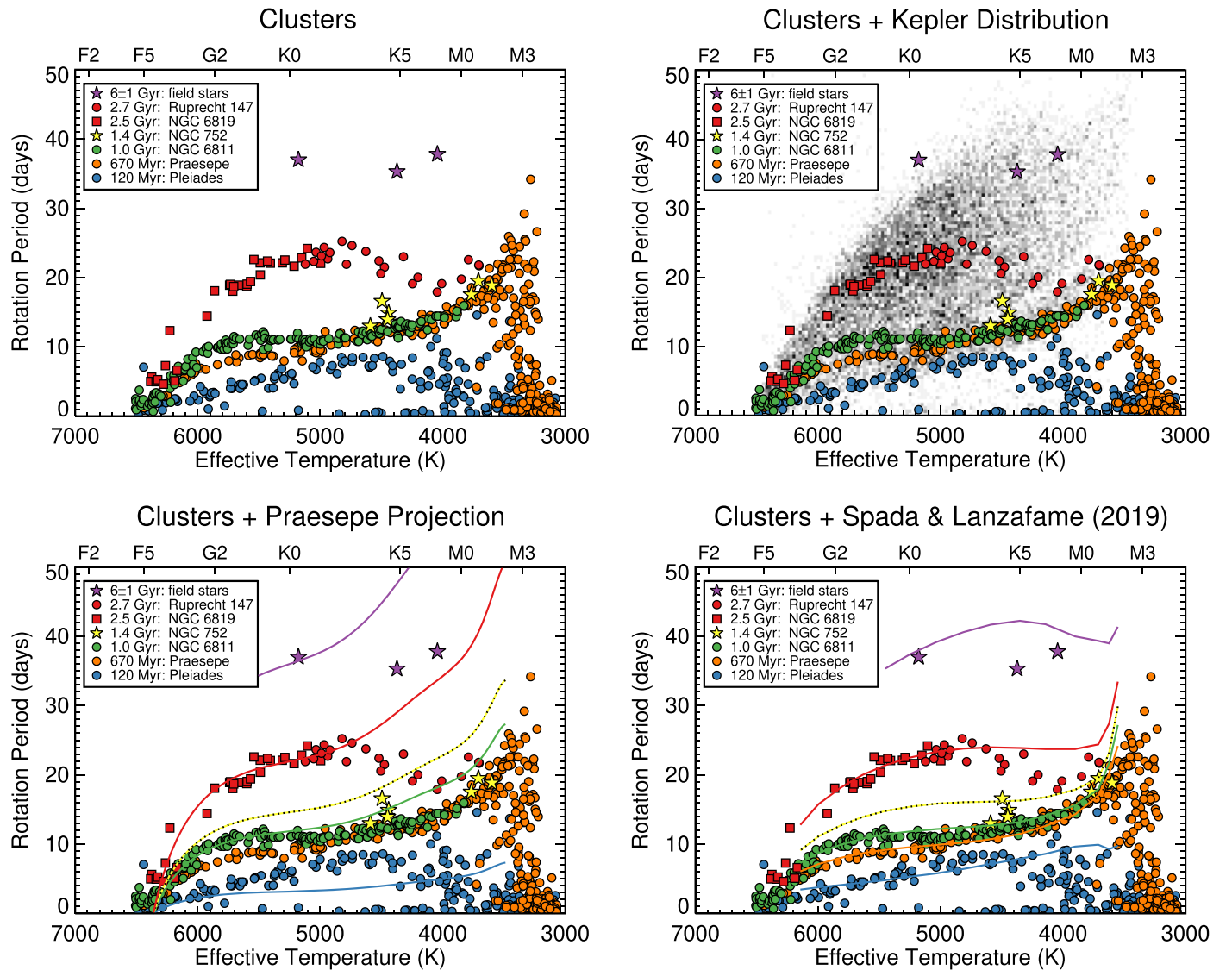


**Figure 7.** Top left:  $P_{\text{rot}}$  data for benchmark populations (data provided in Table 5), including the Pleiades (120 Myr; Rebull et al. 2016), Praesepe (670 Myr; Douglas et al. 2017, 2019), NGC 6811 (1 Gyr; Curtis et al. 2019a), NGC 752 (1.4 Gyr; Agüeros et al. 2018), NGC 6819 (2.5 Gyr, and projected forward in time to 2.7 Gyr to better match the Ruprecht 147 sample; Meibom et al. 2015), Ruprecht 147 (2.7 Gyr; this work), and three old K dwarfs:  $\alpha$  Cen B and 61 Cyg A and B ( $6 \pm 1$  Gyr). The Ruprecht 147 data show that the stars that were stalled between the ages of Praesepe and NGC 6811 have resumed spinning down by 2.7 Gyr. Temperatures are computed from Gaia DR2  $(G_{\text{BP}} - G_{\text{RP}})_0$  colors using our color-temperature relation presented in Appendix A.1. Colors are dereddened using  $E(G_{\text{BP}} - G_{\text{RP}}) = 0.415 A_V$ , with cluster  $A_V$  values provided in Appendix A.3. Top right: same data as the first panel, along with a binned subset of the Kepler field distribution (McQuillan et al. 2014), focusing on single dwarfs within 1000 pc to minimize bias and smearing due to interstellar reddening. The Kepler colors are dereddened using the  $E(B - V) = 0.04 \text{ mag kpc}^{-1}$  law, which approximates the median reddening pattern derived in Appendix F, and temperatures are calculated using our color-temperature relation. The data are binned by 25 K and 0.5 days. Bottom left: same data as the first panel, along with Praesepe-based gyrochrones (a polynomial fit to the Praesepe slow sequence, scaled according to  $(t_*/t_{\text{Prae.}})^{0.62}$ ). While this model works well for G dwarfs, for populations older than Praesepe, the models flare up to very long periods at temperatures cooler than  $T_{\text{eff}} \lesssim 5000$  K. Bottom right: same data as the first panel, along with the Spada & Lanzafame (2020) core-envelope coupling model evaluated at representative ages for this sample (120 Myr, 700 Myr, 1.0 Gyr, 1.5 Gyr, 2.5 Gyr, and a projection of the solar age model to 6 Gyr using  $n = 0.5$ ). This model fits the joint 2.7 Gyr sample (NGC 6819 + Ruprecht 147).

have been recalibrated using a variety of empirical data (e.g., Mamajek & Hillenbrand 2008; Meibom et al. 2009b; Angus et al. 2015), this class of model has been unable to accurately describe the color-period distributions of all benchmark clusters.

Over the past decade, study after study found that the  $P_{\text{rot}}$  distributions for pairs of young clusters ( $\leq 1$  Gyr) do not align when projecting one population to the age of the other using the Skumanich law (e.g., Meibom et al. 2009b, 2011a, 2011b; Cargile et al. 2014; Barnes et al. 2015, and including the Pleiades, Blanco 1, M35, M34, the Hyades, M48, and NGC 6811). But it was not clear in those studies whether

these discrepancies could be resolved with a color-dependent (but time-independent) braking index, whereby K dwarfs simply have a smaller  $n$  than G dwarfs, and they spin down continuously following that different power law.

This is no longer a viable solution. Agüeros et al. (2018) found that  $P_{\text{rot}}$  data for the 1.4 Gyr old NGC 752 cluster overlapped with the Praesepe sequence at  $M_* \approx 0.5 M_{\odot}$ , despite being twice as old (700 Myr older). Then, when examining the color-period distribution for the 1 Gyr old cluster NGC 6811, Curtis et al. (2019a) found that the converged slow sequence departed from models at  $M_* < 0.95 M_{\odot}$  and merged seamlessly with the Praesepe

sequence at  $M_* \approx 0.7 M_\odot$ , despite being 40% older in age (300 Myr).

Furthermore, Curtis et al. (2019a) found that a color-dependent braking law tuned with Praesepe and NGC 6811 cannot reproduce the observed Kepler  $P_{\text{rot}}$  distribution. In such a scenario, the universe is not old enough for K dwarfs to spin all the way down to the 30- to 40-day periods measured in the field (McQuillan et al. 2014).

These studies concluded that stars temporarily stop spinning down after converging on the slow sequence and that stars remain stalled for an extended period of time before spin-down resumes. Based on where the Praesepe, NGC 6811, and NGC 752 sequences overlapped, the duration of this temporary epoch of stalled spin-down must increase toward lower stellar masses.<sup>32</sup>

To illustrate the impact of stalling on gyrochronal ages, consider the case of the wide binary 61 Cyg A and B. Using empirical gyrochronology formulae, we infer ages for the pair of 2 Gyr (Barnes 2007), 3.5 Gyr (Mamajek & Hillenbrand 2008), 3.7 Gyr (Barnes 2010), and 2.9 Gyr (Angus et al. 2019). However, because 61 Cyg A and B are so bright, they have been extensively studied and have interferometric radius measurements, which Kervella et al. (2008) used to constrain their ages to  $6 \pm 1$  Gyr. Assuming that this age is correct, the gyrochronology ages are all systematically too young by 40%–70%. We suggest that this is due to the fact that these models assume, incorrectly, that stars spin down continuously. To repair such models, the mass-dependent stalling timescale must be determined.

## 6.2. Building a Sample of Benchmark Rotator Data

To this end, we build a sample of benchmark  $P_{\text{rot}}$  data. To characterize rotational behavior at younger ages, we use the data for the Pleiades (120 Myr; Rebull et al. 2016; see also Stauffer et al. 2016), Praesepe (670 Myr; Douglas et al. 2019; see also Douglas et al. 2017; Rebull et al. 2017), NGC 6811 (1.0 Gyr; Curtis et al. 2019a; see also Meibom et al. 2011a), and NGC 752 (1.4 Gyr; Agüeros et al. 2018). Polynomial fits to these cluster sequences are provided in Table 4, are described in Appendix A.3, and are plotted in Figures 12 and 13. The  $P_{\text{rot}}$  catalog for these clusters is provided in Table 5.

We also include three old K dwarfs in our analysis (properties summarized in Table 3):<sup>33</sup>  $\alpha$  Cen B and the wide binary 61 Cyg A and B.

The star  $\alpha$  Cen B appears as a long-period outlier in a relatively sparse region of the  $P_{\text{rot}}$  distribution for the Kepler field, shown in the top right panel of Figure 7. The upper envelope of this field distribution approximately corresponds to a line of constant Rossby number  $\text{Ro} = 1.70$  using the Cranmer & Saar (2011) convective turnover time formula (see also the discussion of a detection edge at  $\text{Ro}_{\text{thresh}} = 2.08$  in Section 3.1 of van Saders et al. 2019). Whereas the  $P_{\text{rot}}$  measured from Kepler require brightness modulations in broadband visual light, the  $P_{\text{rot}}$  for  $\alpha$  Cen B was measured

<sup>32</sup> Douglas et al. (2019) found that solar-type Hyads rotate 0.4 days slower than analogs in Praesepe, indicating that the Hyades cluster is 60 Myr older than Praesepe. However, the lower-mass  $P_{\text{rot}}$  sequences for each cluster precisely overlapped, which Douglas et al. (2019) interpreted as further evidence for the mass-dependent stalled braking phenomenon.

<sup>33</sup> The Living with a Red Dwarf program is also building a catalog of ages, rotation periods, and X-ray luminosities for nearby low-mass stars (Guinan & Engle 2009; Engle & Guinan 2018). Guinan & Engle (2019) provide their latest age- $P_{\text{rot}}$  relations for M dwarfs.

**Table 3**  
Data for Old, Nearby Benchmark K Dwarfs

Name	Age (Gyr)	$(G_{\text{BP}} - G_{\text{RP}})_0$ (mag)	$T_{\text{eff}}$ (K)	$\log g$ (dex)	[Fe/H] (dex)	$P_{\text{rot}}$ (days)
$\alpha$ Cen B	$6 \pm 1$	(1.0222)	5178	4.56	+0.23	37
61 Cyg A	$6 \pm 1$	1.4450	4374	4.63	-0.33	35.3
61 Cyg B	$6 \pm 1$	1.6997	4044	4.67	-0.38	37.8
36 Oph A	...	1.0561	5100	...	-0.27	20.7
36 Oph B	...	1.0470	5124	...	-0.25	21.1
36 Oph C	...	1.4033	4428	...	-0.20	18.0

**Note.**  $\alpha$  Cen B:  $T_{\text{eff}}$ ,  $\log g$ , and [Fe/H] are taken from the Spectroscopic Properties Of Cool Stars catalog (SPOCS; Valenti & Fischer 2005). The Gaia DR2 color is predicted from our color-temperature relation (see Appendix A.1, Figure 11). The age is the mean calculated by Mamajek (2014) from several studies, including those of Thévenin et al. (2002), Thoul et al. (2003), Eggenberger et al. (2004), Miglio & Montalbán (2005), Yıldız (2007), and Bazot et al. (2012), and is consistent with the age found by Spada & Demarq (2019). The  $P_{\text{rot}}$  was measured from X-ray and UV data (DeWarf et al. 2010; Dumusque et al. 2012). 61 Cyg A & B:  $T_{\text{eff}}$ ,  $\log g$ , and [Fe/H] are taken from the Gaia FGK Benchmark catalog (Heiter et al. 2015), the age is from Kervella et al. (2008), and the  $P_{\text{rot}}$  were measured from Ca II H and K monitoring (Donahue et al. 1996; Boro Saikia et al. 2016). 36 Oph A, B, C:  $T_{\text{eff}}$  calculated using our Gaia DR2 color-temperature relation (see Appendix A.1, Figure 11). The metallicities are averages of the values listed in SIMBAD. For a detailed review of the  $P_{\text{rot}}$  values, see footnote 28 in Barnes (2007), which drew on measurements reported by Donahue et al. (1996) and Baliunas et al. (1983).

from variations in coronal and chromospheric emission observed in the UV, X-ray, and Ca II H and K. The  $P_{\text{rot}}$  for 61 Cyg A and B were also measured from Ca II H and K modulation. With Rossby numbers of 1.73 and 1.80, the magnetic dynamos for these stars are relatively inactive as well. The  $P_{\text{rot}}$  for similarly old stars in the field are likely to remain largely elusive in photometric time series surveys.

## 6.3. The Flat 2.7 Gyr Color-Period Sequence: A Product of Mass-dependent Stalling

The panels of Figure 7 show  $P_{\text{rot}}$  data for the benchmark samples, including our new measurements for Ruprecht 147. The 2.7 Gyr rotation period sequence appears remarkably flat, with most stars cooler than  $T_{\text{eff}} = 5700$  K rotating within a narrow range of  $P_{\text{rot}} = 22 \pm 2$  days. This is in sharp contrast to the steep mass dependence seen in younger clusters like the Pleiades and Praesepe, where G dwarfs rotate more rapidly than K and early M dwarfs (e.g.,  $P_{\text{rot}}$  ranges between 6.7 and 18.6 days in Praesepe over the same  $T_{\text{eff}}$  range).

However, it is reminiscent of the NGC 6811 sequence derived by Meibom et al. (2011a); the key difference is that the 2.7 Gyr flat sequence extends at least down to  $0.55 M_\odot$ , whereas Curtis et al. (2019a) demonstrated that at  $M_* \lesssim 0.8 M_\odot$  the NGC 6811 sequence begins to curve upward toward longer periods as it merges seamlessly with the younger Praesepe sequence.

This extension of the flat sequence to lower masses is a consequence of the mass dependence of the duration of the epoch of stalled braking. While the higher-mass stars spin more rapidly than lower-mass stars at the age of Praesepe, they resume spinning down earlier and so are able to catch up to the K dwarfs just as these resume spinning down. The process tends to flatten out the color-period sequence.

While its appearance is flat compared to the steep younger sequences, the Ruprecht 147 sequence does seem to be subtly

curved. The sequence appears to dip downward from  $\approx 23.7$  days at spectral type K2 ( $(G_{\text{BP}} - G_{\text{RP}})_0 \approx 1.09, 0.85 M_{\odot}$ ) to slightly faster periods of  $\approx 19.9$  days at K7 ( $(G_{\text{BP}} - G_{\text{RP}})_0 \approx 1.75, 0.62 M_{\odot}$ ) and then curves back up to  $\approx 21.9$  days at M1 ( $(G_{\text{BP}} - G_{\text{RP}})_0 \approx 2.05, 0.55 M_{\odot}$ ). However, this ‘‘sagging’’ curvature is only supported by five stars with  $P_{\text{rot}} < 21$  days.

Recently, Angus et al. (2020) analyzed the McQuillan et al. (2014) sample of  $\sim 34,000$  main-sequence dwarfs in the Kepler field with measured rotation periods, combined with Gaia data. The color–period distributions for these field stars were binned and then color-coded according to  $v_b$  velocity dispersion.<sup>34</sup> Lines of constant velocity dispersion emerged, tracing out gyrochrones across the diagram. At young ages (i.e., low velocity dispersion), these gyrochrones increase from warm and rapid to cool and slow, similar to the pattern seen in young clusters like Praesepe. However, the relationship between color and period flattens out at intermediate ages, similar to what we have found for Ruprecht 147. At older ages, the relation inverts, where cooler stars spin more rapidly than their warmer coeval counterparts. This result presents an independent verification of the flattening of middle-aged rotation sequences.

#### 6.4. When Do Stalled Stars Resume Spinning Down?

With our new  $P_{\text{rot}}$  measurements for Ruprecht 147, it is now clear that stalling is a temporary evolutionary stage. As expected based on the distribution of  $P_{\text{rot}}$  measured for low-mass field stars, such as those in the Kepler field in the top right panel of Figure 7, low-mass stars do indeed eventually resume spinning down.

With our new data, we can empirically determine the age at which stars resume spinning down, if we make a few simplifying assumptions:

1. The lower envelope of the Kepler  $P_{\text{rot}}$  distribution represents the  $P_{\text{rot}}$  at which initially rapidly rotating stars converge to join the slow sequence. This process proceeds from higher to lower masses, which explains why the Pleiades slow sequence is only converged down to  $M_{\star} \approx 0.75 M_{\odot}$ , whereas the Praesepe slow sequence extends down to near the fully convective boundary at  $M_{\star} \approx 0.4 M_{\odot}$ . For more details, see Appendix A.4.
2. Stars completely stall after converging on the slow sequence (i.e.,  $n = 0$ ).
3. Once stars resume spinning down, they follow a Skumanich-like law with  $P_{\text{rot}} \propto t^n$ , where  $n = 0.62$ , irrespective of stellar mass. We examine the post-stalling braking index in Appendix G.

To calculate the age at which stars resume spinning down,  $t_{\text{R}}$ , we fit the ratio of the lower envelope to the joint 2.7 Gyr sequence, raised to the  $1/n$  power where  $n = 0.62$ , and scaled by the 2.7 Gyr age of Ruprecht 147. In other words, we calculate how long it takes to ‘‘rewind’’ the 2.7 Gyr sample back to the  $P_{\text{rot}}$  convergence line, represented by the lower envelope of the Kepler distribution. The bottom panels of Figure 8 plot the resulting  $t_{\text{R}}$  in logarithmic and linear scales, which show a power-law relationship with stellar mass. We fit

this relationship with the function

$$t_{\text{R}} = t_{\text{R},\odot} (M_{\star}/M_{\odot})^{\alpha} \quad (1)$$

and find  $t_{\text{R},\odot} = 231 \pm 10$  Myr and  $\alpha = -3.65 \pm 0.20$ .<sup>35,36,37</sup> The scatter about this fit in Figure 8 is clearly low, indicating that the statistical uncertainty is negligible. However, the true uncertainty is difficult to estimate because it is determined by the validity of our assumptions, not the quality or quantity of data at hand. We require  $P_{\text{rot}}$  sequences for other intermediate-age clusters to constrain the post-stalling braking index, and we need  $P_{\text{rot}}$  distributions for younger clusters to determine when stars converge on the slow sequence as a function of mass.

This formula has a strong mass dependence, where, for example, an  $M_{\star} = 0.55 M_{\odot}$  star will not resume spinning down until it is 2.0 Gyr old ( $T_{\text{eff}} \approx 3700$  K,  $(G_{\text{BP}} - G_{\text{RP}})_0 \approx 2.1$ , M1V). Since analogous stars appear to be converged on the slow sequence by 670 Myr, the age of Praesepe, these stars apparently are stalled for  $\geq 1.3$  Gyr.

In this paper so far, we have advanced gyrochronology by illustrating two things: (1) stalled stars do in fact resume spinning down. That they do is already made obvious by the existence of slower stars in the Kepler field, as pointed out in our study of NGC 6811 (Curtis et al. 2019a), but it is encouraging to see this in an older cluster, and (2) cluster color–period gyrochrone sequences flatten out over time. However, we are not yet attempting to repair gyrochronology. There is still far too much work ahead of us, and it is premature to recalibrate or reformulate a rotation–age relationship until we have filled in other critical gaps in time and mass with light-curve data already available. The stalling timescale is not meant to be used for any reason other than to illustrate the magnitude of the problem. Until we can empirically determine the post-stalling braking index and any dependence on mass, age, or metallicity, this resume time is fundamentally limited by our assumed braking index and the idea behind using the lower envelope of the Kepler field as a reference point for where stars stall.

#### 6.5. Why Do Stars Temporarily Stall? Evaluating the Core–Envelope Coupling Model

A purely empirical, data-driven model for spin-down (i.e., a gyrochronology relation) can be agnostic to the underlying physical causes for angular momentum evolution and still yield accurate and precise ages. In contrast, semi-physical models rely on prescriptions for the magnetic braking torque, which scales with various physical stellar properties and includes some parameters that are empirically tuned (e.g., with cluster and solar data). One approach assumes that stars rotate as solid bodies (e.g., van Saders & Pinsonneault 2013; Matt et al. 2015). In this case, one way to account for a short-term stalling epoch might be to temporarily reduce the magnetic braking efficiency.

Another class of semi-physical model describes the stellar interior with a two-zone approximation, where the convective

<sup>34</sup> At the Kepler field’s low galactic latitude, the velocity in the direction of galactic latitude,  $v_b$ , approximates the vertical velocity perpendicular to the plane,  $v_z$  (often denoted  $W$ ). The dispersion of  $v_z$  increases with age for a population of stars via dynamical heating. Therefore, the dispersion of  $v_b$  for similarly aged stars in the Kepler field should likewise increase with age.

<sup>35</sup> This approach was inspired by the Spada & Lanzafame (2020) calculation of the core–envelope timescale.

<sup>36</sup> The uncertainties are estimated by the bootstrap method, where Gaussian errors of  $0.02 M_{\odot}$  for mass and 10% for  $P_{\text{rot}}$  are applied to simulated cluster samples.

<sup>37</sup> Fitting the resume time as a function of  $T_{\text{eff}}$  and  $(G_{\text{BP}} - G_{\text{RP}})_0$ , we find  $t_{\text{R}} = 202 (T_{\text{eff}}/5770 \text{ K})^{-5.11}$  and  $t_{\text{R}} = 328 ((G_{\text{BP}} - G_{\text{RP}})_0)^{2.47}$  in Myr.



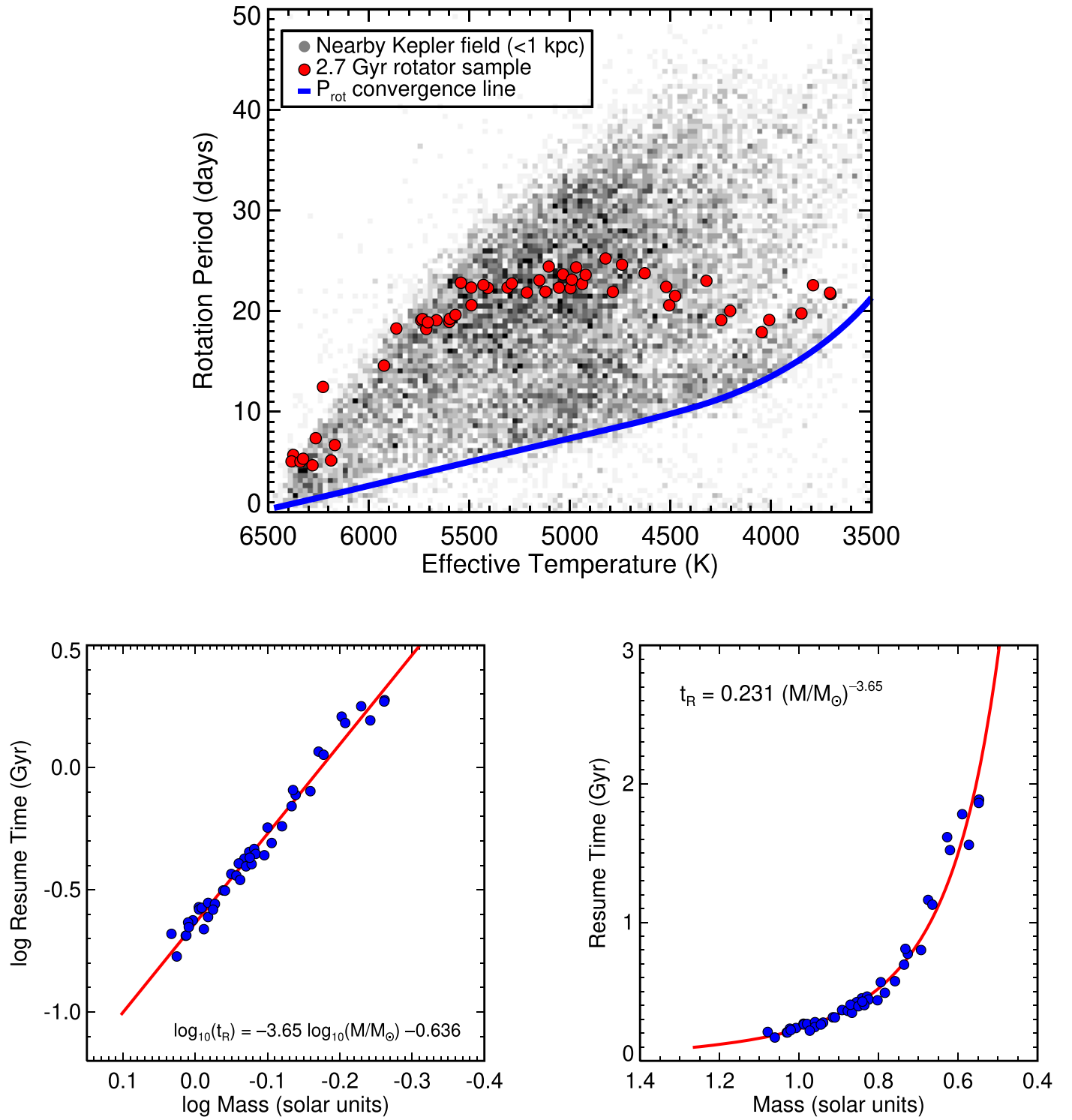


**Figure 8.** When do stalled stars resume spinning down? Top: Kepler  $P_{\text{rot}}$  distribution (McQuillan et al. 2014) has a border along the lower envelope, which we posit represents the rotation period at which stars converge onto the slow sequence (following Figure 7, temperatures are computed from Gaia DR2 colors using our color-temperature relation presented in Appendix A.1, after dereddening with our  $E(B - V) = 0.04 \text{ mag kpc}^{-1}$  relation derived in Appendix F; data are similarly binned by 25 K and 0.5 days). We fit a representation of this border with a sixth-order polynomial (blue line). The representation was created by combining a fit to the Pleiades sequence for more massive stars ( $M_* > 0.95 M_{\odot}$ , modeled with a line of constant Rossby number, where  $R_o = 0.29$  using the Cranmer & Saar 2011 convective turnover timescale), a polynomial fit to the Praesepe sequence for lower-mass stars ( $M_* < 0.59 M_{\odot}$ ), and points marked by hand for the intervening range. Bottom: age at which stars resume spinning down vs. stellar mass ( $M_{\odot}$ ), plotted in logarithmic (left) and linear (right) scales. The blue points are the individual measurements of the resume time,  $t_R$  (Equation (1)), calculated by dividing the convergence line formula by the  $P_{\text{rot}}$  data for the joint 2.7 Gyr sample (NGC 6819 + Ruprecht 147) raised to the  $1/n$  power and then scaled by the 2.7 Gyr age for the old-age reference sample (i.e., the gyrochronal age for the convergence line, which itself is not a gyrochrone). Here we adopted  $n = 0.62$  (Douglas et al. 2019).

envelope is allowed to rotate at a different rate than the core. In these models, angular momentum is assumed to be exchanged between the envelope and core on some characteristic timescale (MacGregor & Brenner 1991). According to this scenario, when the age of the star is comparable to this core–envelope coupling timescale, the rotational braking of the envelope (which includes the visible surface) is temporarily stalled because the spin-down torque from the stellar wind is counteracted by a spin-up torque from the core. This does not necessarily cause stars to fully stall. We assumed  $n = 0$  to estimate the resume time; however, core–envelope coupling can result in a reduced but nonzero  $n$ , where the angular momentum received from the interior is not perfectly balanced against that lost via magnetic braking.

Unfortunately, the timescale for this coupling has not been modeled purely from theory and instead requires empirical constraints from open clusters, which until now have not reached to low enough masses at old enough ages. For this reason, prior core–envelope models failed to predict the full impact of this phenomenon (e.g., Gallet & Bouvier 2013, 2015; Lanzafame & Spada 2015).

Spada & Lanzafame (2020) recently recalibrated their model using our new  $P_{\text{rot}}$  data for NGC 6811 (Curtis et al. 2019a) and reported that their model can now account for most of the apparent stalling effect seen between Praesepe and NGC 6811. In the appendix of their paper, these authors tabulated rotational isochrones, and we can now test how well they perform.

The bottom right panel of Figure 7 shows our benchmark sample along with the Spada & Lanzafame (2020) models. According to their model, the strong mass dependence of the core–envelope coupling timescale introduces a change in slope from steep to flat in the color–period diagram. With respect to the Ruprecht 147 sequence, this model is clearly superior to the Praesepe projection model (bottom left panel of the same figure). It also performs better for the NGC 752 stars and the old, nearby K dwarfs.

The Spada & Lanzafame (2020) model does appear to mildly overshoot the mid-K dwarfs in NGC 752 (by 1.6 days) and Ruprecht 147 (by 2.7 days), suggesting that it needs refining with the data for these older clusters. In Figure 9, we calculate gyrochronal ages for the joint sample of benchmark rotators for NGC 6819 and Ruprecht 147 using this Spada & Lanzafame (2020) model,<sup>38</sup> as well as our polynomial fit to the Praesepe sequence projected forward in time using our solar-calibrated  $n = 0.62$  braking index. Both models work fine at this age for  $M_* > 0.8 M_\odot$  stars; however, each underestimates the true 2.7 Gyr age for  $M_* < 0.7 M_\odot$  stars ( $T_{\text{eff}} \lesssim 4350$  K,  $(G_{\text{BP}} - G_{\text{RP}})_0 > 1.46$ ,  $>K5V$ ), and we find median ages of 2.2 and 1.1 Gyr from each model, respectively. In other words, the large 60% age bias that comes from ignoring stalling is significantly reduced to only 20% with the empirically tuned core–envelope coupling model.

The Spada & Lanzafame (2020) model does not predict full stalling ( $n = 0$ ) behavior, which would appear as truly horizontal lines in Figure 4 of their paper. But Curtis et al. (2019a) found that the Praesepe and NGC 6811 sequences

<sup>38</sup> We used the 2.5 Gyr model tabulated in Spada & Lanzafame (2020) as a function of stellar mass and interpolated it for each star in the sample using masses estimated using the Kraus & Hillenbrand (2007)  $T_{\text{eff}}-M_*$  table together with our relation for converting Gaia DR2  $(G_{\text{BP}} - G_{\text{RP}})_0$  to  $T_{\text{eff}}$ . We then applied our  $n = 0.62$  braking index to calculate ages:  $t = (\text{observed } P_{\text{rot}} / \text{model } P_{\text{rot}})^{1/n} \times 2.5$  Gyr.

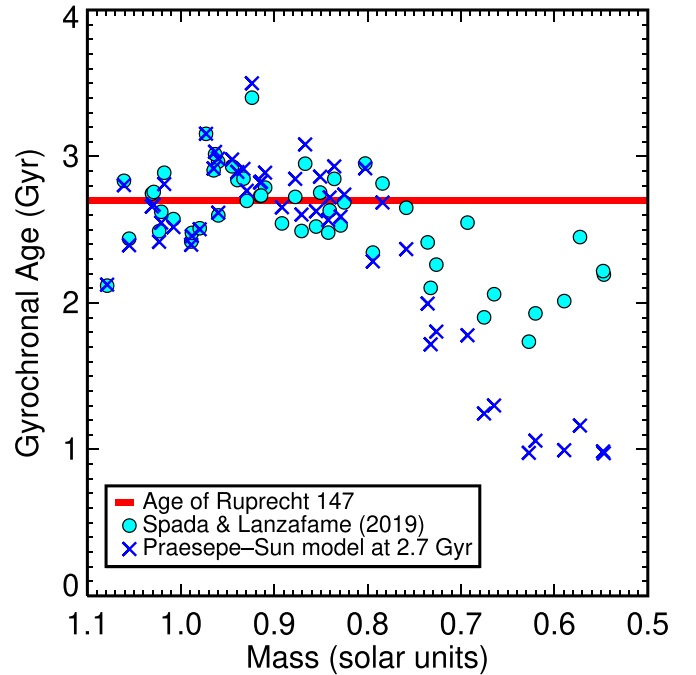


**Figure 9.** Gyrochronal ages vs. stellar mass for benchmark stars in Ruprecht 147 and NGC 6819 calculated using two models. The cyan points show ages calculated with the Spada & Lanzafame (2020) core–envelope coupling model, which was empirically tuned with data from the Pleiades, Praesepe, and NGC 6811 clusters. The blue crosses show ages calculated with the Praesepe polynomial model projected forward in time from 670 Myr to 2.7 Gyr using the  $n = 0.62$  braking law. The red line shows the 2.7 Gyr age of Ruprecht 147. Stars with  $M_* < 0.7 M_\odot$  show the largest discrepancy with both models, with median gyrochronal ages of 1.1 and 2.2 Gyr for the Praesepe and Spada & Lanzafame (2020) models, respectively. The Spada & Lanzafame (2020) model significantly reduces the relative error from 60% down to 20%. As the core–envelope coupling timescale for this model is empirically tuned, incorporating data for NGC 752 and Ruprecht 147 into the calibration might improve this further.

precisely overlapped. To further constrain the exact  $n$  during and after stalling, an expanded rotator sample for other immediate-aged clusters is needed, along with precise knowledge of the interstellar reddening toward each cluster and an understanding of the impact of metallicity on spin-down (Amard & Matt 2020).

#### 6.6. Recommendation for Age-dating Old K Dwarfs: The Case of 36 Ophiuchi

We believe that it is premature to offer a full recalibration of gyrochronology at this stage. First, we have additional clusters ready to analyze. Furthermore, it has only recently become possible to incorporate en masse the large sample of field stars with measured rotation periods into a calibration through the application of kinematic age-dating (Angus et al. 2020). Finally, wide binaries offer great potential for studying stalling, expanding the parameter space covered by the benchmark sample to lower masses and older ages, and testing the impact of metallicity on spin-down; however, this potential has not yet been realized, as there are only a handful of well-characterized systems (e.g.,  $\alpha$  Cen, 61 Cyg) and only a few preliminary investigations published using Kepler targets (Janes 2017, 2018).

Apart from the Spada & Lanzafame (2020) model, how should one approach age-dating old K dwarfs according to their observed rotation? If we apply the original tenet of

gyrochronology, that stars spin down continuously with a constant braking index common to all stars, then all we need is a rotation period sequence for one cluster (to delineate the mass dependence) and a braking index. Out of necessity, to calculate the resume time we posited that this assumption is valid once spin-down resumes. If true, one could then use the Ruprecht 147 color–period sequence in combination with our solar-calibrated braking index ( $n = 0.62$ ).

To illustrate this concept, let us consider the case of the triple-star system, 36 Ophiuchi, which is composed of an inner binary of early K dwarfs (A+B) and a wider mid-K dwarf companion (C). Their properties are summarized in Table 3. The three stars have rotation periods measured by the Mount Wilson Survey (Baliunas et al. 1983; Donahue et al. 1996), and the values are quite similar: 20.69, 21.11, and 18.0 days. According to classic gyrochronology relations and theoretical predictions, 36 Oph C should be rotating more slowly than A or B.

Stated differently, Barnes (2007) found gyrochronal ages for A and B of 1.43 Gyr, but C was only  $590 \pm 70$  Myr old. Later, Mamajek & Hillenbrand (2008) ignored the C component and calculated 1.9 Gyr for A and B; however, that model also yields an age for C that is half the value for A and B, i.e., the Mamajek & Hillenbrand (2008) model predicts  $P_{\text{rot}} = 25.4$  days for C, which is 40% slower than its observed value. The Barnes (2010) model similarly yields 2.1 Gyr for A and B and 1.3 Gyr for C. Now that we have a well-defined sequence for Praesepe, we can use its model and our solar-calibrated braking index to age-date this trio, and we find 2.36, 2.45, and 1.30 Gyr. While our absolute values are systematically older (analogous stars in Praesepe spin at 9.48, 9.45, and 11.91 days, so 36 Oph must be significantly older than that cluster), this model still finds C to be half the age of A and B. Barnes (2007) explained that A and B share a highly eccentric orbit; although their orbital period is quite long ( $\sim 500$  yr), their periastron is estimated to be only  $\sim 6$  au. Barnes (2007) speculated that gravitational tides had altered the rotational evolution for A and B, leaving C to reveal the true age of the system.

However, we can now offer an alternative interpretation in light of the mass-dependent stalling phenomenon. While we expect that each star was temporarily stalled in the past, A and B should have resumed spinning down before C, allowing them to “catch up” and even surpass C in rotational period. Instead of projecting the Praesepe model forward in time, if we rewind the Ruprecht 147 model backward using the same  $n = 0.62$  time dependence, we find ages of 2.24, 2.31, and 2.14 Gyr.<sup>39</sup> In other words, one no longer needs to invoke tides to explain the rotation periods for this trio.

We expect that  $P_{\text{rot}}$  will eventually be measured for other middle-aged wide binaries, which will corroborate our interpretation of the  $P_{\text{rot}}$  data for 36 Oph and 61 Cyg. Once we have such data, we can test our critical assumption for the post-stalling braking index, and then we will be better positioned to reformulate an empirical gyrochronology relation and constrain theoretical models. In the meantime, for K dwarfs with rotation periods slower than the stalled sequence (the

<sup>39</sup> We also estimated ages using the Spada & Lanzafame (2020) model and found 2.24, 2.31, and 1.78 Gyr. To do this, we calculated a mass-dependent braking index using the 2.0 and 2.5 Gyr models and then applied that to the 2.0 Gyr model tabulated according to  $(B - V)$ . The age of C is only 22% lower than the average of A and B, which is a remarkable improvement over classic models. Even better, our approach using the Ruprecht 147 sequence finds that C is only 6% younger than A and B.

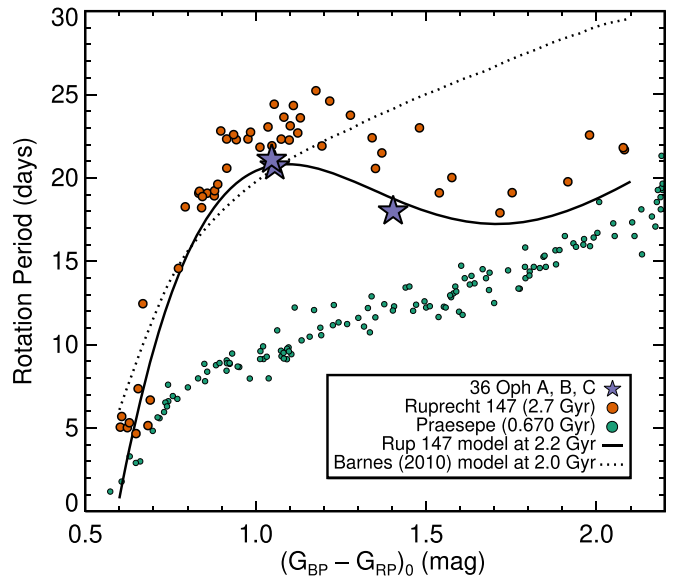


**Figure 10.** Age-dating the triple-star system 36 Ophiuchi. The purple five-point star symbols mark 36 Oph B, A, and C ordered from blue to red in  $(G_{\text{BP}} - G_{\text{RP}})_0$ ; see Table 3 for details. Classic gyrochronology relations yield ages for C that are half the value of A and B, e.g., 590 Myr vs. 1.43 Myr from Barnes (2007), 1.3 Gyr vs. 2.4 Gyr with our Praesepe-based model, or 1.25 Gyr vs. 2.05 Gyr from Barnes (2010) shown as a dotted line in this figure. Instead, for stars that have resumed spinning down (i.e., slower than the Praesepe sequence, shown with green points), we suggest an alternative approach: adopt the Ruprecht 147 color–period sequence as an empirical 2.7 Gyr gyrochrone (orange points), and project it forward or backward in time using a  $t^n$  braking law (for now, we prefer  $n = 0.62$ ). The 36 Oph periods almost overlap the Ruprecht 147 data, indicating that they share a similar age. Spinning them down to best match the Ruprecht 147 sequence yields  $t = 2.2 \pm 0.1$  Gyr for 36 Oph. Gyrochronology can now finally yield a consistent age for the triple system.

overlapping portions of Praesepe and NGC 6811), we hypothesize that such stars have resumed spinning down and can be similarly age-dated relative to the Ruprecht 147 sequence. Our procedure is illustrated in Figure 10.

### 6.7. The Kepler Intermediate-period Gap Is Not Caused by a Lull in Star Formation

Measurements of stellar rotation in the Kepler field revealed a bimodal distribution among cool dwarfs ( $T_{\text{eff}} < 5000$  K) at intermediate periods (15–25 days; McQuillan et al. 2013, 2014). Several hypotheses have been advanced to explain this feature, including a lull in the local star formation rate (McQuillan et al. 2013, 2014). Davenport (2017) argued that this occurred  $\approx 600$  Myr ago, based on the fact that a gyrochrone from Meibom et al. (2009b) appears to trace the gap (see also Davenport & Covey 2018). However, there are two problems with this scenario:

1. The intermediate-period gap does not trace a 600 Myr old population.
2.  $P_{\text{rot}}$  sequences for older clusters cross the gap.

Praesepe provides an *empirical* gyrochrone at 670 Myr (Douglas et al. 2017; Rebull et al. 2017), and it does not trace the gap, but instead follows the lower envelope of the Kepler  $P_{\text{rot}}$  distribution. Sequences for the Hyades (730 Myr; Douglas et al. 2019, 2016) and even NGC 6811 (1 Gyr; Meibom et al. 2011a; Curtis et al. 2019a) likewise do not trace the gap and similarly track the lower envelope of the Kepler  $P_{\text{rot}}$  distribution

at  $T_{\text{eff}} < 4500$  K as they remain stalled. Clearly, the Meibom et al. (2009a) gyrochrone, and indeed all empirical gyrochrones as we have discussed here and elsewhere (Agüeros et al. 2018; Curtis et al. 2019a; Douglas et al. 2019), fail to accurately describe stellar spin-down for cool dwarfs. That the intermediate-period gap approximately coincides with that model is a coincidence.

According to the open cluster data, the intermediate-period gap does not have one common age. In fact, the  $P_{\text{rot}}$  sequences for NGC 752 (1.4 Gyr) and Ruprecht 147 (2.7 Gyr) intersect the gap.<sup>40</sup> This disproves any scenario for the creation of the gap occurring at a single point in time. Indeed, these cluster sequences cross the gap at different points in the diagram, at decreasing masses with increasing ages, indicating that it is formed at different times for stars of different masses.<sup>41</sup>

Alternatively, Reinhold et al. (2019) cited the gap as evidence for a transition from spot- to faculae-dominated photospheres, along with the observation that stars near the gap have weaker photometric amplitudes than slower or faster analogs. In this case, the gap is actually filled with stars; their rotation periods are simply difficult to measure from photometric time series (however, they should be measurable with Ca II H and K monitoring). Reinhold et al. (2019) ascribed a single age of 800 Myr to this transition, irrespective of stellar mass, which the open cluster data clearly refute. However, the idea of a spot-to-faculae transition is not necessarily in conflict with the open cluster data, as long as it is acknowledged that this happens at different times for different masses. We note that the gap also appears to approximately follow a line of constant Rossby number of  $Ro \approx 0.5$  using the Cranmer & Saar (2011) formula for the convective turnover time. This might suggest that the gap is caused by an event in the evolution of the magnetic dynamo, not an event in time, as the magnetic activities of stars of different masses evolve at different rates according to their mass-dependent convective turnover times.

Finally, having found that stars do not spin down continuously, we encourage theoretical work on the possibility that the gap is created by a temporary increase in the braking efficiency, causing stars to “jump” across the gap (an idea originally proposed by McQuillan et al. 2013). In this case, the gap is actually relatively empty (i.e., there are few stars rotating with  $P_{\text{rot}}$  that place them in the gap, irrespective of our ability to measure them). Regarding this idea, we would like to call attention to the five Ruprecht 147 stars in or just beneath the gap (i.e., more rapid and cooler/redder)—they appear to trace the lower edge of the gap, as if they are “waiting in line” to cross it (see Figures 8 and 19).

## 7. Conclusions

We used the 2.7 Gyr old Ruprecht 147 open cluster as a benchmark for studying stellar rotation, with the eventual goal of repairing gyrochronology for low-mass stars. First,

we assembled a catalog of 440 candidate members and identified binaries and nonmembers using astrometric and photometric data from Gaia DR2, RV time series, and high spatial resolution imaging obtained with Robo-AO. Next, we measured periodicities in K2 light curves for 68 stars and then used the chromospheric emission index  $\log R'_{\text{HK}}$  to invalidate  $P_{\text{rot}}$  for three stars. Separately, we used PTF to construct sparser light curves with lower precision for K and early M dwarfs, and we measured  $P_{\text{rot}}$  for seven stars, including three for which we also have measured  $P_{\text{rot}}$  from K2. In these cases, we found nearly identical  $P_{\text{rot}}$  values, despite the differences in cadence, photometric precision, and times of observation. In all, we measured  $P_{\text{rot}}$  for 58 dwarfs, including 35 stars we classify as benchmark rotators, of which 23 are likely single dwarfs.

We paired our Ruprecht 147 data with  $P_{\text{rot}}$  data for the approximately coeval cluster NGC 6819, which was surveyed during the primary Kepler mission. Before merging the data sets, we derived a relative interstellar reddening and distance modulus for NGC 6819 by comparing the apparent magnitudes of red clump giants in each cluster and found  $A_V = 0.44$  for NGC 6819, after accounting for our  $A_V = 0.30$  value for Ruprecht 147.

Meibom et al. (2015) measured  $P_{\text{rot}}$  for 30 NGC 6819 dwarfs with masses  $M_* \gtrsim 0.85 M_{\odot}$ . Our Ruprecht 147 sample extends this mass limit down to  $M_* \approx 0.55 M_{\odot}$  and includes 20 stars with masses below the NGC 6819 sample limit.

Using the overlapping portions of each sample ( $0.84 < M_* < 0.96 M_{\odot}$ ;  $5000 \text{ K} < T_{\text{eff}} < 5500 \text{ K}$ ), we found that the Ruprecht 147 stars rotate systematically more slowly, although only by 5%. Applying the  $n = 0.62$  braking law (Douglas et al. 2019) and adopting 2.7 Gyr for the age of Ruprecht 147, we calculate a gyrochronological age of 2.5 Gyr for NGC 6819, which is consistent with the literature. Considering the merged  $\approx 2.7$  Gyr sample, we now have rotation periods for 67 benchmark stars with  $0.55 M_{\odot} < M_* < 1.3 M_{\odot}$ , 54 of which are likely single.

With this merged sample, we can now study how stars spin down from their youth, represented by younger clusters like the Pleiades and Praesepe, up to 2.7 Gyr. The Ruprecht 147 rotation period sequence appears remarkably flat, with most stars cooler than  $T_{\text{eff}} < 5700$  K contained to within  $P_{\text{rot}} = 22 \pm 2$  days. This is in sharp contrast with the steep mass dependence seen in the younger clusters, where periods tend to get longer toward decreasing mass.

Now that we have identified a temporary epoch of stalled braking (Agüeros et al. 2018; Curtis et al. 2019a; Douglas et al. 2019), we suggest that this flat sequence is produced by the mass-dependent duration of the epoch of stalled braking. While the higher-mass stars spin more rapidly than lower-mass stars at the age of Praesepe, they resume spinning down earlier and so catch up to their lower-mass siblings just as these resume spinning down.

The rotation period distribution for cool dwarfs observed by Kepler shows a gap at intermediate periods, which has been interpreted as evidence for a lull in the local star formation rate (McQuillan et al. 2013, 2014; Davenport 2017; Davenport & Covey 2018). However, the  $P_{\text{rot}}$  sequences for NGC 752 (1.4 Gyr) and Ruprecht 147 intersect this gap, thereby refuting the idea that this gap has a single age or was formed by any single event in time. Instead, perhaps the gap is created by an event in the evolution of the magnetic dynamo, which proceeds

<sup>40</sup> Figure 19 in Appendix D.7 examines a member of Ruprecht 147, EPIC 219489683, which appears to fall right in the gap.

<sup>41</sup> Reinhold & Hekker (2020) reported  $P_{\text{rot}}$  for stars in the K2 campaign fields, which probe different regions of the local Galaxy than did Kepler, and they still find evidence for a “dearth region,” although it is does not appear as pronounced in their data set. The detection of an intermediate-period gap along a variety of sight lines through the Galaxy would also challenge the variable star formation rate hypothesis.

at different rates for stars of different masses (and convective turnover times).

We also used our new data for Ruprecht 147 to determine when stars resume spinning down as a function of mass, and we find that  $0.55 M_{\odot}$  stars are stalled for  $\approx 1.3$  Gyr. The steep mass dependence also means that this phenomenon might present a big obstacle for age-dating even lower-mass stars with rotation. Unfortunately, we were unable to measure  $P_{\text{rot}}$  for  $\leq 0.55 M_{\odot}$  stars in Ruprecht 147 to test this hypothesis.

Spada & Lanzafame (2020) used our new  $P_{\text{rot}}$  data for NGC 6811 (Curtis et al. 2019a) to recalibrate an angular momentum evolution model that incorporates core–envelope coupling, which these authors claim can explain the stalled braking phenomenon. Indeed, the Spada & Lanzafame (2020) model more closely matches our new Ruprecht 147  $P_{\text{rot}}$  data than any other model we are aware of, including the purely empirical (e.g., Barnes 2003, 2007, 2010; Angus et al. 2019) or the semi-physical varieties (e.g., van Saders & Pinsonneault 2013; Gallet & Bouvier 2015; Matt et al. 2015). There is still some tension with the data, which perhaps can be mitigated by incorporating these measurements into their calibration. In that case, however, we would require  $P_{\text{rot}}$  data for other old stars to validate a retuned model. In the interim, to age-date old K dwarfs, we recommend using the Ruprecht 147  $P_{\text{rot}}$  sequence as an empirical 2.7 Gyr gyrochrone and projecting it in time using a  $t^n$  ( $n = 0.62$ ) braking law.

Finally, to derive empirically *how long* stars are stalled, we need to know when stars converge on the slow sequence as a function of mass. The difference in age between the Pleiades and Praesepe is too large to work this out from the  $P_{\text{rot}}$  data for these two clusters alone, however. There has been progress in filling in the age gap with other clusters using ground-based data, for example, M34 (200–250 Myr; Meibom et al. 2011b), M48 (400–450 Myr; Barnes et al. 2015), and M37 (550 Myr; Hartman et al. 2009). The situation will hopefully improve in the near future from additional ground-based surveys of young clusters and from the high-cadence photometric imaging from NASA’s Transiting Exoplanet Survey Satellite (Ricker et al. 2015).

J.L.C. is supported by the National Science Foundation Astronomy and Astrophysics Postdoctoral Fellowship under award AST-1602662 and the National Aeronautics and Space Administration under grant NNX16AE64G issued through the K2 Guest Observer Program (GO 7035). M.A.A. acknowledges support provided by the NSF through grant AST-1255419. S.T.D. acknowledges support provided by the NSF through grant AST-1701468. S.P.M. is supported by the European Research Council under the European Union’s Horizon 2020 research and innovation program (agreement No. 682393, AWESoMeStars). S.H.S. acknowledges support by NASA Heliophysics LWS grant NNX16AB79G. C.Z. is supported by a Dunlap Fellowship at the Dunlap Institute for Astronomy & Astrophysics, funded through an endowment established by the Dunlap family and the University of Toronto. Funding for the Stellar Astrophysics Centre is provided by The Danish National Research Foundation (grant agreement No. DNR106). The Center for Exoplanets and Habitable Worlds and the Penn State Extraterrestrial Intelligence Center are supported by the Pennsylvania State University and the Eberly College of Science.

We thank Sydney Barnes, Mark Giampapa, Jennifer van Saders, Travis Metcalfe, Eric Mamajek, Garrett Somers, Federico Spada, David Gruner, Rayna Rampalli, and the attendees of the Thinkshop 16 meeting hosted at the Leibniz Institute for Astrophysics in Potsdam, Germany (AIP) in 2019,<sup>42</sup> for enlightening conversations on rotation, activity, and our Ruprecht 147 results. We acknowledge preliminary work on the PTF data by Leo J. Liu (not used in this study). We are grateful to the K2 Guest Observer office and Ball Aerospace for repositioning the Campaign 7 field to accommodate Ruprecht 147; the staff at the various observatories cited in this study; the Harvard–Smithsonian Center for Astrophysics telescope allocation committee for granting access to Magellan and TRES; Iván Ramírez for assistance acquiring and analyzing MIKE spectra; John O’Meara and John Bochanski for assistance with MagE; Edward Villanueva and Dan Kelson for their assistance with MIKE data; Jeff Valenti, Debra Fischer, and John M. Brewer for assistance with SME; Katja Poppenhaeger for supporting our petition to repoint K2 Campaign 7, Fabienne Bastien for supporting our GO 7035 proposal, and Jennifer van Saders and Florian Gallet for sharing rotational isochrones generated from their angular momentum evolution models (van Saders & Pinsonneault 2013; Gallet & Bouvier 2015).

This paper includes data collected by the Kepler and K2 missions, which are funded by the NASA Science Mission Directorate. We obtained these data from the Mikulski Archive for Space Telescopes (MAST). STScI is operated by the Association of Universities for Research in Astronomy, Inc., under NASA contract NAS5-26555. Support for MAST for non-HST data is provided by the NASA Office of Space Science via grant NNX09AF08G and by other grants and contracts.

This work has made use of data from the European Space Agency (ESA) mission Gaia,<sup>43</sup> processed by the Gaia Data Processing and Analysis Consortium (DPAC).<sup>44</sup> Funding for the DPAC has been provided by national institutions, in particular the institutions participating in the Gaia Multilateral Agreement.

This work made use of the <https://gaia-kepler.fun> cross-match database, created by Megan Bedell.

This paper is based on observations obtained with the Samuel Oschin Telescope as part of the Palomar Transient Factory project, a scientific collaboration between the California Institute of Technology, Columbia University, Las Cumbres Observatory, the Lawrence Berkeley National Laboratory, the National Energy Research Scientific Computing Center, the University of Oxford, and the Weizmann Institute of Science.

The Robo-AO system was developed by collaborating partner institutions, the California Institute of Technology and the Inter-University Centre for Astronomy and Astrophysics, and with the support of the National Science Foundation under grant Nos. AST-0906060, AST-0960343, and AST-1207891, the Mt. Cuba Astronomical Foundation, and by a gift from Samuel Oschin.

This work utilized SOLIS data obtained by the NSO Integrated Synoptic Program (NISP), managed by the National Solar Observatory, which is operated by the Association of

<sup>42</sup> <https://thinkshop.aip.de/16/cms/>

<sup>43</sup> <https://www.cosmos.esa.int/gaia>

<sup>44</sup> <https://www.cosmos.esa.int/web/gaia/dpac/consortium>

Universities for Research in Astronomy (AURA), Inc., under a cooperative agreement with the National Science Foundation.

This research has made use of NASA’s Astrophysics Data System and the VizieR (Ochsenbein et al. 2000) and SIMBAD (Wenger et al. 2000) databases, operated at CDS, Strasbourg, France.

*Facilities:* Gaia, K2, PTF, PO:1.5 m (Robo-AO).

*Software:* The IDL Astronomy User’s Library (Landsman 1993), K2fov (Mullally et al. 2016).

## Appendix A

### Polynomial Models for Stellar Property Relations and Color–Period Sequences

#### A.1. An Empirical Color–Temperature Relation

The Gaia DR2 catalog included effective temperatures for  $1.61 \times 10^8$  stars with  $G < 17$  mag and  $3000 \text{ K} < T_{\text{eff}} < 10,000 \text{ K}$ , determined from the broadband photometry (Bailer-Jones et al. 2013; Andrae et al. 2018). These  $T_{\text{eff}}$  values can be heavily biased by interstellar reddening, which is unaccounted for in DR2. For example, with  $A_V = 0.3$ , the Gaia DR2  $T_{\text{eff}}$  values for solar-type stars in Ruprecht 147 are negatively biased by 300–400 K. Fortunately, we know the amount of interstellar reddening for this and the other clusters we are studying, so we can deredden the photometry and estimate accurate photometric temperatures with an empirical color–temperature relation of our own construction. Figure 11 shows the empirical color–temperature relation we built from three benchmark samples:

1. Brewer et al. (2016a): This catalog includes stellar properties and abundances calculated from HIRES spectra collected for the California Planet Survey, which were analyzed with SME (Valenti & Piskunov 1996; Valenti & Fischer 2005) following the Brewer et al. (2015) procedure. We selected stars with high-quality spectra ( $S/N > 70$ ) with  $T_{\text{eff}} > 4700 \text{ K}$ , low photometric errors ( $\sigma_{G_{\text{BP}}}, G_{\text{RP}} < 0.05$ ;  $\sigma_G < 0.025$ ), fainter than  $G > 3.7$  mag (to avoid any photometry problems for very bright stars), with  $-0.5 < [\text{Fe}/\text{H}] < +0.5$  dex, and  $d < 200$  pc to minimize the impact of interstellar reddening. This includes 886 stars with  $4702 \text{ K} < T_{\text{eff}} < 6674 \text{ K}$  and  $2.81 \text{ dex} < \log g < 4.83 \text{ dex}$ .
2. Boyajian et al. (2012): This catalog includes 30 stars with  $3054 \text{ K} < T_{\text{eff}} < 5407 \text{ K}$  and  $-0.49 \text{ dex} < [\text{Fe}/\text{H}] < +0.35 \text{ dex}$ , which were characterized with interferometry and spectral energy distribution analysis.
3. Mann et al. (2015): We selected 119 stars from this catalog with  $3056 \text{ K} < T_{\text{eff}} < 4131 \text{ K}$  and  $-0.54 \text{ dex} < [\text{Fe}/\text{H}] < +0.53 \text{ dex}$ , after trimming 50 stars that were not cross-matched properly (since the  $T_{\text{eff}}$  range was adequately sampled by the properly matched stars, we did not need to correct this). These stars were characterized with optical and near-infrared spectroscopy.

The scatter about our color–temperature relation implies a typical  $T_{\text{eff}}$  precision of 50 K. Furthermore, as noted by Rabus et al. (2019), the Gaia temperatures for stars cooler than  $T_{\text{eff}} < 4000 \text{ K}$  are inaccurate. Our relation, as well as the Rabus et al.  $M_G$ – $T_{\text{eff}}$  relation, more accurately represents the cool stars in our sample.

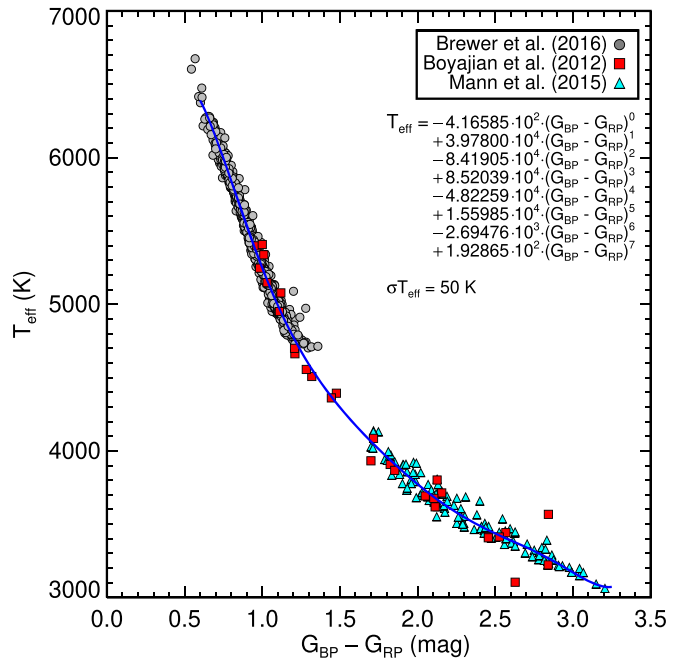


**Figure 11.** Empirical color–temperature relation. This relation is constructed from benchmark stars drawn from Brewer et al. (2016a), Boyajian et al. (2012), and Mann et al. (2015). The scatter about the relationship implies a typical  $T_{\text{eff}}$  precision of 50 K. The formula is provided in Table 4.

#### A.2. The Empirical Hyades Main Sequence

We fit a polynomial to the Gaia DR2 CMD for the Hyades cluster (Gaia Collaboration et al. 2018a), and we often use this as an empirical main sequence for selecting photometrically single stars in the field or in other clusters. For clusters, we typically use a broader cut to reject nondwarf and large outlier stars and then iteratively refit that cluster’s CMD to make a model appropriate for selecting its single dwarfs.

#### A.3. Polynomial Fits to the Converged, Slow Sequences in the Color–Period Distributions for the Pleiades, Praesepe, NGC 6811, NGC 752, and NGC 6819 + Ruprecht 147

We fit polynomials to the dereddened color–period distributions for various open clusters, focusing on the converged portions of their slow sequences. The cluster data are provided in Table 5. These are useful for qualitatively illustrating the empirical basis for gyrochronology and the stalling phenomenon and for comparing field star periods to the benchmark cluster data in a way that is clean and simple, albeit approximate.

Prior to performing these fits, we used Gaia DR2 astrometry, RVs, and CMDs to isolate likely single stars, and we also rejected binaries from the samples based on the identification of multiple rotation periods by the studies from which we collected the  $P_{\text{rot}}$  values. The data for these clusters are provided in the online journal in a table associated with Figure 12. Our strategy for identifying benchmark single-star members for each of these samples is similar to the procedures used in this paper, as well as Douglas et al. (2019) and Curtis et al. (2019a).

Figures 12 and 13 show these distributions in linear and logarithmic space, along with the models and their uncertainties. The coefficients for these models are provided in Table 4. The uncertainties combine  $P_{\text{rot}}$  measurement errors, apparent

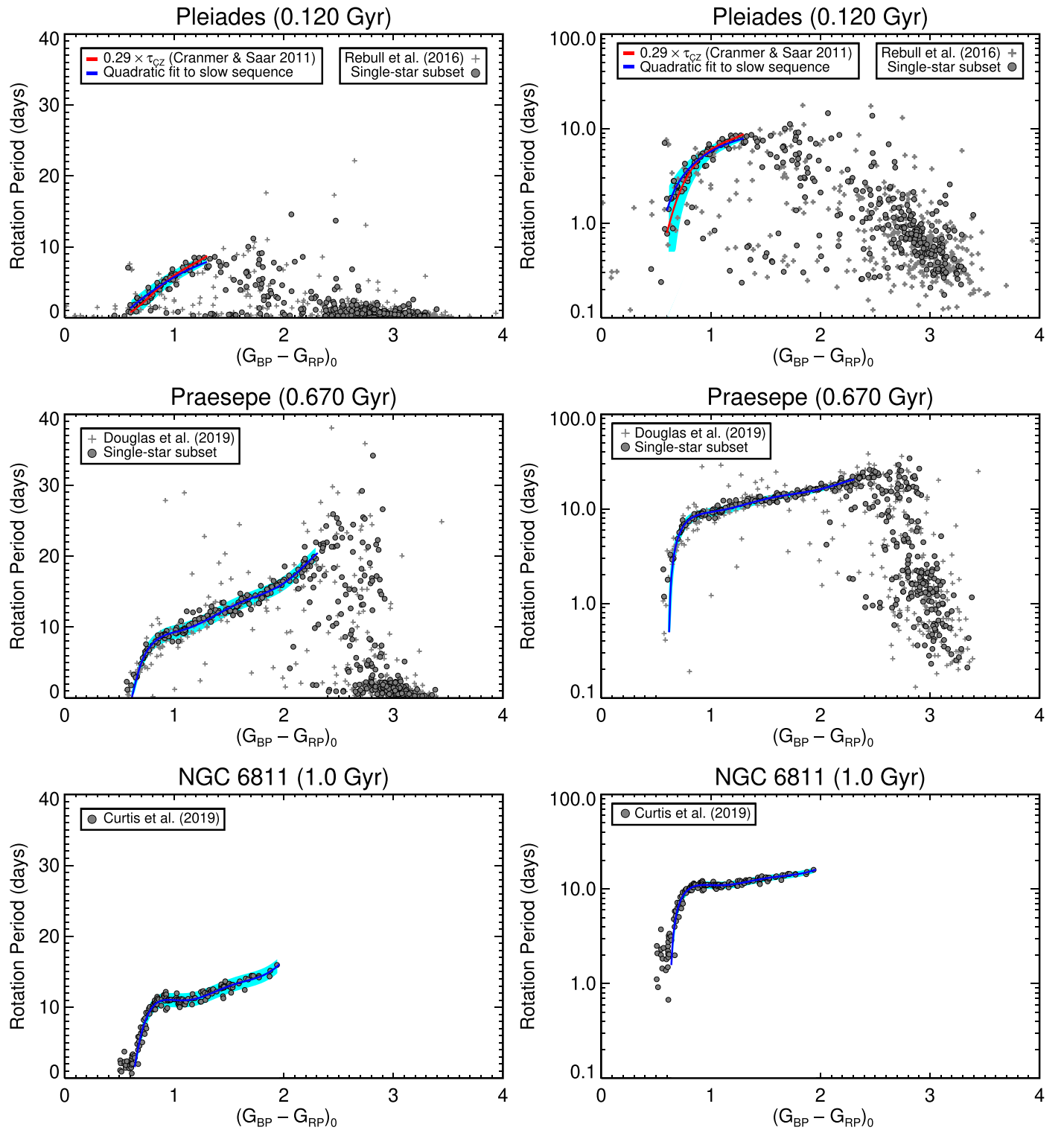


**Figure 12.** Color vs. rotation period for the Pleiades (120 Myr; Rebull et al. 2016), Praesepe (670 Myr; Douglas et al. 2019), and NGC 6811 (1.0 Gyr; Curtis et al. 2019a); NGC 752 (1.4 Gyr; Agüeros et al. 2018) and NGC 6819 (2.5 Gyr; Meibom et al. 2015) with Ruprecht 147 (2.7 Gyr; this work) are shown in Figure 13. Polynomial fits to the slowly rotating sequences are overlaid, and their coefficients are provided in Table 4. The cyan bands show an approximation of the dispersion for each sequence ( $\Delta P_{\text{rot}} = 1$  day applied for Pleiades, Praesepe, and NGC 6811; 2 days applied for NGC 752, NGC 6819, and Ruprecht 147). For younger clusters, the dispersion likely reflects the intrinsic tightness of the sequences, which are still converging. At older ages, the dispersion most likely reflects the  $P_{\text{rot}}$  measurement uncertainties (although differential rotation might also contribute). The cluster data are provided in Table 5.

spread caused by differential rotation, and intrinsic dispersion in the true equatorial rotation periods (i.e., how tightly converged the sequences are). We opted for a single-valued rotation period deviation for each cluster and found

$\Delta P_{\text{rot}} = 1$  day for the Pleiades, Praesepe, and NGC 6811 and 2 days for NGC 752 and the joint sample of NGC 6819 and Ruprecht 147. A synthetic cluster sample can therefore be generated from these models with the application of Gaussian

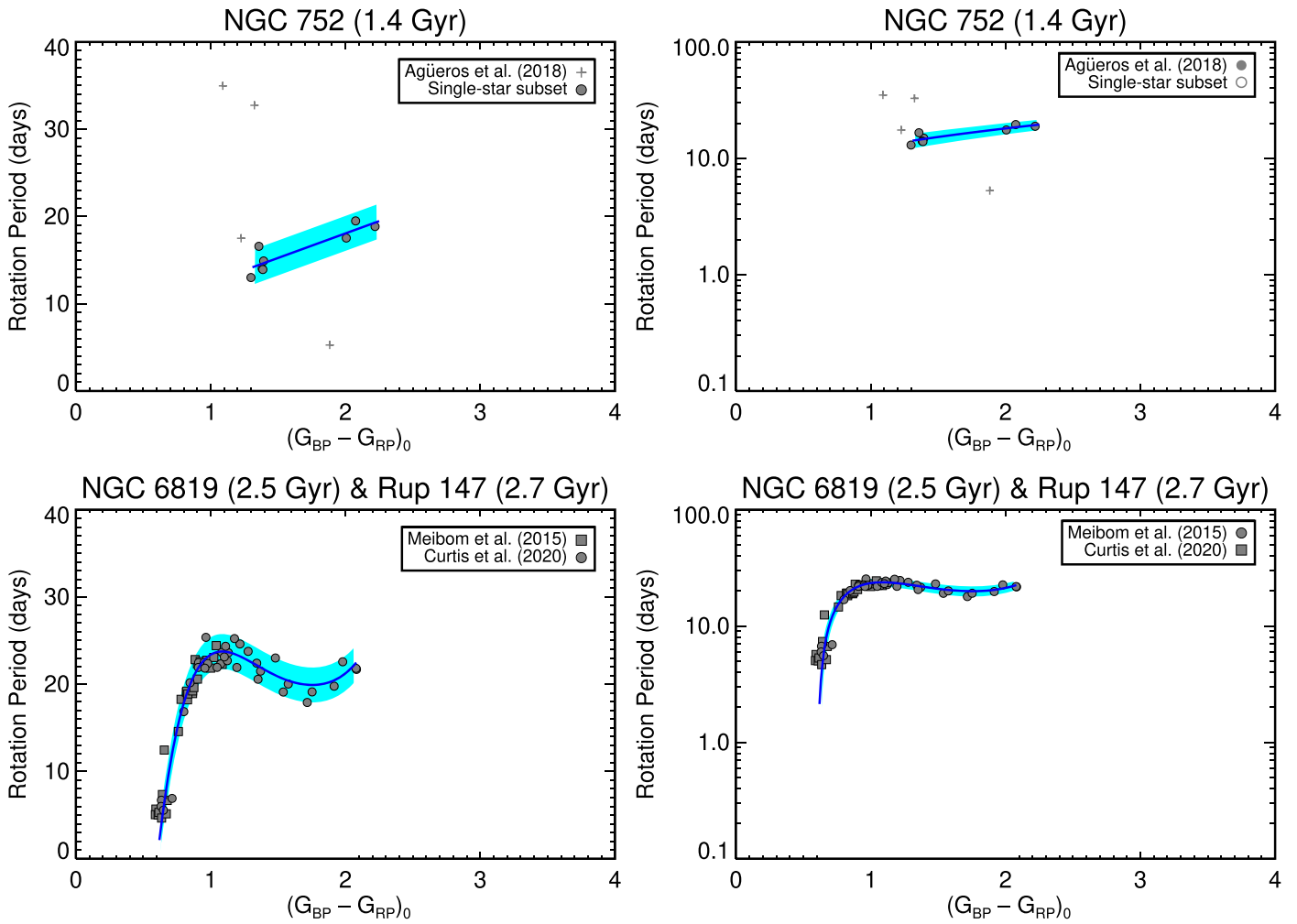


**Figure 13.** Continued from Figure 12—color vs. rotation period for NGC 752 (1.4 Gyr; Agüeros et al. 2018) and NGC 6819 (2.5 Gyr; Meibom et al. 2015) with Ruprecht 147 (2.7 Gyr; this work). Polynomial fits to the slowly rotating sequences are overlaid, and their coefficients are provided in Table 4. The cyan bands show an approximation of the dispersion for each sequence ( $\Delta P_{\text{rot}} = 1$  day applied for Pleiades, Praesepe, and NGC 6811; 2 days applied for NGC 752, NGC 6819, and Ruprecht 147). For younger clusters, the dispersion likely reflects the intrinsic tightness of the sequences, which are still converging. At older ages, the dispersion most likely reflects the  $P_{\text{rot}}$  measurement uncertainties (although differential rotation might also contribute). The cluster data are provided in Table 5.

noise with  $\sigma = \Delta P_{\text{rot}}$ . For the Pleiades, its 1-day uncertainty translates to a larger relative dispersion compared to the more slowly rotating Praesepe and NGC 6811 sequences, and we suspect that this reflects the intrinsic tightness of these intermediate-aged sequences compared to the Pleiades stars, which are still converging. For the older clusters, the 2-day dispersion likely reflects their larger  $P_{\text{rot}}$  uncertainties (their longer rotation periods mean that fewer cycles are captured in each light curve, inflating the uncertainty), although differential rotation might also contribute.

*Pleiades.*—We adopt 120 Myr for the Pleiades, based on its lithium depletion boundary (125–130 Myr by Stauffer et al. 1998 and  $115 \pm 5$  Myr by Dahm 2015) and CMD isochrone ages (110–160 Myr from Gossage et al. 2018 and 115–135 Myr from Cummings & Kalirai 2018). We adopted  $A_V = 0.12$  for the interstellar extinction. As Curtis et al. (2019b) explained, the slow sequence is well fit by a line of constant Rossby number,  $\text{Ro} = 0.29$ , using the Cranmer & Saar (2011) convective turnover time formula and our color- $T_{\text{eff}}$  relation. We also fit a quadratic polynomial to the sequence and provide both models in Table 4.

*Praesepe.*—We adopt an age of 670 Myr and  $A_V = 0.035$  for this cluster (for more information, see Table 1 and

Appendix A in Douglas et al. 2019). The polynomial fit to its single star is taken from Equation (1) in Douglas et al. (2019).

*NGC 6811.*—We used 135 “YY” rotators from Curtis et al. (2019a), which satisfy single-star membership criteria and are on the slow sequence; we adopted an age of 1.0 Gyr and  $A_V = 0.15$  from that same work.

*NGC 752.*—Agüeros et al. (2018) presented  $P_{\text{rot}}$  for 12 members; however, only eight have Gaia DR2 consistent with single-star membership. These rotators are clustered into two groupings in color, so the best we can do is fit a straight line between these clumps. We adopted an age of 1.4 Gyr, based on the 1.34 Gyr value from Agüeros et al. (2018) and 1.45 Gyr value from Twarog et al. (2015), and also applied  $A_V = 0.1$  (Twarog et al. 2015).

*NGC 6819 + Ruprecht 147.*—The fundamental parameters for NGC 6819 and Ruprecht 147 were reviewed in Appendix E and Section 2, respectively. To construct this model, we divided the sequence into blue and red portions, split at  $(G_{\text{BP}} - G_{\text{RP}})_0 = 0.85$ . For the blue portion, we applied the Praesepe model projected forward in time from 670 Myr to 2.7 Gyr using an  $n = 0.62$  braking law. For the red portion, we fit a cubic polynomial to the  $P_{\text{rot}} > 18$  day rotators. We then refit this



**Table 4**  
Polynomial Models for Estimating Stellar Properties and for Describing Cluster Rotation Period Sequences

Property, $Y$	$(G_{\text{BP}} - G_{\text{RP}})_0$	$c_0$	$c_1$	$c_2$	$c_3$	$c_4$	$c_5$	$c_6$	$c_7$
<i>Stellar Properties</i>									
<i>Estimating effective temperature from the dereddened Gaia DR2 color, <math>(G_{\text{BP}} - G_{\text{RP}})_0</math></i>									
$T_{\text{eff}}$ (K)	0.55 to 3.25	-416.585	39780.0	-84190.5	85203.9	-48225.9	15598.5	-2694.76	192.865
<i>The empirical Hyades main sequence: <math>(G_{\text{BP}} - G_{\text{RP}})</math> versus <math>M_G</math></i>									
$M_G$ (mag)	0.2 to 4.2	-0.0319809	4.08935	5.76321	-6.98323	3.06721	-0.589493	0.0417076	...
<i>Color-Period Sequences</i>									
<i>Kepler lower envelope</i>									
$P_{\text{rot}}$ (days)	0.6 to 2.1	36.4756	-202.718	414.752	-395.161	197.800	-50.0287	5.05738	...
<i>Pleiades (120 Myr)—Constant Rossby number, <math>R_o = 0.29</math></i>									
$P_{\text{rot}}$ (days)	0.6 to 1.3	37.068	-188.02	332.32	-235.78	60.395	...	...	...
<i>Pleiades (120 Myr)—quadratic fit</i>									
$P_{\text{rot}}$ (days)	0.6 to 1.3	-8.467	19.64	-5.438	...	...	...	...	...
<i>Praesepe (670 Myr)</i>									
$P_{\text{rot}}$ (days)	0.6 to 2.4	-330.810	1462.48	-2569.35	2347.13	-1171.90	303.620	-31.9227	...
<i>NGC 6811 (1 Gyr)</i>									
$P_{\text{rot}}$ (days)	0.65 to 1.95	-594.019	2671.90	-4791.80	4462.64	-2276.40	603.772	-65.0830	...
<i>NGC 752 (1.4 Gyr)</i>									
$P_{\text{rot}}$ (days)	1.32 to 2.24	6.80	5.63	...	...	...	...	...	...
<i>NGC 6819 + Ruprecht 147 (2.7 Gyr)</i>									
$P_{\text{rot}}$ (days)	0.62 to 2.07	-271.783	932.879	-1148.51	695.539	-210.562	25.8119	...	...

**Note.** Model:  $Y \approx \sum(c_i (G_{\text{BP}} - G_{\text{RP}})_0^i)$ , where  $Y$  is the modeled property. In each case, the degree of the polynomial was selected to minimize systematic patterns in the residuals, except for the NGC 725 relation, which was effectively constrained by two points necessitating a linear model.

two-piece representation with a fifth-order polynomial to produce a smooth relation, provided in Table 4. This polynomial model is valid over the range  $0.75 < (G_{\text{BP}} - G_{\text{RP}})_0 < 2.05$  and  $3700 \text{ K} < T_{\text{eff}} < 6000 \text{ K}$ . We opted for this two-piece approach because we assume that the Praesepe projection model remains valid at this age based on the consistency found for the 1 Gyr old NGC 6811 cluster, despite the lack of benchmark rotators in the  $6000 \text{ K} < T_{\text{eff}} < 6200 \text{ K}$  range in our joint 2.7 Gyr sample.

#### A.4. The Lower Envelope of the Kepler Field $P_{\text{rot}}$ Distribution

In Section 6.4, we posit that the lower envelope of the color-period distribution for Kepler field stars measured by McQuillan et al. (2014) represents the  $P_{\text{rot}}$  at which initially rapidly rotating stars converge on the slow sequence. We then use this model together with the  $P_{\text{rot}}$  data for NGC 6819 and Ruprecht 147 to estimate the age at which stalled stars resume spinning down.

Regarding the stalled  $P_{\text{rot}}$  sequence, we first created a representation of the lower envelope of the Kepler  $P_{\text{rot}}$  distribution, which we then fit with a sixth-order polynomial. For this representation, we used the Pleiades sequence for  $(G_{\text{BP}} - G_{\text{RP}})_0 < 0.93$ , which we modeled with a line of constant Rossby number,  $R_o = 0.29$ , using the  $T_{\text{eff}}$ -based convective turnover time formula from Cranmer & Saar (2011). The density of the Kepler  $P_{\text{rot}}$  distribution drops significantly at  $(G_{\text{BP}} - G_{\text{RP}})_0 > 2.1$  ( $T_{\text{eff}} < 3700 \text{ K}$ ,  $M_* < 0.54 M_{\odot}$ , M1). For these lower-mass stars, we adopt the Praesepe slow sequence, which appears to track the lower

envelope at  $(G_{\text{BP}} - G_{\text{RP}})_0 > 1.9$  ( $M_* < 0.59 M_{\odot}$ ), and which we know is stalled based on our analysis of the NGC 6811 cluster. For the intervening color range,  $0.93 < (G_{\text{BP}} - G_{\text{RP}})_0 < 1.90$ , we marked points by eye, which we added to the representation. The resulting polynomial is shown overlaid on the trimmed Kepler  $P_{\text{rot}}$  distribution in the top panel of Figure 8,<sup>45</sup> and it is provided in Table 4.

## Appendix B Superstamp Light Curves

We provide light-curve data for candidate cluster members located in the Ruprecht 147 superstamp, described in Cody et al. (2018). The light-curve procedure is described in Rebull et al. (2018) and is extracted using 1-, 2-, 3-, and 4-pixel circular moving apertures. Position-dependent detrending was performed with the K2SC code (Aigrain et al. 2016). We also calculated a systematics correction light curve for the 2-pixel apertures, shown in Figure 14, and the 3-pixel apertures. The  $P_{\text{rot}}$  values we measure from the systematics-corrected light curves are not negatively affected by this procedure, i.e., it does not introduce spurious signals, at least none with amplitudes comparable to the stellar rotation signals already prominent in the uncorrected version of the light curves. However, this procedure does yield cleaner plots by removing a strong ramp-up in brightness that appears common to all of our superstamp targets. The superstamp light curves and the systematic correction light curves are available for download from the online journal.

<sup>45</sup> Appendix F describes our procedure for preparing the Kepler  $P_{\text{rot}}$  data from McQuillan et al. (2014) for presentation in this study.

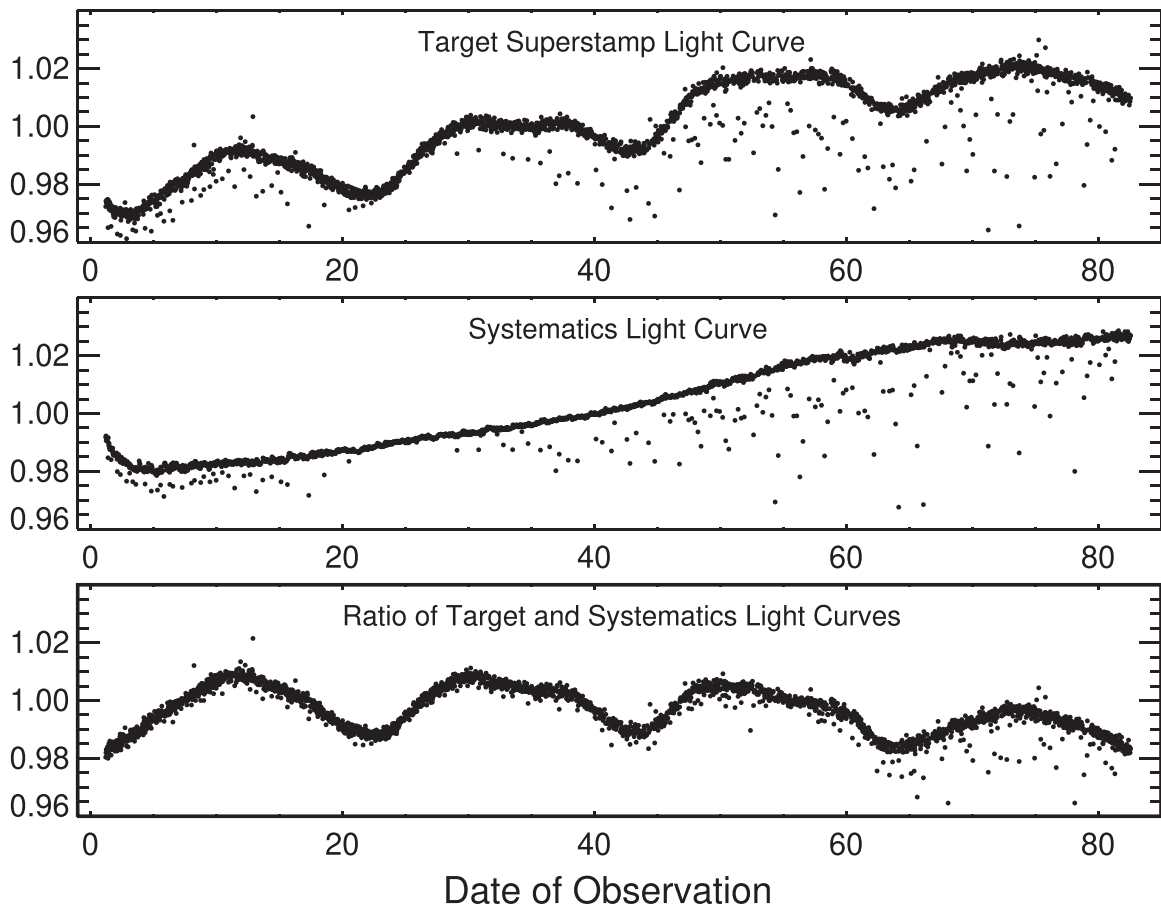


**Figure 14.** Superstamp light-curve preparation for EPIC 219651610, the star featured in Figures 3 and 4. Top: target light curve, extracted from the superstamp with a 2-pixel-radius circular moving aperture. Middle: systematics light curve produced by median-combining the normalized light curves for all superstamp targets in our sample. This shows that the superstamp target light curves share common systematic trends, including a prominent ramp-up in brightness over time. Bottom: the ratio of the target and systematics light curves mostly removes this ramping and other features, isolating the periodic stellar rotation signal. This procedure is largely for improving the aesthetics of our diagnostic plots, as the stellar rotation signal is prominent in the uncorrected version shown in the top panel. The superstamp light curves for individual targets and the systematics correction shown here are available for download in the online journal.

(The data used to create this figure are available.)

### Appendix C

#### Gallery of Selected Variables in the Vicinity of Ruprecht 147 Rotators Observed with PTF

To illustrate the photometric precision of our PTF light curves and our sensitivity to short and long periodicities, we

present a gallery of four reference stars (nonmembers of Ruprecht 147) used in our photometric calibrations. Figure 15 shows the phase-folded light curves for these stars, with periodicities ranging from 5 hr to 50 days.

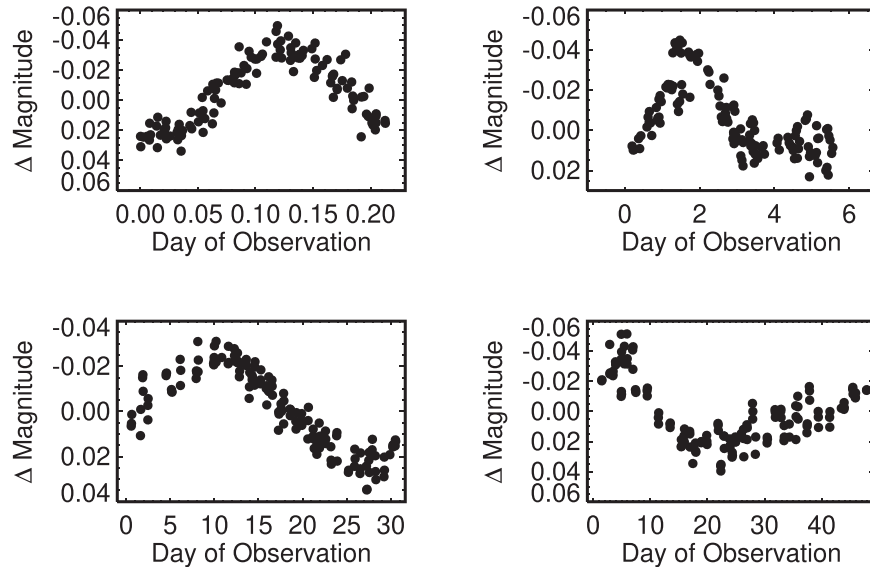


**Figure 15.** Phase-folded PTF light curves for variable stars in the vicinity of Ruprecht 147 rotators, with periodicities ranging from 5 hr to 50 days (shown), with additional longer-period variables noted. The cases shown here are drawn from the reference stars with strong peak powers in their LS periodograms plotted in the panels of Figure 4. Top left: a neighbor to EPIC 219297228, Gaia DR2 4087800102544050688 is a distant G-type subgiant:  $G = 15.13$ ,  $(G_{BP} - G_{RP}) = 1.017$ ,  $\varpi = 0.409$  mas (2344 pc; RUWE = 1.84), with  $T_{\text{eff}} \approx 5650\text{--}5810$  K assuming  $E(B - V) = 0.12\text{--}0.16$ . Top right: a neighbor to EPIC 219234791, Gaia DR2 4087708155887598080 is a main-sequence K0 dwarf:  $G = 14.10$ ,  $(G_{BP} - G_{RP}) = 1.21$ ,  $\varpi = 2.63$  mas (377 pc; RUWE = 1.03), with  $T_{\text{eff}} \approx 5294$  K assuming  $E(B - V) = 0.11$ , the R147 value. Bottom left: a neighbor to EPIC 218984438, Gaia DR2 4084649348891870464 is a distant K giant:  $G = 15.06$ ,  $(G_{BP} - G_{RP}) = 1.19$ ,  $\varpi = 0.13$  mas (5575 pc; RUWE = 0.99). Bottom right: a neighbor to EPIC 219234791, Gaia DR2 4087710732868011904 is a distant K giant:  $G = 14.46$ ,  $(G_{BP} - G_{RP}) = 1.42$ ,  $\varpi = 0.18$  mas (4598 pc; RUWE = 1.03). Distances are taken from Bailer-Jones et al. (2018).

## Appendix D

### $P_{\text{rot}}$ Validation Strategies, a Discussion of Outliers and Nondetections, and Notes on Other Stars

Table 1 provides notes on individual stars. This appendix provides supplemental material and expanded discussion to clarify those notes using case studies. References to the relevant appendices are provided in the table.

#### D.1. The $P_{\text{rot}}$ Distribution for the Nonbenchmark Rotators of Ruprecht 147

As explained in Section 4.1, we crafted a benchmark sample of rotators by rejecting photometric binaries and spectroscopic binaries that are known or suspected to have short orbital periods. We also rejected three stars based on discrepancies between the  $P_{\text{rot}}$  apparent in the light curve and the chromospheric activity level evident in their Ca II H and K spectra. The color–period diagram for these nonbenchmark stars is presented in Figure 16. This figure demonstrates that most rapid outliers are short-period spectroscopic binaries. In these cases, tidal interactions are almost certainly responsible for their rapid rotation. There are also a few long-period outliers at 28–30 days (EPIC 219442294 and EPIC 219634222); perhaps the signals from both companions of each binary are interfering and causing spurious periodicities to dominate the periodogram analysis. In the remainder of this appendix, we provide notes on additional stars not already included in the main paper.

#### D.2. Rapid Solar Analogs? Some Yes, Some No

At a given mass, rotation period tightly correlates with chromospheric emission. Considering a sample with a range of masses, Noyes et al. (1984) found that dividing the rotation periods for stars by their convective turnover times (i.e., Rossby number,  $R_o = P_{\text{rot}}/\tau_{\text{CZ}}$ ) also yielded a tight relationship, referred to as the activity–Rossby relation (see also Mamajek & Hillenbrand 2008).

We measured chromospheric activity via Ca II H and K line core emission for solar-analog stars using high-resolution spectra with high signal-to-noise ratios obtained with the Magellan/MIKE and MMT/Hectochelle spectrographs (data collection and reduction described by Curtis 2016). We measured the  $\log R'_{\text{HK}}$  activity index following Noyes et al. (1984) and Wright et al. (2004). Curtis et al. (2018) present an example of this procedure applied to the planet host K2-231. The results from our full Ca II H and K survey of FGK members will be presented in a separate study.

In Section 4.2.1, we identified two solar twins, which appear to be single according to all available astrometric, photometric, AO, and RV data. And yet, they are rotating rapidly relative to expectations from NGC 6819 and a gyrochronology model interpolating between Praesepe’s color–period distribution and the Sun’s period. Furthermore, both stars—EPIC 219503117 (CWW 85,  $\log R'_{\text{HK}} = -4.44$  dex) and EPIC 219692101 (CWW 97,  $\log R'_{\text{HK}} = -4.58$  dex)—have anomalously high chromospheric emission, consistent with their rapid rotation periods. Figure 17 presents a portion of the MMT/Hectochelle spectrum for CWW 85 centered on the Ca II H line, which shows that the chromospheric activity for this star is greatly enhanced relative to the Sun, as is expected for its rapid rotation. However, their high activity levels are inconsistent with expectations for 2.7 Gyr old solar twins based on the Sun’s present range, the trend of declining activity with age

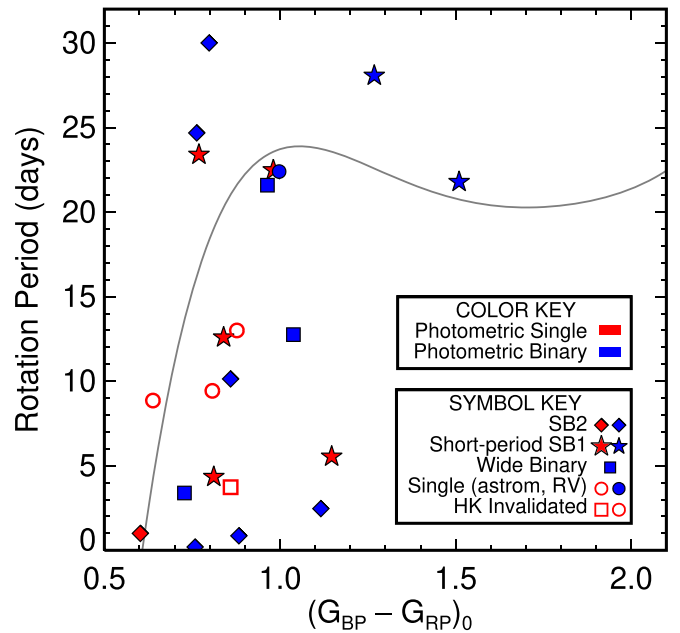


**Figure 16.** Color–period distribution for nonbenchmark stars in Ruprecht 147. The benchmark rotators of Ruprecht 147 are represented by the polynomial model (gray line; see Table 4 and Figures 5 and 6). Filtering out short-period binaries and photometric binaries rejects most  $P_{\text{rot}}$  outliers. Stars that are classified as photometric binaries are shaded blue, and the photometrically single stars are shaded red. Spectroscopic binaries with short orbital periods are shown with diamond symbols (SB2s) and five-point-star symbols (SB1s) and make up most of the  $\lesssim 5$ -day outliers. Astrometric binaries and long-period SB1s are marked with squares but were only rejected as benchmarks if they also exhibited excess luminosities (i.e., no filled red squares are in this figure). Stars that appear single according to astrometry and RVs, but which are photometric binaries, are marked with circles. Three stars are plotted with open symbols to indicate that they have invalidated periods. In these cases, their Ca II H and K spectra reveal inactive chromospheres, which demonstrate that the rapid rotation apparent in their light curves cannot be hosted by these stars.

seen in solar twins in the field (e.g., Lorenzo-Oliveira et al. 2018), and data for other benchmark clusters (Giampapa et al. 2006; Mamajek & Hillenbrand 2008). We suggested that these overactive and rapid stars might be “blue lurkers.” Otherwise, perhaps they are merely binaries with short orbital periods and high mass ratios seen nearly face-on (so that they exhibit no detectable photometric excess or RV variability). Either way, they are clearly anomalous.

In the nonbenchmark color–period distribution presented in Figure 16, the symbols for most rotators are filled in, whereas three are represented by outlined symbols indicating that we rejected their apparent  $P_{\text{rot}}$  from our catalog. These three stars are also solar twins: EPIC 219800881 (K2-231, CWW 93,  $T_{\text{eff}} = 5695$  K,  $P_{\text{rot}} = 13.0$  days,  $\log R'_{\text{HK}} = -4.82$  dex; Curtis et al. 2018), EPIC 219409830 (CWW 76,  $T_{\text{eff}} = 5826$  K,  $P_{\text{rot}} = 9.43$  days,  $\log R'_{\text{HK}} = -4.86$  dex), and EPIC 219256928 (CWW 88,  $T_{\text{eff}} = 5641$  K,  $P_{\text{rot}} = 3.7$  days,  $\log R'_{\text{HK}} = -4.78$  dex). All are photometrically single, the first two pass all single-star criteria, and the third is an astrometric binary candidate and a known long-period SB1. None are expected to be affected by tidal interactions, and yet their periods appear rapid. However, the chromospheric emission we measured from MIKE spectra shows that these stars are inactive. The right panel of Figure 17 shows the case of EPIC 219409830, the activity of which is on par with solar maximum, as is expected for the age of Ruprecht 147. According to the well-established relationship between

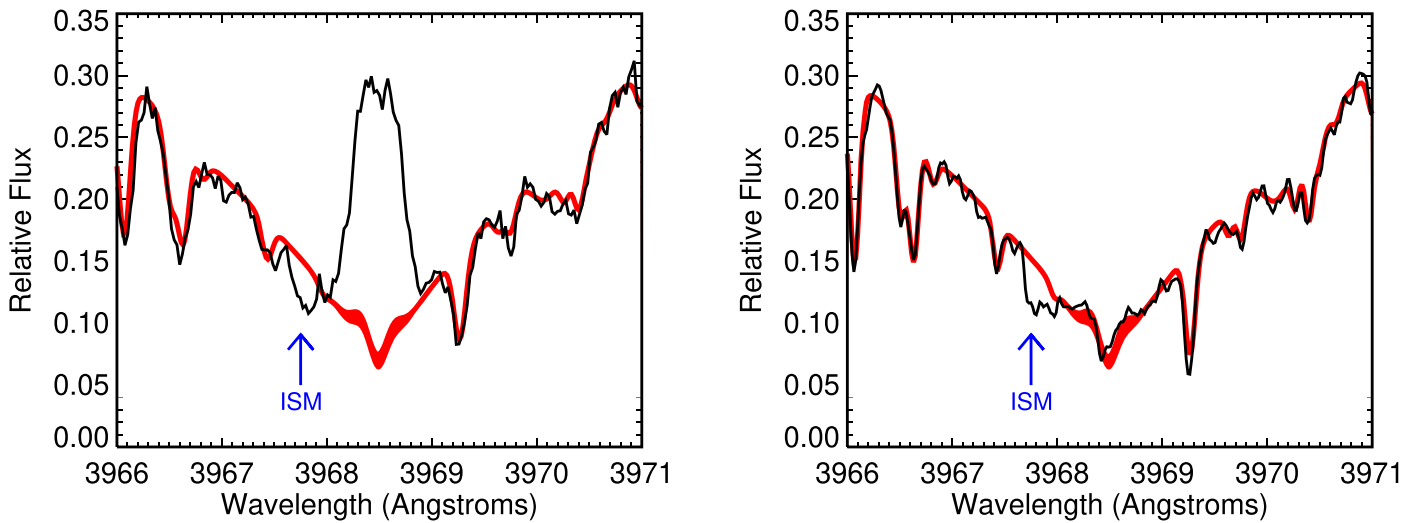


**Figure 17.** Ca II H spectra for two solar twin members of Ruprecht 147 (black lines): EPIC 219503117 (left panel; CWW 85,  $T_{\text{eff}} = 5719$  K,  $\log R'_{\text{HK}} = -4.44$  dex,  $P_{\text{rot}} = 11.0$  days; spectrum from Magellan/MIKE) and EPIC 219409830 (right panel; CWW 76,  $T_{\text{eff}} = 5819$  K,  $\log R'_{\text{HK}} = -4.86$  dex, apparent  $P_{\text{rot}} = 9.4$  days; spectrum from Magellan/MIKE). The range of the contemporary solar cycle is represented with SOLIS/ISS spectra of the Sun taken on 2008 May 03 and 2014 July 1 (red shading). Note the interstellar absorption line blueward of the Ca II H line core (for more on interstellar medium absorption and its impact on Ca II H and K emission metrics, see Curtis 2017). While the K2 light curves of each of these targets show variability indicative of rapid  $\sim 10$ -day rotation, only CWW 85 at left exhibits enhanced chromospheric emission at a level commensurate with this rotation. In contrast, the Ca II emission for CWW 76 is consistent with the modern solar maximum, as is typical for the solar twins in this cluster and is expected for its age. The K2 light curve for the active star (CWW 85, EPIC 219503117) shows an 11-day periodicity made clear by asymmetries in the alternating dip patterns that reveal its true period. However, the K2 light curve for the inactive star (CWW 76, EPIC 219409830) shows a symmetric pattern with a period that is at odds with its inactive chromosphere. Doubling the apparent period would resolve the tension between its rotation and chromospheric emission. The photometric amplitude ( $R_{\text{var}}$ ) is also  $5\times$  lower for this star relative to its active twin and is inconsistent with analogous stars in the Kepler field (median value of 95 reference stars is  $8.3\times$  higher); this likewise suggests that the true period is double the apparent value. Alternatively, the light curve for CWW 76 might be affected by a background star. We searched Gaia DR2 for neighbors within  $20''$  with  $G$  within 3 mag of our target and found one match: Gaia DR2 4088004714786985344, at  $7''8$  and 2.2 mag fainter than our target—a subgiant with a similar photometric color. If this scenario is correct, then the background star would have a much larger photometric amplitude, which has been diluted by our brighter target. These plots are produced following the same procedure used for K2-231 in Figure 5 by Curtis et al. (2018).

chromospheric emission and stellar rotation (e.g., Noyes et al. 1984; Mamajek & Hillenbrand 2008) and between chromospheric emission and stellar age for solar twins (e.g., Lorenzo-Oliveira et al. 2018), we argue that there is no way that the periodic variability seen in the light curves indicates the true rotation periods for these stars. Thus, we reject these  $P_{\text{rot}}$  measurements as invalid.

Regarding EPIC 219409830 (CWW 76, shown in the right panel of Figure 17), the Gaia DR2 photometry and our MIKE spectroscopy indicate that it is only 80–100 K warmer than CWW 85 (the active star shown in the left panel of the same figure), i.e., they are nearly twins. The LS periodograms for the K2 light curves for each indicate that they have similar rotation periods (9.4 and 11.0 days for CWW 76 and CWW 85, respectively). However, their Ca II H and K spectra definitively demonstrate that CWW 85 is magnetically active and CWW 76 is inactive; thus, their rotation periods cannot be similar. Doubling the apparent period of CWW 76 would increase its  $P_{\text{rot}}$  to  $\approx 19$  days, which is equal to the value expected from the activity–Rossby relation (Mamajek & Hillenbrand 2008). Its photometric amplitude ( $R_{\text{var}}$ ) is also  $5\times$  lower than CWW 85 (its active twin) and is inconsistent with analogous stars in the Kepler field (the median value of 95 reference stars is  $8.3\times$  higher); this likewise suggests that the true period is double the apparent value. Alternatively, the light curve for CWW 76 might be affected by another star blended in the photometric aperture. EPIC 219409830 appears to be single (11 HARPS RVs have a standard deviation of  $40 \text{ m s}^{-1}$  and are consistent with RVs from Lick, 2012 MIKE, and Gaia),

so binarity is not likely the cause. We searched Gaia DR2 for neighbors within  $20''$  with  $G$  within 3 mag of our target and found one match: Gaia DR2 4088004714786985344, at  $7''8$  and 2.2 mag fainter than our target—a subgiant with a similar photometric color. If this scenario is correct, then the background star would have a much larger photometric amplitude, which has been diluted by our brighter target. We opt to remove this target from our benchmark sample at this time because we have not been able to conclusively determine its period.

*EPIC 219256928.*—This inactive star with an apparently rapid rotation period is an SB1 with an unknown orbital period. In this case, perhaps the light-curve modulation comes from a fainter, more active secondary star.

*EPIC 219774323.*—We report a period of 6.9 days for this star. However, the period we infer from its  $\log R'_{\text{HK}}$  using the activity–Rossby relation is approximately double that value. There is a weak hint of this in the light-curve timing analysis, where the periods for the odd sets and even sets of dips are different; however, this difference is not significant enough to warrant our altering of the LS period. We do note that our Praesepe-based gyrochrone predicts a period for this star of 12.9 days, which is only 7% smaller than the double-period. We left the apparent  $P_{\text{rot}}$  unchanged in the table.

The  $P_{\text{rot}}$  and  $\log R'_{\text{HK}}$  for EPIC 219601739, EPIC 219722212, and EPIC 219721519 are consistent. Results for all other members with Ca II H and K spectra will be presented in a separate study.

### D.3. Binaries with Inactive Primaries and Low-mass Secondaries

Late F and early G dwarfs in Ruprecht 147 are expected to be inactive, according to the activity–Rossby–age relation (Mamajek & Hillenbrand 2008), and confirmed by our unpublished Ca II H and K survey. In cases where such stars have lower-mass companions (e.g., a K dwarf), those secondaries are expected to be more active owing in part to their longer convective turnover times and hence smaller Rossby numbers given the observed fact that the color–period sequence for the cluster is relatively flat. In these situations, it is possible that the primary’s brightness variations are negligible compared to the secondary’s spot modulation signal, despite the difference in brightness that will dilute the amplitude for the secondary. Therefore, any apparent rotation period might be hosted by the secondary star. We suspect that this is the case for EPIC 219404735, EPIC 219442294, and EPIC 219661601.

*EPIC 219404735.*—This target is an SB2. Modeling the broadband photometry as a binary with a PARSEC isochrone, we find  $M_1 = 1.14 M_\odot$  and  $M_2 = 0.89 M_\odot$  (for details on the method, see Section 3.1.3.1 in Curtis 2016). The K2 light curve shows a clear 24.7-day period, with a double-dip morphology typical for a K dwarf cluster member. Given the inferred masses for each component, we expect periods of 10.3 and 23.6 days. We estimate  $\tau_{CZ} = 6.4$  days with the Cranmer & Saar (2011) formula and the PARSEC  $T_{\text{eff}}$  for the primary; the resulting Rossby number  $\text{Ro} = 3.8$  would be extremely inactive. There are only nine stars in the Kepler sample from McQuillan et al. (2014) with larger Rossby numbers (prepared following the recipe in Appendix F). The more likely explanation is that the K0V secondary is responsible for the rotation period evident in the K2 light curve.

*EPIC 219661601.*—The  $(G_{\text{BP}} - G_{\text{RP}})$  for this star indicates  $T_{\text{eff}} = 5856$  K. It has a modest photometric excess ( $\Delta G = 0.33$  mag), but not large enough to satisfy our photometric binary criteria. With  $\text{RUWE} = 1.53$ , the star is a candidate wide binary. Our SME analysis of a MIKE spectrum indicates  $T_{\text{eff}} = 6045$  K (Bragaglia et al. 2018 measured  $T_{\text{eff}} = 5987$  K from HARPS spectra). Photometric modeling yields  $M_1 = 1.107 M_\odot$  (6054 K) and  $M_2 = 0.721 M_\odot$  (4477 K). This revised photometric temperature for the primary is consistent with our spectroscopic measurement. According to our gyrochrone model for NGC 6819 and Ruprecht 147, we expect such a star to have a 13.5-day period. Even if the 5856 K temperature is correct, this would make it a twin of EPIC 219601739 (5834 K), which has  $P_{\text{rot}} = 16.7$  days. In other words, the apparent period of 20.5 days for EPIC 219661601 is too slow. However, the Mamajek & Hillenbrand (2008) activity–Rossby–age relation predicts  $\log R'_{\text{HK}} = -4.975$  dex for the primary, with a Rossby number  $\text{Ro} \approx 2.1$ , which means that we should expect the primary to be quite inactive. This should make measuring the rotation period from white-light brightness variations challenging. Instead, we suggest that the 20.5-day rotation signal is hosted by the K dwarf secondary. According to the temperature found from our isochrone analysis, our Ruprecht 147 model expects a 21.6-day period, which is equal to the period measured from the light curve.

### D.4. K Dwarfs with Ambiguous Rotation Periods and the Power of Dip Timing Analysis

*EPIC 219333882.*—This star ( $T_{\text{eff}} \approx 4950$  K,  $M_* \approx 0.83 M_\odot$ , K2V) has a K2 light curve that we found challenging to interpret. There is a clear 11.6-day signal, which is favored by the LS periodogram. However, every third minimum is shallower than the other two, leading the ACF to favor a 34.8-day period. Furthermore, the PTF light curve shows a 24.5-day periodicity. We have only one RV for this star, from MIKE, and it is consistent with being a single member. The Gaia proper motion and photometry also indicate that it is a single star; however,  $\text{RUWE} = 1.6$ , so it might actually be a wide binary. There are four stars in Gaia DR2 within  $15''$ , but all are significantly fainter (4.1–7.3 mag in  $G$ ), so background blending is unlikely a concern.

We examined the K2 light curve by timing the dips and found an asymmetric spacing between the minima indicating that they come in pairs. The average spacing of the odd minima is  $11.0 \pm 0.7$  days, and the spacing of the even minima is  $12.3 \pm 0.6$  days, totaling to 23.3 days for a full rotation. If true, the first LS and ACF peaks would indicate the half-period harmonics. We suggest that this confusing pattern is caused by two active regions with particular growth and decay patterns that make it look like three peaks per rotation, whereas the PTF data happened to catch the star with only one dominant active region. This switching between one and two active regions is fairly common at this temperature and rotation period ( $T_{\text{eff}} \approx 5000$  K,  $P_{\text{rot}} \approx 24$  days); Figure 4 in Basri & Nguyen (2018) indicates  $N_{\text{single}}/N_{\text{double}} \approx 0.5$ . Alternatively, perhaps the confusion arises from interference from a faint companion. Although this star is RV- and photometrically single, the astrometry indicates that it is a wide binary. Perhaps the variability of the faint secondary is interfering with the primary’s rotational modulation pattern and producing this confusing signal. Based on this careful inspection of the K2 light-curve minima timing and supported by the clear signal in the PTF light curve, we conclude that the most likely rotation period for this star is 23.4 days, which places it on the slow sequence.

*EPIC 219346771.*—The K2 light curve for this star ( $T_{\text{eff}} \approx 4247$  K,  $M_* \approx 0.72 M_\odot$ , K5V) is also confusing at first glance and appears to show two sets of periods: a long period of 27–30 days, with a second set of dips spaced every 8–10 days. However, timing successive pairs of dips shows that the odd pairs (first–second, third–fourth, fifth–sixth) are spaced at  $8.1 \pm 0.7$  days and the even pairs (second–third, fourth–fifth, sixth–seventh) are spaced at  $11.0 \pm 0.5$  days. Combining these timings, we conclude that the period is likely 19.1 days, which would place it on the slow sequence as well. The K2 analysis panel for this star (in the Figure 3 set online) includes vertical lines marking off the odd dips to aid the reader’s interpretation of this timing analysis. Unfortunately, this star was not observed by PTF, so we cannot independently verify the timing period.

### D.5. Unresolved Background Blends

*EPIC 219610822.*—The K2 light curve for this star ( $T_{\text{eff}} \approx 5035$  K,  $M_* \approx 0.85 M_\odot$ , K0V) contains an EB with  $P_{\text{orb}} = 29.55$  days, with apparent eclipse depths of 0.1% and 0.08%. We suspect that the EB is in the distant background

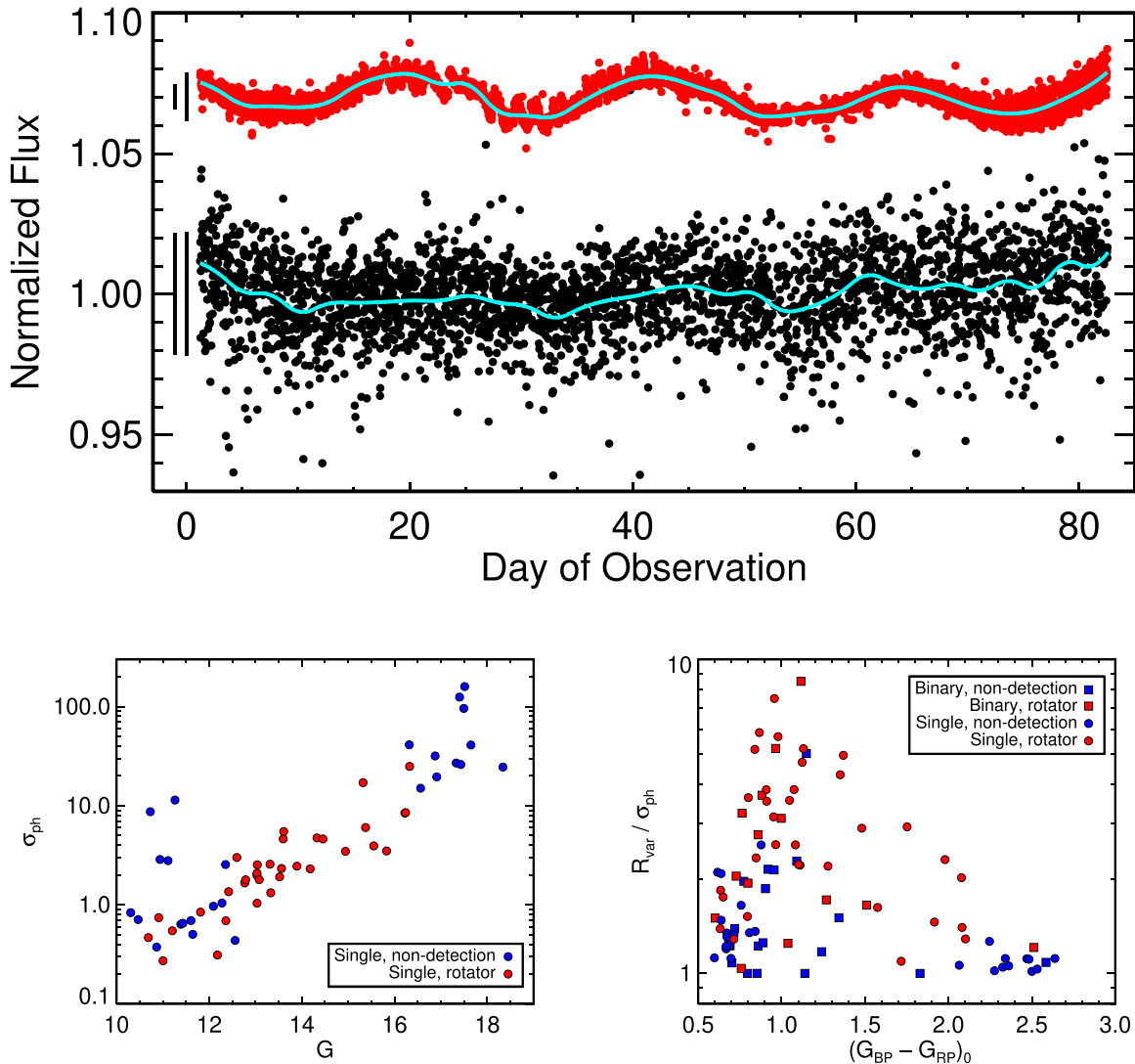


**Figure 18.** Top: light curves for two analogous stars illustrate how abnormally high photometric noise is suppressing our sensitivity to  $P_{\text{rot}}$  in certain nondetection cases. These two stars are EPIC 219353203 (top, red points,  $P_{\text{rot}} = 21.8$  days) and EPIC 219616992 (bottom, black points,  $P_{\text{rot}}$  is not clearly evident, but the LS periodogram favors a 20.7-day period). The vertical lines at the left of the figure mark the photometric precision ( $\sigma_{\text{ph}}$ ) and amplitude ( $R_{\text{var}}$ ). In the top case, the photometric precision for this PDCSAP light curve is  $6.7\times$  better than for the superstamp light curve for the bottom case. Bottom left: the photometric precision for likely or effectively single stars is plotted as a function of apparent  $G$  magnitude. The noise increases toward fainter magnitudes. We report  $P_{\text{rot}}$  for stars shaded red, while the blue-shaded stars are nondetections. Between  $13 < G < 16$ , our success rate is high, with only three nondetections. Brighter (i.e., more massive) stars tend to be inactive by 2.7 Gyr, making their photometric amplitudes very weak, and we therefore report only a few  $P_{\text{rot}}$  detections. At  $G > 16$ , the typical noise increases by six times compared to the  $14 < G < 16$  range, which likely is responsible for their nondetections. Bottom right: we plot the ratio of the amplitude to the noise for an expanded sample that includes the stars from the left panel and adds in the binaries (marked with squares). Stars with ratios  $> 1$  tend to have visually validated  $P_{\text{rot}}$  detections. Where this is not the case, it is often because the light curves exhibit morphologies that resist simple interpretation, i.e., they are binaries that show clear spot modulation patterns (and therefore have a high  $R_{\text{var}}/\sigma$  ratio), but the signals from both companions are likely interfering and confusing the periodogram analysis.

(based on TRES RVs that show that the cluster member is not the host) and is blended with the cluster member. We also measured  $P_{\text{rot}} = 22.8$  days in the K2 light curve. Given the large amplitude of the spot modulation signal, we assume that it is associated with the cluster member and not the background EB.

It is possible that some of the rotation signals we measure in our sample are caused by other background blends. We can check Gaia DR2 for bright neighbors in the K2 photometric apertures and assess how such blends might bias our results. The CMD panels in Figure Set 3 show the full Ruprecht 147 catalog, together with the target star, and neighboring stars within  $12''$  that might be blended in the K2 photometric aperture. We plot both the apparent  $G$  and absolute  $M_G$  magnitudes (calculated using the parallax and then adjusted to

the R147 distance modulus by adding 7.4 mag) to illustrate that these blended stars tend to be significantly fainter than the target. Furthermore, their spectral types and luminosity classes are often inconsistent with the rotation signal apparent in the light curve. For example, rapidly rotating giants are rare (Pinsonneault et al. 2014), although they can rotate as fast as 13–55 days (Costa et al. 2015). Still, it is unlikely that each one of these background giants that happens to contaminate our targets also rotates rapidly.

*EPIC 219297228.*—This star has a bright neighbor (Gaia DR2 4087799651563238912), which is only 0.43 mag fainter, is 0.1 mag redder in  $(G_{\text{BP}} - G_{\text{RP}})_0$ , and is separated by only  $8''.25$  ( $\approx$ two K2 pixels). This flux from this neighbor is certainly affecting the K2 observations. However, we can confidently attribute the 23-day rotation period signal to our

target and not this interloper for two reasons. First, its absolute magnitude indicates that it is a distant AGB star, whereas the light-curve modulation looks like that of a middle-aged K dwarf. Second, the two stars are resolved in our PTF imaging, so we can cleanly extract light curves for each star. According to our PTF light curve, our target has a 23.8-day period, confirming the K2 result.

#### D.6. Photometric Amplitudes, Noise, and Nondetections

The amplitude of the brightness fluctuations due to rotating spots can be assessed from the typical range of minima to maxima, called  $R_{\text{var}}$  (Basri et al. 2010). We calculate this according to the interval between the 5th and 95th flux percentiles for the normalized light curves (McQuillan et al. 2013). We also estimate the photometric precision using this interval technique performed on detrended light curves. For this, we fit a cubic basis spline to the light curves with break points spaced at 2.5 days and then divide out the model. This removes spot modulation patterns and any remaining low-order systematics and isolates the photometric noise, which we refer to as  $\sigma_{\text{ph}}$  and plot in the bottom left panel of Figure 18. The ratio of  $R_{\text{var}}/\sigma_{\text{ph}}$ , plotted in the bottom right panel of the same figure, is  $\approx 1$  for most of our nondetections. Apparently in these cases the noise is too high relative to the spot signal. Stars with clear rotation signals tend to have a higher ratio: the median value for 33 rotators is 2.3 and ranges from 1.2 to 7.1.

There are other stars with ratios  $>1$  for which we do not report a  $P_{\text{rot}}$ . Many are binaries with large photometric excesses; in these cases, the rotation signal from the secondary is likely interfering with the primary’s and confusing the  $P_{\text{rot}}$  analysis. Although multiple periods have been measured for binaries in the Pleiades (Rebull et al. 2016) and Praesepe (Douglas et al. 2017; Rebull et al. 2017), those younger stars tend to spin much more rapidly than Ruprecht 147 stars, and often the second periodicity is fairly rapid. For example, 46 of the 58 multiperiodic stars in Praesepe analyzed by Douglas et al. (2017) have secondary  $P_{\text{rot}} < 5$  days. This helps disentangle the two signals. However, in our case where there are two stars likely spinning at  $\sim 20$  days, this is all but hopeless.

Restricting our list to only the main-sequence dwarfs that are not classified as photometric binaries, SB2s, or short-period SB1s (i.e., our “benchmark” targets), there are three stars that lack  $P_{\text{rot}}$  yet have ratios  $>1$ . EPIC 219800881 and EPIC 219256928 are addressed in Appendix D.2; briefly, their Ca II H and K spectra show them to be magnetically inactive, which invalidates the rapid periods apparent in their light curves. Regarding EPIC 219698970, its superstamp light curve is strongly affected by a systematic, which probably biased  $R_{\text{var}}$  toward an artificially high value.

*EPIC 219616992.*—This star ( $T_{\text{eff}} \approx 3765$  K,  $M_{\star} \approx 0.54 M_{\odot}$ , M1V) is located in the K2 superstamp. The top panel of Figure 18 plots light curves for it and an analogous star (i.e., similar color and magnitude)—the light curve plotted in red at the top of the panel shows EPIC 219353203, which has a clear period of 21.8 days. The light curve plotted in black below that star shows EPIC 219616992—its period is not obvious in this light curve, and we suspect that the cause is the abnormally high photometric noise ( $6.7\times$ ), which is suppressing our sensitivity to its period, given the spot amplitude expected from the analogous star. The figure shows a smoothed version of the noisy light curve (using a cubic basis spline used to calculate  $\sigma_{\text{ph}}$ ); there are

subtle periodic dips spaced at 20.7 days. However, we require unambiguous visual validation of the  $P_{\text{rot}}$  before accepting it into our benchmark rotator sample, and so this star remains a nondetection.

*EPIC 219675090.*—A similar analysis of the K2 superstamp light curve for this star ( $T_{\text{eff}} \approx 4055$  K,  $M_{\star} \approx 0.64 M_{\odot}$ , K5V) relative to an analog shows that its light curve is also abnormally noisy— $4.8\times$  higher than stars of similar color and magnitude, which appears to be masking some periodic structure in the light curve that is weakly apparent in the second half of the light curve. The K2 analysis panel in Figure Set 3 shows the smoothed version of its light curve, which reveals a repeating sequence of narrow and deep dips followed by shallower and broader dips. The timing of these dips indicates a period of 17.9 days, which we adopt as the validated  $P_{\text{rot}}$  for this star. If this is the true period, it too falls on the slow sequence for Ruprecht 147.

The bottom left panel of Figure 18 shows that the photometric noise increases by nearly six times at  $G > 16$  (based on the median  $\sigma_{\text{ph}}$  for the 12 stars on our list with  $14 < G < 16$  and the 17 with  $G > 16$ ). We selected analogous rotators from the Kepler sample (McQuillan et al. 2014): for the 721 stars with  $(G_{\text{BP}} - G_{\text{RP}}) > 2$ ,  $P_{\text{rot}} > 10$  days, the median amplitude is  $R_{\text{var}} \approx 7$  ppt, and 90% range between 3 and 20 ppt. Our nine faintest stars lacking periods with  $16.3 < G < 18.3$  have  $\sigma_{\text{ph}} = 15, 19, 25, 27, 28, 32, 43, 126,$  and 161 ppt. We conclude that the light curves for our  $G > 16$  targets are too noisy to confidently detect stellar rotation.

#### D.7. EPIC 219489683 Is in the Kepler Intermediate-period Gap

Section 6.7 discussed how the distribution of color versus rotation period for the Kepler field derived by McQuillan et al. (2014) shows a bimodality, where there is a narrow gap that approximately traces a line of constant Rossby number. We explained that the Ruprecht 147 rotation period sequence crosses the gap and concluded that this challenges the scenario where the gap is formed by a temporary lull in star formation rate (i.e., the gap does not have a single-valued age, so it could not have been created by a single event in time).

One member of Ruprecht 147, EPIC 219489683, has a color and period that appear to place it in the gap, shown in the left panel of Figure 19. However, interstellar reddening smears out the gap and shifts it relative to the Ruprecht 147 sequence, which has a known reddening value. If no reddening correction is applied to Ruprecht 147, then the star would fall on the edge of the gap. The stars in the Kepler field are likely reddened somewhat less than Ruprecht 147 (see Appendix F), so the true location of EPIC 219489683 in this distribution is probably somewhere between the  $A_V = 0.0$  and  $A_V = 0.3$  cases.

Reinhold et al. (2019) explained that the gap coincided with a decrease in amplitude of the spot modulation signal, which they suggested is caused by a net cancellation of dimming from spots and brightening from plage. The right panel of Figure 19 plots the  $(G_{\text{BP}} - G_{\text{RP}})_0$  versus  $R_{\text{var}}$  for a selection of Kepler stars drawn from McQuillan et al. (2014) with periods within 10% of the Ruprecht 147 sequence model. This figure also shows our  $R_{\text{var}}$  measurements for the Ruprecht 147 rotator sample and highlights EPIC 219489683. We were surprised to find that it showed a large photometric amplitude compared to similar stars in the Kepler field, defying expectations from Reinhold et al. (2019). Examining the magnetic activity of this



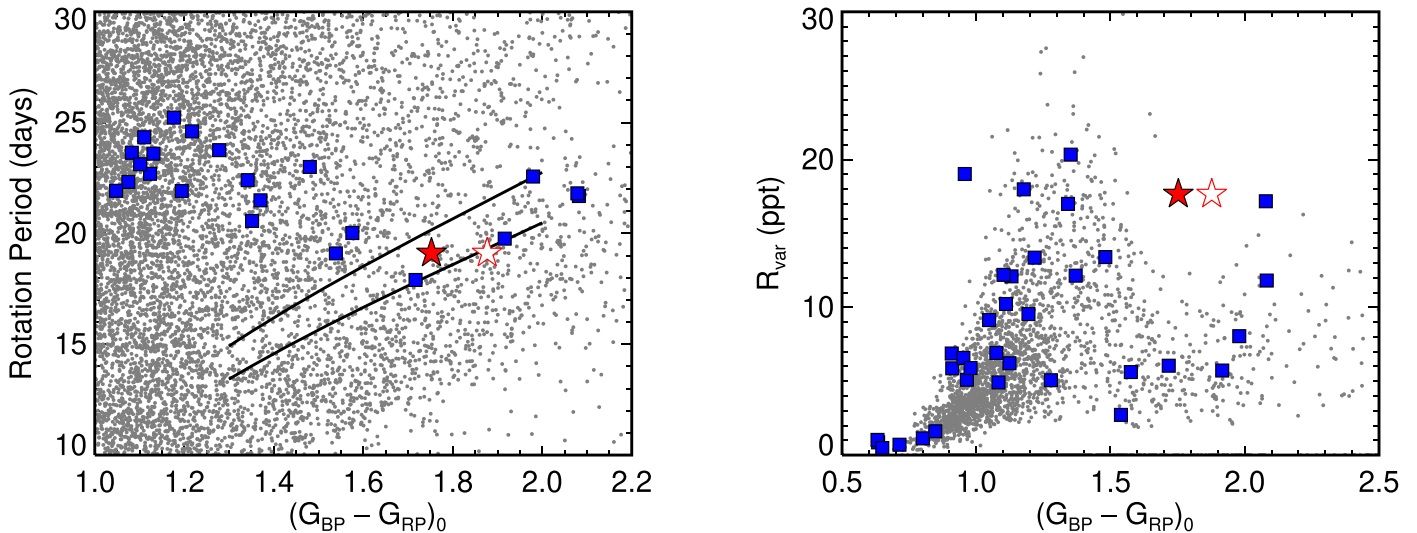


**Figure 19.** EPIC 219489683 falls in the intermediate-period gap. Left: color vs. period for Kepler stars (gray points; McQuillan et al. 2014). The Kepler colors have been dereddened using the  $E(B - V) = 0.04 \text{ mag kpc}^{-1}$  law, which approximates the median reddening pattern derived in Appendix F and the following extinction coefficients:  $E(G_{\text{BP}} - G_{\text{RP}}) = 0.415 A_V = 0.134 E(B - V)$ . The black lines trace  $\text{Ro} = 0.45$  and  $0.50$  using Cranmer & Saar (2011) convective turnover times and approximately trace the intermediate-period gap. The benchmark rotators for Ruprecht 147 (blue squares, dereddened using  $A_V = 0.30 \text{ mag}$ ) intersect this gap, and EPIC 219489683 (marked with a filled red star with  $A_V = 0.3$  applied) falls right in the middle of the gap—it is also marked with an open red star with no reddening correction applied. This illustrates how essential accurate and precise reddening corrections are for analyzing such features in color–period distributions. Right: color vs.  $R_{\text{var}}$  for Kepler stars with periods within 10% of the Ruprecht 147 sequence model. The benchmark rotators for Ruprecht 147 approximately follow the same distribution, with one notable exception: EPIC 219489683 has an abnormally large  $R_{\text{var}}$  for its color and period. The light curve for the outlying blue square at  $((G_{\text{BP}} - G_{\text{RP}})_0 \approx 0.96, R_{\text{var}} \approx 19 \text{ ppt})$  shows significant spot evolution; the amplitude for the later 2/3 of the light curve is more consistent with the Kepler and Ruprecht 147 distributions.

star and other Ruprecht 147 stars expected to fall in and near the gap might shed light on the mechanism responsible for carving out this feature in the color–period distribution.

#### D.8. Estimating $P_{\text{rot}}$ Uncertainties

Lamm et al. (2004), Agüeros et al. (2018), and others estimated  $P_{\text{rot}}$  uncertainties using the width of a Gaussian fit to the primary LS periodogram peak. For example, there are five rotators with similar color in the NGC 752 sample (Agüeros et al. 2018), and the mean reported error is 2.4 days. Separately, the  $P_{\text{rot}}$  dispersion as a function of color combines measurement uncertainties with the degree of convergence of the slow sequence (how intrinsically tight the slow sequence is) and the range of differential rotation in these stars. The standard deviation for this NGC 752 sample is 1.4 days, which suggests that the periodogram width is an overestimate of the true uncertainty for that sample.

For both the K2 and PTF rotators, the width of the periodogram peak indicates a typical uncertainty of  $\lesssim 10\%$  for our targets. Focusing on the slowly rotating sequence cooler than  $T_{\text{eff}} < 5500 \text{ K}$ ,  $P_{\text{rot}} = 22.6 \pm 1.7 \text{ days}$  (8%). Finally, there are three stars for which we have measured  $P_{\text{rot}}$  with both K2 and PTF—the differences in the periods measured from each survey are 0.1, 0.4, and 1.6 days, or  $< 7\%$ . For this work, given that we observe only two to four full rotation cycles in the light curves, we adopt a 10% uncertainty for all rotators, which amounts to  $\approx 15\%$  in gyrochronal age per star.

#### D.9. Notes on Additional Stars

*EPIC 219590752.*—The Gaia DR2 RV error is  $4.8 \text{ km s}^{-1}$ , which, according to our criteria, would classify it as a candidate short-period binary. However, HARPS RVs collected over

400 days have a dispersion of  $18 \text{ m s}^{-1}$ , indicating that if this is a spectroscopic binary, it must have a long orbital period. We reclassify it from a short- to long-period SB1.

*EPIC 219582840.*—This star has an RV variance-to-error ratio  $e/i = 5.4$ , which classifies it as a candidate short-period binary according to our  $e/i > 4$  threshold. However, two MIKE RVs taken 18 days apart differ by only  $1.5 \text{ km s}^{-1}$ , which is consistent within the measurement uncertainties. Considered together with Hectochelle RVs taken 2 yr earlier, the difference of  $7.5 \text{ km s}^{-1}$  confirms it is an SB1. We reclassify it as a long-period SB1. We acknowledge that our classifications could be inaccurate until orbital solutions are available for these stars.

## Appendix E Fundamental Properties of NGC 6819

NGC 6819 is a rich, well-studied cluster. Cantat-Gaudin et al. (2018) identified 1915 members with Gaia DR2 data, and Milliman et al. (2014) reported 566 RV-single members and 93 spectroscopic binary members.

Metallicity measurements in the recent literature range between  $[\text{Fe}/\text{H}] = -0.06$  and  $+0.10$  dex and have an average value of  $+0.03$  dex (Bragaglia et al. 2001; Friel et al. 2002; Marshall et al. 2005; Anthony-Twarog et al. 2014, 2018; Lee-Brown et al. 2015; Milliman et al. 2015; Ness et al. 2016; Slumstrup et al. 2017; Cummings et al. 2018; Deliyannis et al. 2019). We also cross-matched the Cantat-Gaudin et al. (2018) cluster membership catalogs for NGC 6819 and M67 with the LAMOST DR4 catalog (Xiang et al. 2015) and calculated metallicities for each cluster (median and standard deviation): for NGC 6819 we found  $[\text{Fe}/\text{H}] = +0.05 \pm 0.08$  for 54 stars, and for M67 we found  $[\text{Fe}/\text{H}] = +0.05 \pm 0.04$  for 10 stars, indicating that they share a similar metallicity. M67 is

commonly found to have a metallicity and abundance pattern similar to the Sun (Önehag et al. 2011; Liu et al. 2016). Assuming a solar metallicity would make the metallicity of NGC 6819 0.1 dex lower than our value for Ruprecht 147. The SDSS Data Release 16 includes a value-added catalog from the Open Cluster Chemical Analysis and Mapping survey (OCCAM; Donor et al. 2018, 2020),<sup>46</sup> which includes stellar properties and chemical abundances for open cluster members based on APOGEE spectra and Gaia DR2 astrometric membership (Ahumada et al. 2020): for NGC 6819,  $[\text{Fe}/\text{H}] = +0.05 \pm 0.04$  dex, and for Ruprecht 147,  $[\text{Fe}/\text{H}] = +0.12 \pm 0.02$  dex (33 stars). The metallicities appear to be similar enough ( $\lesssim 0.1$  dex) that any minor differences should have negligible impact on this study.

The average interstellar reddening of NGC 6819 has been constrained to  $E(B - V) = 0.14\text{--}0.17$  (Bragaglia et al. 2001; Anthony-Twarog et al. 2014; Cummings et al. 2018; Deliyannis et al. 2019), and it varies significantly across the cluster ( $\Delta E(B - V) \approx 0.05\text{--}0.06$ ; Platais et al. 2013; Anthony-Twarog et al. 2014). The distance modulus is  $(m - M)_0 = 11.90\text{--}11.94$  (Yang et al. 2013; Anthony-Twarog et al. 2014; Cummings et al. 2018). The age is 2.3–2.6 Gyr (Yang et al. 2013; Anthony-Twarog et al. 2014; Brewer et al. 2016b; Cummings et al. 2018; Soydugan et al. 2020), which is approximately coeval with the 2.7 Gyr Ruprecht 147.

### *E.1. The Relative Reddening of NGC 6819 Compared to Ruprecht 147 Using the Red Clump*

Before joining the rotation samples for Ruprecht 147 and NGC 6819, we must determine whether the mean interstellar reddening values are determined consistently. To do this, we make use of each cluster’s red clump population. Red clump giants can serve as distance indicators because of their low intrinsic luminosity dispersion compared to other giants. This is especially true when infrared or near-infrared magnitudes are used because these are relatively insensitive to interstellar dust and stellar metallicity (Paczynski & Stanek 1998; Churchwell et al. 2009; Hawkins et al. 2017).

The red clumps in NGC 6819 and Ruprecht 147 should have essentially identical magnitudes in all bands owing to their similar metallicity and age, except for the fact that NGC 6819 is much more distant and suffers greater interstellar reddening and extinction than the stars of Ruprecht 147. We can use this fact to calculate the relative distance modulus and extinction for NGC 6819 by comparing its red clump to that of Ruprecht 147.

Stello et al. (2011) identified red clump members of NGC 6819 via asteroseismic analysis of Kepler light curves (in their table, class = clump, asteroseismic member = yes). We trimmed that sample by selecting those consistent with single-star membership according to the Hole et al. (2009) RV catalog (bin = SM) and rejected those identified as known or possible blends, leaving us with 10 stars. We list their Gaia DR2 and KIC IDs in Table 6, along with photometric magnitudes from Gaia DR2 ( $G, G_{\text{BP}}, G_{\text{RP}}$ ; Evans et al. 2018), 2MASS ( $J, H, K_S$ ; Skrutskie et al. 2006), and the Wide-field Infrared Survey Explorer (WISE; W1, W2, W3; Wright et al. 2010). Table 6 also identifies five RV-single members of Ruprecht 147 that appear to be red clump stars, based on their K2 asteroseismic power spectra (M. N. Lund et al. 2020, in preparation).

We computed median apparent magnitudes in each band for each cluster and then calculated the distance and extinction values needed to balance their absolute magnitudes, finding  $\Delta(m - M)_0 = 4.57$  and  $\Delta A_V = 0.14$ . Applying our adopted values for Ruprecht 147 ( $(m - M)_0 = 7.4, A_V = 0.30$ ), we find for NGC 6819  $(m - M)_0 = 11.97, A_V = 0.44$ . These values are consistent with the literature values summarized previously, and we adopt our value for this study.

Figure 20 plots the apparent CMDs for NGC 6819 and Ruprecht 147 and highlights the stars with measured rotation periods. This figure also includes representative light curves from each cluster, which illustrates the increased photometric noise for the much fainter members of NGC 6819 relative to our Ruprecht 147 targets.

<sup>46</sup> [https://www.sdss.org/dr16/data\\_access/value-added-catalogs/?vac\\_id=open-cluster-chemical-abundances-and-mapping-catalog](https://www.sdss.org/dr16/data_access/value-added-catalogs/?vac_id=open-cluster-chemical-abundances-and-mapping-catalog)

**Table 5**  
Data for the Pleiades, Praesepe, NGC 6811, NGC 752, NGC 6819, and Ruprecht 147 Clusters

Cluster	Age (Gyr)	$A_V$ (mag)	DR2Name	Oname	RAdeg (deg)	DEdeg (deg)	$(G_{BP} - G_{RP})$	$G$ (mag)	$T_{\text{eff}}$ (K)	$P_{\text{rot}}$ (days)
Pleiades	0.12	0.12	Gaia DR2 67618285777617664	EPIC 210990525	53.88216	22.82339	0.7103	9.7295	6292	2.795
Praesepe	0.67	0.035	Gaia DR2 664327433763175424	EPIC 211988287	129.97927	20.06497	0.6449	9.9914	6396	3.290
NGC 6811	1.0	0.15	Gaia DR2 2128134824634071424	KIC 9716563	294.41070	46.48682	0.5688	13.3127	6842	1.111
NGC 752	1.4	0.10	Gaia DR2 342740730979607808		28.69750	37.83303	2.2698	17.2738	3648	18.850
NGC 6819	2.5	0.44	Gaia DR2 2076489767049653632	KIC 5111207	295.03754	40.20463	0.7896	15.1142	6523	5.420
Ruprecht 147	2.7	0.30	Gaia DR2 4087732516937081088	EPIC 219208969	289.18732	-17.28552	0.7590	10.6879	6381	6.700

**Note.** The column “Oname” provides KIC or EPIC identification numbers where available (NGC 752 was not observed by Kepler/K2, so the field is empty for its stars). The full version includes  $(G_{BP} - G_{RP})_0$  and  $M_G$ , calculated using parallaxes from Gaia DR2 and the listed  $A_V$  values, together with the following approximate relations:  $E(G_{BP} - G_{RP}) = 0.415 A_V$  and  $A_G = 0.86 A_V$ . The  $T_{\text{eff}}$  is based on our empirical color–temperature relation. The color–period distributions for individual clusters are plotted in Figures 12 and 13, and the clusters are plotted together in Figure 7. See Appendix A.3 for details on the adopted cluster properties. (This table is available in its entirety in machine-readable form.)

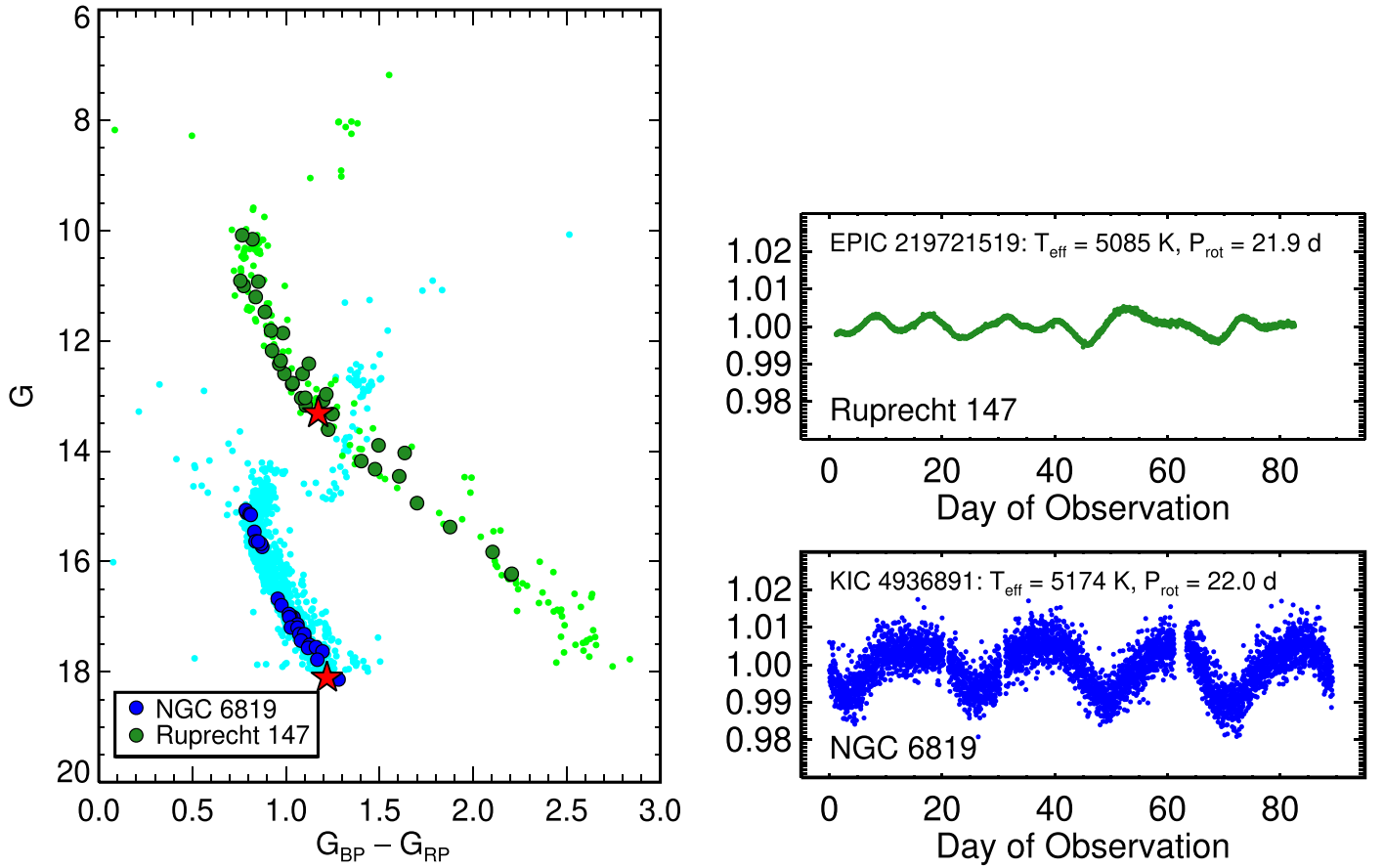


**Figure 20.** Left: Gaia DR2 CMDs for NGC 6819 (cyan points) and Ruprecht 147 (bright green points) and their rotators (blue and dark green points, respectively). Two stars with similar effective temperatures and rotation periods are marked in each cluster with red stars. Right: K2 light curve for EPIC 219721519, in Ruprecht 147 (top;  $T_{\text{eff}} = 5085$  K,  $P_{\text{rot}} = 21.9$  days), and the Kepler light curve for KIC 4936891, in NGC 6819 (bottom;  $T_{\text{eff}} = 5174$  K,  $P_{\text{rot}} = 22.0$  days), the red star symbols marked in the CMD. While the  $P_{\text{rot}}$  are evident in each panel, the noise is significantly increased in the NGC 6819 light curves because stars in that cluster are much fainter and more extinguished ( $\Delta(m - M)_V = 4.71$ , i.e.,  $\approx 77\times$  fainter). Conversely, systematics are typically much stronger in the Ruprecht 147 light curves owing to the increased pointing instability.

**Table 6**  
Data for Red Clump Members of NGC 6819 and Ruprecht 147

Gaia DR2 Source ID	KIC/EPIC	$G$	$G_{BP}$	$G_{RP}$	$J$	$H$	$K_S$	W1	W2	W3
<i>NGC 6819:</i>										
2076300101294355968	5024327	12.761	13.390	12.020	10.992	10.450	10.323	10.154	10.265	10.294
2076392528993233024	5024967	12.803	13.444	12.053	11.005	10.471	10.323	10.067	10.496	10.324
2076488323940775680	5111949	12.767	13.395	12.024	11.009	10.464	10.346	10.233	10.341	10.392
2076488049062931328	5112288	12.788	13.423	12.038	11.026	10.460	10.337	10.229	10.324	10.491
2076487838597288320	5112373	12.766	13.402	12.016	10.990	10.393	10.312	10.195	10.275	10.396
2076487872957025408	5112387	12.786	13.424	12.036	11.005	10.448	10.341	10.237	10.323	10.387
2076581919866484224	5112401	12.572	13.208	11.824	10.804	10.230	10.081	10.001	10.116	10.200
2076393937742523904	5112730	12.729	13.365	11.979	10.939	10.400	10.250	10.164	10.254	10.220
2076393662864626176	5112950	12.715	13.367	11.954	10.922	10.355	10.207	10.083	10.187	10.040
2076582710140560000	5200152	12.678	13.289	11.952	10.974	10.425	10.306	10.193	10.317	10.528
<i>Ruprecht 147:</i>										
4084757199808535296	219239754	8.037	8.627	7.346	6.406	5.883	5.735	5.743	5.691	5.711
4183930438518525184	219624547	8.247	8.878	7.528	6.537	6.022	5.834	5.783	5.772	5.813
4087762027643173248	219310397	8.028	8.620	7.337	6.425	5.926	5.718	5.626	5.664	5.699
4184125807991900928	219614490	8.124	8.735	7.416	6.448	5.939	5.787	5.666	5.685	5.733
4184137077986034048	219704882	8.025	8.660	7.311	6.401	5.801	5.633	5.615	5.528	5.576

**Note.** Photometry from Gaia DR2, 2MASS, and WISE.

## Appendix F The Kepler $P_{\text{rot}}$ Data Set

McQuillan et al. (2014) published  $P_{\text{rot}}$  for 34,030 stars in the Kepler field using the ACF technique. M. Bedell cross-matched the Kepler Input Catalog (KIC) with Gaia DR2.<sup>47</sup> We downloaded the Kepler–Gaia cross-match table produced using a 1" search radius and then matched it with the McQuillan et al. (2014) catalog according to the KIC IDs. Next, we trimmed the sample in the following ways, which resulted in 16,259 nearby rotators cleaned of some categories of binaries and evolved stars:

1. Photometric binaries: We derived an empirical main sequence by fitting a cubic basis spline to the Hyades CMD, and for each Kepler rotator, we calculated the difference between its absolute magnitude (using the parallax for the distance correction) and the expected  $M_G$  based on its ( $G_{\text{BP}} - G_{\text{RP}}$ ) color and the Hyades CMD model. Stars with photometric excesses  $\Delta G > 0.5$  were trimmed.
2. Distant stars: Stars beyond 1 kpc were trimmed.
3. Astrometric binaries: Stars with excess astrometric noise indicative of binarity following the criteria we applied for the Ruprecht 147 sample were trimmed (i.e.,  $\epsilon_i > 0$  and  $D > 6$ ).
4. Spectroscopic binaries: Stars with Gaia DR2  $\sigma_{\text{RV}} > 3$  km s<sup>-1</sup> were trimmed.

Interstellar reddening can smear out intrinsically sharp structure in the color–period diagram, which is why we have restricted the sample to  $< 1000$  pc. To assess the impact of

reddening on this nearby subset, we used the catalog of spectroscopic parameters for the California-Kepler Survey stars observed with HIRES (CKS; Petigura et al. 2017) and analyzed with SME by Brewer & Fischer (2018). These stars tend to be much more distant than those in the CPS sample (Brewer et al. 2016a) that we used to construct our color–temperature relation (664 pc vs. 45 pc based on the median parallax of each sample). However, since the spectra were collected with the same instrument and setup and analyzed with the same procedure, we expect that our color–temperature relation can be used to accurately predict the intrinsic color for the more distant CKS stars, allowing us to estimate the amount of interstellar reddening toward each star.

We find negligible reddening for stars within 150 pc, shown in Figure 21. At 500 pc, the median value is  $E(B - V) = 0.017$  (10th and 90th percentiles are 0.00 and 0.06, respectively), corresponding to  $A_V = 0.054$  (0.00, 0.19). By 800 pc, the median reddening (extinction) has increased to 0.031 (0.096). At this distance, the reddening coherently varies across the Kepler field (right panel of the same figure), indicating that discrete cloud structures in the foreground are responsible for the larger scatter in the distance versus  $A_V$  diagram. This median reddening is approximately  $E(B - V) \approx 0.04$  mag kpc<sup>-1</sup>. The large variation across the field with this relatively small total value supports our decision to restrict the Kepler sample to  $< 1$  kpc, i.e., the differential reddening pattern is real, but the impact is not large, so intrinsically sharp features in the color–period distribution will not be smeared out much.

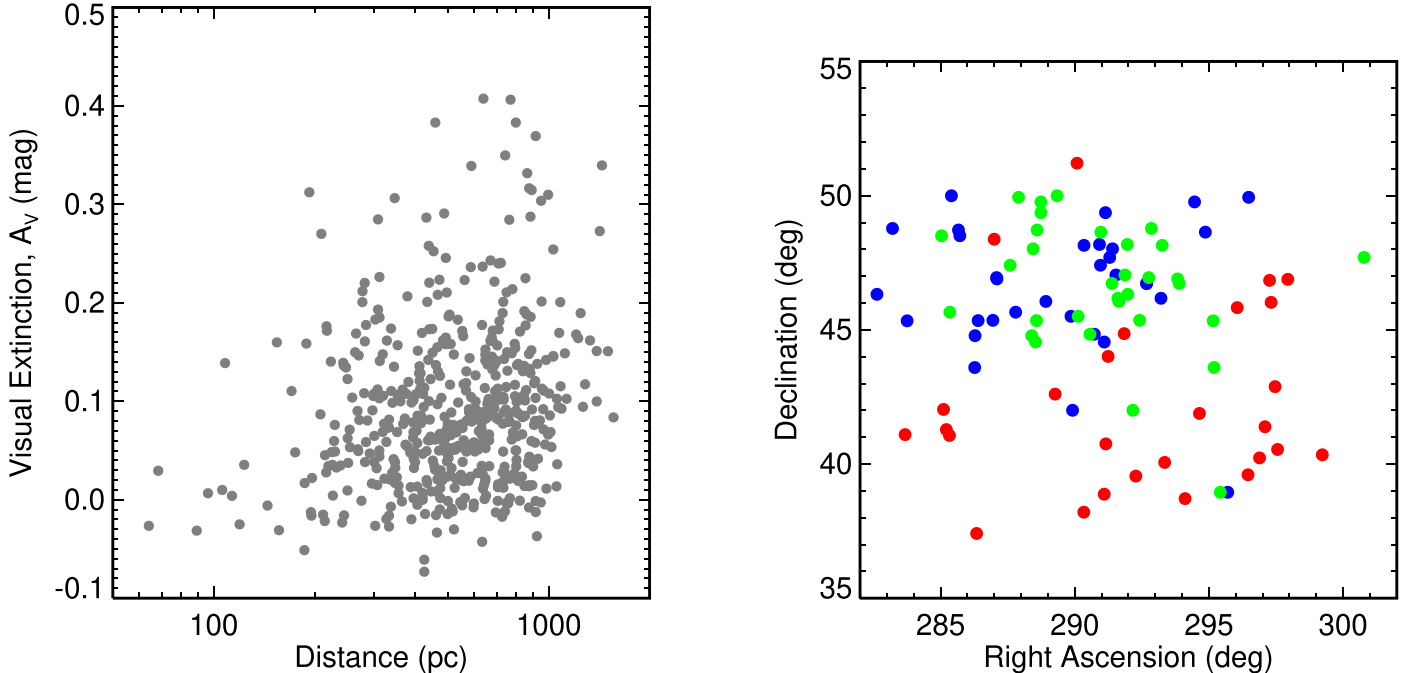


**Figure 21.** Interstellar reddening/extinction in the Kepler field. Left: using spectroscopic  $T_{\text{eff}}$  for CKS stars observed with HIRES (Brewer & Fischer 2018), we calculate the amount of reddening with our empirical color–temperature relation and then plot the results as a function of distance (using the inverted parallax). Within 150 pc, the reddening is negligible, and it increases with distance. Right: the equatorial coordinates for the subset of this sample at  $d = 800 \pm 100$  pc are plotted and color-coded according to the amount of reddening (blue:  $A_V < 0.05$ ; green:  $0.05 < A_V < 0.15$ ; red:  $A_V > 0.15$ ). The reddening varies coherently across the Kepler field, indicating the presence of foreground clouds. The scatter in  $A_V$  shown in the left panel appears to be primarily caused by differential reddening, not measurement uncertainties. The median trend is approximately  $E(B - V) = 0.04$  mag kpc<sup>-1</sup>, or  $A_V = 0.124$  mag kpc<sup>-1</sup>.

<sup>47</sup> <https://gaia-kepler.fun>

## Appendix G

### A Color- and Time-dependent Braking Index

Barnes (2003) proposed that stars spin down such that their  $P_{\text{rot}}$  could be described by a simple function that had separable dependencies on mass (using photometric color as a proxy) and time:  $P_{\text{rot}} = f(M_*, t) = g(M_*) \times h(t)$ . Following Skumanich (1972),  $h(t) = t^n$ , i.e., stars spin down with a common braking index that is constant in time. Although the cluster  $P_{\text{rot}}$  data demonstrate that stars do not spin down continuously, it is not yet clear whether stars share a common post-stalling braking index, or whether it is constant in time (i.e., Skumanich-like).

In Section 6.4, we applied such a Skumanich-like braking index with the value  $n = 0.62$  to calculate the “resume time,”  $t_R$ , when stars resume spinning down after exiting the stalling phase. This particular value of the braking index was tuned by Douglas et al. (2019) using solar-color Praesepe stars and the Sun. In this appendix, we will repeat this exercise using various pairings of benchmark populations, including Praesepe, NGC 6811, NGC 752, the joint NGC 6819 + Ruprecht 147 sample, and four old K dwarfs. We will use polynomial fits to the  $P_{\text{rot}}$  sequences for these various clusters, provided in Table 4.

#### G.1. NGC 752 K Dwarfs Compared to Ruprecht 147

For NGC 752, Agüeros et al. (2018) presented rotation periods for five mid-K dwarfs with Gaia DR2 astrometry consistent with membership.<sup>48</sup> They have  $T_{\text{eff}} = 4450 \pm 60$  K and  $M_* \approx 0.72\text{--}0.75 M_{\odot}$ , with  $P_{\text{rot}} = 14.0 \pm 1.4$  days. For Ruprecht 147, there are two rotators with these approximate colors, assuming  $A_V = 0.1$  for NGC 752: EPIC 219651610 (featured in Figures 3 and 4) and EPIC 219722781. These two stars have an average  $P_{\text{rot}} = 21.0$  days.<sup>49</sup>

The average braking index for these stars between 1.4 and 2.7 Gyr is therefore  $n = 0.62 \pm 0.1$ . This is consistent with the value found with Praesepe and the Sun, although the precision is limited by uncertainties in the  $P_{\text{rot}}$  for these K dwarfs and the uncertainties in the ages of each cluster.  $P_{\text{rot}}$  for additional members of NGC 752, and/or for an even older cluster, would be helpful for further testing this hypothesis and improving the precision of this calculation.

#### G.2. NGC 6819 + Ruprecht 147 Relative to NGC 6811

Comparing the eight solar analog rotators in NGC 6819 ( $T_{\text{eff}} = 5600\text{--}5800$  K) to the NGC 6811 sequence (1 Gyr), we find  $n = 0.59 \pm 0.02$ , which is close to the Praesepe–Sun value. However, extending this analysis to the full NGC 6819 and Ruprecht 147 sample, we find that stars with  $4600 \text{ K} < T_{\text{eff}} < 5600 \text{ K}$  (27 stars) have  $n = 0.73 \pm 0.04$ , which suggests that the post-stalling braking index does have some dependence on mass, or that the post-stalling braking index varies over this time interval.

Regarding the nine stars cooler than 4600 K, the braking index decreases away from the  $n = 0.73$  plateau toward cooler

<sup>48</sup> Listing Gaia DR2 IDs with  $P_{\text{rot}}$  in parentheses, these stars are 342523783591381504 (13.0 days), 342907478789972864 (14.0 days), 342854392994216064 (14.0 days), 342869957955643264 (16.6 days), and 342889611726120832 (13.9 days).

<sup>49</sup> We can also fit a linear relation for the rotators with  $1 < (G_{\text{BP}} - G_{\text{RP}})_0 < 1.8$  (15 stars) to estimate the 2.7 Gyr  $P_{\text{rot}}$  at the median color for the NGC 752 mid-K dwarfs, and we find  $P_{\text{rot}} = 20.9$  days, in agreement with the two stars most similar in color to the NGC 752 stars.

temperatures, reaching  $n \approx 0.2$  at 3700 K. Presumably, the time-averaged braking index between 1 and 2.7 Gyr for these cool dwarfs is still affected by stalling. As Curtis et al. (2019a) described, such a low braking index cannot be maintained throughout the age of the universe; otherwise, these late K and early M dwarfs would not be able to spin all the way down to the 40- to 50-day periods observed in the field.

#### G.3. Old Nearby K Dwarfs Relative to Ruprecht 147

Comparing the old and nearby K dwarfs ( $\alpha$  Cen B and 61 Cyg A and B) to the Ruprecht 147 slow sequence, we calculate  $n = 0.58, 0.63,$  and  $0.80$ , respectively (sorted from warmest to coolest). The warmest two are consistent with the values derived with the following pairs: Praesepe and the Sun, NGC 752 and Ruprecht 147, and the solar analogs of NGC 6819 and NGC 6811. Therefore, the gyrochronology ages inferred by projecting the Ruprecht 147 sequence forward in time with an  $n = 0.62$  braking law are consistent with the 6 Gyr ages we adopted at  $-5.4\%$  and  $1.5\%$ .

However, the value we find for 61 Cyg B is 30% larger than the mean for the other three K dwarfs, and its gyrochronology age is 26.3% larger than the Kervella et al. (2008) result. At its temperature (4044 K), the Ruprecht 147 sequence appears to dip down as it crosses the Kepler intermediate-period gap.

Establishing additional cool and old benchmarks for stellar rotation will be critical for deciphering the rotational evolution of such stars. For example, is this discrepancy due to inaccurate  $P_{\text{rot}}$  or age parameters for 61 Cyg B? A mean value of  $n = 0.62$  for the pair can be reached by increasing the age 61 Cyg by 0.8 Gyr (within the 1 Gyr uncertainty). Or is the braking history more complex than we have assumed?

#### G.4. The Slow Period Edge in the Kepler Distribution Relative to Ruprecht 147

The  $P_{\text{rot}}$  distribution for Kepler field stars has a well-defined upper envelope. van Saders et al. (2019) divided this feature into warm and cool portions, separated at  $T_{\text{eff}} \approx 5000$  K. The warm side is steeply sloped and is probably shaped by a detection threshold and/or a final shutdown of magnetic braking (van Saders et al. 2016).

Stars cooler than 5000 K are not old enough to be affected by these proposals, so the upper edge might represent the oldest stars in the Kepler sample. If we assume that those stars are 10 Gyr old (or 13.7 Gyr old), then it would take a time-averaged braking index of  $n = 0.55$  (or 0.45) to project the Ruprecht 147 sequence forward in time to match this edge, similar to the classic Skumanich law.

#### G.5. Summary of Calculations for the Post-stalling Braking Index

All values calculated from these various samples range between  $n \approx 0.5$  and 0.8, summarized below:



















*Solar analogs.*—All samples indicate  $n \approx 0.6$ , including Praesepe and the Sun, NGC 6811 and the Sun, and NGC 6811 and NGC 6819.

*Early K dwarfs.*—The NGC 6819 + R147 joint sample compared to NGC 6811 yielded  $n = 0.73$ ; however, we found  $n \approx 0.6$  from the comparison between the old K dwarfs in the field with the R147 sequence. This suggests that stars of a given mass might not spin down with a single-valued post-stalling braking index that is constant in time.

*Mid-K dwarfs.*—The R147 stars compared to the NGC 6811 sequence, the NGC 752 stars compared to the R147 sequence, and 61 Cyg A compared to the R147 sequence all returned  $n \approx 0.6$ .

*Late K to early M dwarfs.*—The comparison between R147 stars and the NGC 6811 sequence is likely biased by stalling ( $n \approx 0.3$ – $0.4$ ). Comparing 61 Cyg B with the R147 sequence returned one of the highest values of  $n \approx 0.8$ . Finally, projecting the R147 sequence forward in time with  $n = 0.5$  reaches the upper edge of the Kepler field in  $\approx 11$  Gyr.

### ORCID iDs

Jason Lee Curtis  <https://orcid.org/0000-0002-2792-134X>  
 Marcel A. Agüeros  <https://orcid.org/0000-0001-7077-3664>  
 Sean P. Matt  <https://orcid.org/0000-0001-9590-2274>  
 Kevin R. Covey  <https://orcid.org/0000-0001-6914-7797>  
 Stephanie T. Douglas  <https://orcid.org/0000-0001-7371-2832>  
 Ruth Angus  <https://orcid.org/0000-0003-4540-5661>  
 Steven H. Saar  <https://orcid.org/0000-0001-7032-8480>  
 Ann Marie Cody  <https://orcid.org/0000-0002-3656-6706>  
 Andrew Vanderburg  <https://orcid.org/0000-0001-7246-5438>  
 Nicholas M. Law  <https://orcid.org/0000-0001-9380-6457>  
 Adam L. Kraus  <https://orcid.org/0000-0001-9811-568X>  
 David W. Latham  <https://orcid.org/0000-0001-9911-7388>  
 Christoph Baranec  <https://orcid.org/0000-0002-1917-9157>  
 Reed Riddle  <https://orcid.org/0000-0002-0387-370X>  
 Carl Ziegler  <https://orcid.org/0000-0002-0619-7639>  
 Mikkel N. Lund  <https://orcid.org/0000-0001-9214-5642>  
 Guillermo Torres  <https://orcid.org/0000-0002-5286-0251>  
 Victor Silva Aguirre  <https://orcid.org/0000-0002-6137-903X>  
 Jason T. Wright  <https://orcid.org/0000-0001-6160-5888>

### References

- Agüeros, M. A., Bowsher, E. C., Bochanski, J. J., et al. 2018, *ApJ*, **862**, 33  
 Agüeros, M. A., Covey, K. R., Lemonias, J. J., et al. 2011, *ApJ*, **740**, 110  
 Ahumada, R., Allende Prieto, C., Almeida, A., et al. 2020, *ApJS*, **249**, 3  
 Aigrain, S., Parviainen, H., & Pope, B. J. S. 2016, *MNRAS*, **459**, 2408  
 Amard, L., & Matt, S. P. 2020, *ApJ*, **889**, 108  
 Andrae, R., Fousneau, M., Creevey, O., et al. 2018, *A&A*, **616**, A8  
 Angus, R., Aigrain, S., Foreman-Mackey, D., & McQuillan, A. 2015, *MNRAS*, **450**, 1787  
 Angus, R., Beane, A., Price-Whelan, A. M., et al. 2020, *AJ*, **160**, 90  
 Angus, R., Morton, T. D., Foreman-Mackey, D., et al. 2019, *AJ*, **158**, 173  
 Anthony-Twarog, B. J., Deliyannis, C. P., & Twarog, B. A. 2014, *AJ*, **148**, 51  
 Anthony-Twarog, B. J., Lee-Brown, D. B., Deliyannis, C. P., & Twarog, B. A. 2018, *AJ*, **155**, 138  
 Bailer-Jones, C. A. L., Andrae, R., Arcay, B., et al. 2013, *A&A*, **559**, A74  
 Bailer-Jones, C. A. L., Rybizki, J., Fousneau, M., Mantelet, G., & Andrae, R. 2018, *AJ*, **156**, 58  
 Baliunas, S. L., Hartmann, L., Noyes, R. W., et al. 1983, *ApJ*, **275**, 752  
 Baranec, C., Riddle, R., Law, N. M., et al. 2014, *ApJL*, **790**, L8  
 Barnes, S. A. 2003, *ApJ*, **586**, 464  
 Barnes, S. A. 2007, *ApJ*, **669**, 1167  
 Barnes, S. A. 2010, *ApJ*, **722**, 222  
 Barnes, S. A., Weingrill, J., Granzer, T., Spada, F., & Strassmeier, K. G. 2015, *A&A*, **583**, A73  
 Basri, G., & Nguyen, H. T. 2018, *ApJ*, **863**, 190  
 Basri, G., Walkowicz, L. M., Batalha, N., et al. 2010, *ApJL*, **713**, L155  
 Bazot, M., Bourguignon, S., & Christensen-Dalsgaard, J. 2012, *MNRAS*, **427**, 1847  
 Beatty, T. G., Morley, C. V., Curtis, J. L., et al. 2018, *AJ*, **156**, 168  
 Bernstein, R., Shectman, S. A., Gunnels, S. M., Mochnacki, S., & Athey, A. E. 2003, *Proc. SPIE*, **4841**, 1694  
 Boro Saikia, S., Jeffers, S. V., Morin, J., et al. 2016, *A&A*, **594**, A29  
 Boyajian, T. S., von Braun, K., van Belle, G., et al. 2012, *ApJ*, **757**, 112  
 Bragaglia, A., Carretta, E., Gratton, R. G., et al. 2001, *AJ*, **121**, 327  
 Bragaglia, A., Fu, X., Mucciarelli, A., Andreuzzi, G., & Donati, P. 2018, *A&A*, **619**, A176  
 Bressan, A., Marigo, P., Girardi, L., et al. 2012, *MNRAS*, **427**, 127  
 Brewer, J. M., & Fischer, D. A. 2018, *ApJS*, **237**, 38  
 Brewer, J. M., Fischer, D. A., Basu, S., Valenti, J. A., & Piskunov, N. 2015, *ApJ*, **805**, 126  
 Brewer, J. M., Fischer, D. A., Valenti, J. A., & Piskunov, N. 2016a, *ApJS*, **225**, 32  
 Brewer, L. N., Sandquist, E. L., Mathieu, R. D., et al. 2016b, *AJ*, **151**, 66  
 Cantat-Gaudin, T., Jordi, C., Vallenari, A., et al. 2018, *A&A*, **618**, A93  
 Cargile, P. A., James, D. J., Pepper, J., et al. 2014, *ApJ*, **782**, 29  
 Casamiquela, L., Tarricq, Y., Soubiran, C., et al. 2020, *A&A*, **635**, A8  
 Churchwell, E., Babler, B. L., Meade, M. R., et al. 2009, *PASP*, **121**, 213  
 Cody, A. M., Barentsen, G., Hedges, C., Gully-Santiago, M., & Cardoso, J. V. D. M. 2018, *RNAAS*, **2**, 25  
 Costa, A. D., Canto Martins, B. L., Bravo, J. P., et al. 2015, *ApJL*, **807**, L21  
 Covey, K. R., Agüeros, M. A., Law, N. M., et al. 2016, *ApJ*, **822**, 81  
 Cranmer, S. R., & Saar, S. H. 2011, *ApJ*, **741**, 54  
 Cummings, J. D., & Kalirai, J. S. 2018, *AJ*, **156**, 165  
 Cummings, J. D., Kalirai, J. S., Tremblay, P. E., Ramirez-Ruiz, E., & Choi, J. 2018, *ApJ*, **866**, 21  
 Curtis, J., Vanderburg, A., Montet, B., et al. 2016, A Warm Brown Dwarf Transiting a Solar Analog in a Benchmark Cluster, v1, Zenodo, doi:10.5281/zenodo.58758  
 Curtis, J. L. 2016, PhD thesis, Penn State Univ. [https://etda.libraries.psu.edu/files/final\\_submissions/13071](https://etda.libraries.psu.edu/files/final_submissions/13071)  
 Curtis, J. L. 2017, *AJ*, **153**, 275  
 Curtis, J. L., Agüeros, M. A., Douglas, S. T., & Meibom, S. 2019a, *ApJ*, **879**, 49  
 Curtis, J. L., Agüeros, M. A., Mamajek, E. E., Wright, J. T., & Cummings, J. D. 2019b, *AJ*, **158**, 77  
 Curtis, J. L., Vanderburg, A., Torres, G., et al. 2018, *AJ*, **155**, 173  
 Curtis, J. L., Wolfgang, A., Wright, J. T., Brewer, J. M., & Johnson, J. A. 2013, *AJ*, **145**, 134  
 Dahm, S. E. 2015, *ApJ*, **813**, 108  
 Davenport, J. R. A. 2017, *ApJ*, **835**, 16  
 Davenport, J. R. A., & Covey, K. R. 2018, *ApJ*, **868**, 151  
 Deliyannis, C. P., Anthony-Twarog, B. J., Lee-Brown, D. B., & Twarog, B. A. 2019, *AJ*, **158**, 163  
 DeWarf, L. E., Datin, K. M., & Guinan, E. F. 2010, *ApJ*, **722**, 343  
 Donahue, R. A., Saar, S. H., & Baliunas, S. L. 1996, *ApJ*, **466**, 384  
 Donor, J., Frinchaboy, P. M., Cunha, K., et al. 2018, *AJ*, **156**, 142  
 Donor, J., Frinchaboy, P. M., Cunha, K., et al. 2020, *AJ*, **159**, 199  
 Douglas, S. T., Agüeros, M. A., Covey, K. R., et al. 2016, *ApJ*, **822**, 47  
 Douglas, S. T., Agüeros, M. A., Covey, K. R., & Kraus, A. 2017, *ApJ*, **842**, 83  
 Douglas, S. T., Curtis, J. L., Agüeros, M. A., et al. 2019, *ApJ*, **879**, 100  
 Duchêne, G., & Kraus, A. 2013, *ARA&A*, **51**, 269  
 Dumusque, X., Pepe, F., Lovis, C., et al. 2012, *Natur*, **491**, 207  
 Eggenberger, P., Charbonnel, C., Talon, S., et al. 2004, *A&A*, **417**, 235  
 Engle, S. G., & Guinan, E. F. 2018, *RNAAS*, **2**, 34  
 Evans, D. W., Riello, M., De Angeli, F., et al. 2018, *A&A*, **616**, A4  
 Fabricant, D., Fata, R. G., McLeod, B. A., et al. 2004, *Proc. SPIE*, **5492**, 767  
 Friel, E. D., Janes, K. A., Tavaréz, M., et al. 2002, *AJ*, **124**, 2693  
 Fűrész, G., Szentgyörgyi, A. H., & Meibom, S. 2008, in Precision Spectroscopy in Astrophysics, ed. N. C. Santos et al. (Berlin: Springer), **287**  
 Gaia Collaboration, Babusiaux, C., van Leeuwen, F., et al. 2018a, *A&A*, **616**, A10  
 Gaia Collaboration, Brown, A. G. A., Vallenari, A., et al. 2018b, *A&A*, **616**, A1  
 Gallet, F., & Bouvier, J. 2013, *A&A*, **556**, A36  
 Gallet, F., & Bouvier, J. 2015, *A&A*, **577**, A98  
 Geller, A. M., Mathieu, R. D., Harris, H. C., & McClure, R. D. 2008, *AJ*, **135**, 2264  
 Giampapa, M. S., Hall, J. C., Radick, R. R., & Baliunas, S. L. 2006, *ApJ*, **651**, 444  
 Gossage, S., Conroy, C., Dotter, A., et al. 2018, *ApJ*, **863**, 67  
 Gruner, D., & Barnes, S. A. 2020, *A&A*, in press (arXiv:2010.02298)  
 Guinan, E. F., & Engle, S. G. 2009, arXiv:0901.1860  
 Guinan, E. F., & Engle, S. G. 2019, *RNAAS*, **3**, 189  
 Hartman, J. D., Gaudi, B. S., Pinsonneault, M. H., et al. 2009, *ApJ*, **691**, 342  
 Hawkins, K., Leistedt, B., Bovy, J., & Hogg, D. W. 2017, *MNRAS*, **471**, 722  
 Heiter, U., Jofré, P., Gustafsson, B., et al. 2015, *A&A*, **582**, A49  
 Hole, K. T., Geller, A. M., Mathieu, R. D., et al. 2009, *AJ*, **138**, 159  
 Howell, S. B., Sobek, C., Haas, M., et al. 2014, *PASP*, **126**, 398  
 Huber, D., Bryson, S. T., Haas, M. R., et al. 2016, *ApJS*, **224**, 2

- Janes, K. 2018, in 20th Cambridge Workshop on Cool Stars, Stellar Systems and the Sun, Cambridge Workshop on Cool Stars, Stellar Systems, and the Sun (Cambridge, MA: Harvard Univ. Press), 85
- Janes, K. A. 2017, *ApJ*, **835**, 75
- Kervella, P., Mérand, A., Pichon, B., et al. 2008, *A&A*, **488**, 667
- Kounkel, M., & Covey, K. 2019, *AJ*, **158**, 122
- Kraus, A. L., Douglas, S. T., Mann, A. W., et al. 2017, *ApJ*, **845**, 72
- Kraus, A. L., & Hillenbrand, L. A. 2007, *AJ*, **134**, 2340
- Lamm, M. H., Bailer-Jones, C. A. L., Mundt, R., Herbst, W., & Scholz, A. 2004, *A&A*, **417**, 557
- Landsman, W. B. 1993, in ASP Conf. Ser. 52, *Astronomical Data Analysis Software and Systems II*, ed. R. J. Hanisch, R. J. V. Brissenden, & J. Barnes (San Francisco, CA: ASP), 246
- Lanzafame, A. C., & Spada, F. 2015, *A&A*, **584**, A30
- Law, N. M., Dekany, R. G., Rahmer, G., et al. 2010, *Proc. SPIE*, **7735**, 77353M
- Law, N. M., Kulkarni, S. R., Dekany, R. G., et al. 2009, *PASP*, **121**, 1395
- Lee-Brown, D. B., Anthony-Twarog, B. J., Deliyannis, C. P., Rich, E., & Twarog, B. A. 2015, *AJ*, **149**, 121
- Leiner, E., Mathieu, R. D., Vanderburg, A., Gosnell, N. M., & Smith, J. C. 2019, *ApJ*, **881**, 47
- Lindgren, L., Hernández, J., Bombrun, A., et al. 2018, *A&A*, **616**, A2
- Liu, F., Asplund, M., Yong, D., et al. 2016, *MNRAS*, **463**, 696
- Lorenzo-Oliveira, D., Freitas, F. C., Meléndez, J., et al. 2018, *A&A*, **619**, A73
- Luger, R., Agol, E., Kruse, E., et al. 2016, *AJ*, **152**, 100
- Luger, R., Kruse, E., Foreman-Mackey, D., Agol, E., & Saunders, N. 2018, *AJ*, **156**, 99
- MacGregor, K. B., & Brenner, M. 1991, *ApJ*, **376**, 204
- Mamajek, E. 2014, The Sun Rotates Normally for its Age, doi:10.6084/m9.figshare.1051826, [https://figshare.com/articles/figure/The\\_Sun\\_Rotates\\_Normally\\_for\\_its\\_Age/1051826](https://figshare.com/articles/figure/The_Sun_Rotates_Normally_for_its_Age/1051826)
- Mamajek, E. E., & Hillenbrand, L. A. 2008, *ApJ*, **687**, 1264
- Mann, A. W., Feiden, G. A., Gaidos, E., Boyajian, T., & von Braun, K. 2015, *ApJ*, **804**, 64
- Marshall, J. L., Burke, C. J., DePoy, D. L., Gould, A., & Kollmeier, J. A. 2005, *AJ*, **130**, 1916
- Marshall, J. L., Burles, S., Thompson, I. B., et al. 2008, *Proc. SPIE*, **7014**, 701454
- Matt, S. P., Brun, A. S., Baraffe, I., Bouvier, J., & Chabrier, G. 2015, *ApJL*, **799**, L23
- Mayor, M., Pepe, F., Queloz, D., et al. 2003, *Msngr*, **114**, 20
- McQuillan, A., Aigrain, S., & Mazeh, T. 2013, *MNRAS*, **432**, 1203
- McQuillan, A., Mazeh, T., & Aigrain, S. 2014, *ApJS*, **211**, 24
- Meibom, S., Barnes, S. A., Latham, D. W., et al. 2011a, *ApJL*, **733**, L9
- Meibom, S., Barnes, S. A., Platais, I., et al. 2015, *Natur*, **517**, 589
- Meibom, S., Grundahl, F., Clausen, J. V., et al. 2009a, *AJ*, **137**, 5086
- Meibom, S., & Mathieu, R. D. 2005, *ApJ*, **620**, 970
- Meibom, S., Mathieu, R. D., & Stassun, K. G. 2009b, *ApJ*, **695**, 679
- Meibom, S., Mathieu, R. D., Stassun, K. G., Liebesny, P., & Saar, S. H. 2011b, *ApJ*, **733**, 115
- Miglio, A., & Montalbán, J. 2005, *A&A*, **441**, 615
- Milliman, K. E., Mathieu, R. D., Geller, A. M., et al. 2014, *AJ*, **148**, 38
- Milliman, K. E., Mathieu, R. D., & Schuler, S. C. 2015, *AJ*, **150**, 84
- Mullally, F., Barclay, T., & Barentsen, G. 2016, K2fov: Field of view software for NASA's K2 mission, Astrophysics Source Code Library, ascl:1601.009
- Ness, M., Hogg, D. W., Rix, H.-W., et al. 2016, *ApJ*, **823**, 114
- Nowak, G., Palle, E., Gandolfi, D., et al. 2017, *AJ*, **153**, 131
- Noyes, R. W., Hartmann, L. W., Baliunas, S. L., Duncan, D. K., & Vaughan, A. H. 1984, *ApJ*, **279**, 763
- Ochsenbein, F., Bauer, P., & Marcout, J. 2000, *A&AS*, **143**, 23
- Olivares, J., Bouy, H., Sarro, L. M., et al. 2019, *A&A*, **625**, A115
- Önehag, A., Korn, A., Gustafsson, B., Stempels, E., & Vandenberg, D. A. 2011, *A&A*, **528**, A85
- Paczynski, B., & Stanek, K. Z. 1998, *ApJL*, **494**, L219
- Pakhomov, Y. V., Antipova, L. I., Boyarchuk, A. A., et al. 2009, *ARep*, **53**, 660
- Peri, M. L. 1995, PhD thesis, AA(California Inst. of Tech.)
- Petigura, E. A., Howard, A. W., Marcy, G. W., et al. 2017, *AJ*, **154**, 107
- Pinsonneault, M. H., Elsworth, Y., Epstein, C., et al. 2014, *ApJS*, **215**, 19
- Platais, I., Gosnell, N. M., Meibom, S., et al. 2013, *AJ*, **146**, 43
- Press, W. H., & Rybicki, G. B. 1989, *ApJ*, **338**, 277
- Rabus, M., Lachaume, R., Jordán, A., et al. 2019, *MNRAS*, **484**, 2674
- Raghavan, D., McAlister, H. A., Henry, T. J., et al. 2010, *ApJS*, **190**, 1
- Rahmer, G., Smith, R., Velur, V., et al. 2008, *Proc. SPIE*, **7014**, 70144Y
- Rau, A., Kulkarni, S. R., Law, N. M., et al. 2009, *PASP*, **121**, 1334
- Rebull, L. M., Stauffer, J. R., Bouvier, J., et al. 2016, *AJ*, **152**, 113
- Rebull, L. M., Stauffer, J. R., Cody, A. M., et al. 2018, *AJ*, **155**, 196
- Rebull, L. M., Stauffer, J. R., Hillenbrand, L. A., et al. 2017, *ApJ*, **839**, 92
- Reinhold, T., Bell, K. J., Kuzlewicz, J., Hekker, S., & Shapiro, A. I. 2019, *A&A*, **621**, A21
- Reinhold, T., & Hekker, S. 2020, *A&A*, **635**, 43
- Ricker, G. R., Winn, J. N., Vanderspek, R., et al. 2015, *JATIS*, **1**, 014003
- Roeser, S., Demleitner, M., & Schillbach, E. 2010, *AJ*, **139**, 2440
- Sahlholdt, C. L., & Silva Aguirre, V. 2018, *MNRAS*, **481**, L125
- Scargle, J. D. 1982, *ApJ*, **263**, 835
- Skrutskie, M. F., Cutri, R. M., Stiening, R., et al. 2006, *AJ*, **131**, 1163
- Skumanich, A. 1972, *ApJ*, **171**, 565
- Slumstrup, D., Grundahl, F., Brogaard, K., et al. 2017, *A&A*, **604**, L8
- Smith, J. C., Stumpe, M. C., Van Cleve, J. E., et al. 2012, *PASP*, **124**, 1000
- Soubiran, C., Jasniewicz, G., Chemin, L., et al. 2013, *A&A*, **552**, A64
- Soydugan, E., Alicavus, F., Soydugan, F., et al. 2020, arXiv:2009.05610
- Spada, F., & Demarque, P. 2019, *MNRAS*, **489**, 4712
- Spada, F., & Lanzafame, A. C. 2020, *A&A*, **636**, A76
- Stassun, K. G., & Torres, G. 2018, *ApJ*, **862**, 61
- Stauffer, J., Rebull, L., Bouvier, J., et al. 2016, *AJ*, **152**, 115
- Stauffer, J. R., Schultz, G., & Kirkpatrick, J. D. 1998, *ApJL*, **499**, L199
- Stello, D., Meibom, S., Gilliland, R. L., et al. 2011, *ApJ*, **739**, 13
- Stumpe, M. C., Smith, J. C., Van Cleve, J. E., et al. 2012, *PASP*, **124**, 985
- Szentgyorgyi, A. H., Cheimets, P., Eng, R., et al. 1998, *Proc. SPIE*, **3355**, 242
- Szentgyorgyi, A. H., & Fűrész, G. 2007, *Revista Mexicana de Astronomia y Astrofisica Conference Series*, **28**, 129
- Thévenin, F., Provost, J., Morel, P., et al. 2002, *A&A*, **392**, L9
- Thoul, A., Scuflaire, R., Noels, A., et al. 2003, *A&A*, **402**, 293
- Torres, G., Curtis, J. L., Vanderburg, A., Kraus, A. L., & Rizzuto, A. 2018, *ApJ*, **866**, 67
- Torres, G., Vanderburg, A., Curtis, J. L., et al. 2019, *ApJ*, **887**, 109
- Torres, G., Vanderburg, A., Curtis, J. L., et al. 2020, *ApJ*, **896**, 162
- Trifonov, T., Tal-Or, L., Zechmeister, M., et al. 2020, *A&A*, **636**, 74
- Twarog, B. A., Anthony-Twarog, B. J., Deliyannis, C. P., & Thomas, D. T. 2015, *AJ*, **150**, 134
- Valenti, J. A., & Fischer, D. A. 2005, *ApJS*, **159**, 141
- Valenti, J. A., & Piskunov, N. 1996, *A&AS*, **118**, 595
- van Saders, J. L., Ceillier, T., Metcalfe, T. S., et al. 2016, *Natur*, **529**, 181
- van Saders, J. L., & Pinsonneault, M. H. 2013, *ApJ*, **776**, 67
- van Saders, J. L., Pinsonneault, M. H., & Barbieri, M. 2019, *ApJ*, **872**, 128
- Vanderburg, A., & Johnson, J. A. 2014, *PASP*, **126**, 948
- Vogt, S. S. 1987, *PASP*, **99**, 1214
- Vogt, S. S., Allen, S. L., Bigelow, B. C., et al. 1994, *Proc. SPIE*, **2198**, 362
- Wenger, M., Ochsenbein, F., Egret, D., et al. 2000, *A&AS*, **143**, 9
- Wright, E. L., Eisenhardt, P. R. M., Mainzer, A. K., et al. 2010, *AJ*, **140**, 1868
- Wright, J. T., Marcy, G. W., Butler, R. P., & Vogt, S. S. 2004, *ApJS*, **152**, 261
- Xiang, M. S., Liu, X. W., Yuan, H. B., et al. 2015, *MNRAS*, **448**, 822
- Yang, S.-C., Sarajedini, A., Deliyannis, C. P., et al. 2013, *ApJ*, **762**, 3
- Yeh, F. C., Carraro, G., Montalto, M., & Seleznev, A. F. 2019, *AJ*, **157**, 115
- Yildız, M. 2007, *MNRAS*, **374**, 1264
- Zacharias, N., Monet, D. G., Levine, S. E., et al. 2004a, *BAAS*, **36**, 1418
- Zacharias, N., Urban, S. E., Zacharias, M. I., et al. 2004b, *AJ*, **127**, 3043
- Ziegler, C., Law, N. M., Baranec, C., et al. 2018, *AJ*, **156**, 83
- Zinn, J. C., Pinsonneault, M. H., Huber, D., & Stello, D. 2019, *ApJ*, **878**, 136